The Influence of Snow Cover Variability and Tundra Lakes on Passive Microwave Remote Sensing of Late Winter Snow Water Equivalent in the Hudson Bay Lowlands

by

Peter Toose

A thesis
presented to the University of Waterloo
in fulfillment of the
thesis requirement for the degree of
Master of Environmental Studies
in
Geography

Waterloo, Ontario, Canada, 2007

AUTHOR'S DECLARATION

I hereby declare that I am the sole author of this thesis. This is a true copy of the thesis, including any required final revisions, as accepted by my examiners. I understand that my thesis may be made electronically available to the public.

Abstract

Four years of regional snow surveys in the Northwest Territories and northern Manitoba, Canada, have shown that current North American operational passive microwave snow water equivalent (SWE) retrieval algorithms consistently underestimate in tundra environments. Almost all contemporary SWE algorithms are based on the brightness temperature difference between the 37GHz and 19GHz frequencies found onboard both past and present spaceborne sensors. The passive microwave underestimation of SWE is likely a result of the distribution and deposition of the tundra snow, coupled with the influence of tundra lakes on brightness temperatures at 19GHz. The tundra environment is dominated by thousands of small lakes and ponds which can cover up to 30-40% of the landscape and current SWE algorithms do not consider the impact of sub-grid scale lake-cover fraction. To better our understanding concerning the underestimation of passive microwave SWE retrievals on the tundra, Environment Canada conducted an intensive field campaign in March 2006, just south of Churchill, Manitoba. In situ measurements of snow depth, SWE, snow density, snow grain size and snow stratigraphy were recorded at 87 sites within a 25km by 25km grid located over the Marantz Lake region of the Hudson Bay Coastal Plains. Coincident multi-scale passive microwave airborne (70m resolution) and spaceborne (regridded to 25km resolution) data were measured at 6.9GHz, 19GHz, 37GHz and ~89 GHz frequencies during the same time period.

An analysis of the snow survey data highlighted small-scale localized patterns of snow distribution and deposition on the tundra that likely influenced the SWE underestimation from large-scale passive microwave spaceborne sensors. The distribution of snow in this environment was controlled largely by wind and the presence of taller vegetation (approximately greater than 1m in height). Snow from the open tundra plains was re-distributed into smaller scale features with taller vegetation such as narrow creekbeds, lake edge willows and small tundra tree-islands. The very large amount of snow deposited in these features has a reduced influence on the microwave emission measured by large-scale passive microwave spaceborne sensors because of the small proportion of the land cover these features encompass, and is therefore most likely unaccounted for in current methods of satellite SWE estimation.

Analysis of the high-resolution airborne data revealed a sensitivity of the 19GHz frequency to tundra lake features. The magnitude of 19GHz emission measured over some lakes was far less than the surrounding land surfaces, effectively minimizing the difference between the 37GHz and 19GHz

brightness temperatures, thereby resulting in lower SWE retrievals. Interestingly, the 19GHz frequency was not sensitive to all lakes. A unique characteristic of tundra lakes and ponds are their shallow nature; lakes and ponds can completely freeze to their beds, and when this occurs, it was hypothesized that the 19GHz frequency would no longer be as sensitive to the lakes. To provide a possible explanation for why the 19GHz brightness temperatures were influenced in different ways by different tundra lakes, the production of a regional tundra lake ice map using a time series of RADARSAT-1 ScanSAR Wide-A imagery was conducted.

The production of the regional tundra lake ice map was based on the established technique of using a synthetic aperture radar winter time series for identifying a probable set of lakes that were most likely frozen to bottom or had free-floating ice based on the observed change in backscatter intensity values throughout the winter season. There was no way of confirming whether the different lake ice types identified were accurate because no field observations of lake ice information were collected during the March 2006 field campaign. Instead, a comparison of the pattern and magnitude of the changing backscatter values for each different ice type was conducted with previous SAR lake ice studies. There were some differences in magnitude and ranges of backscatter values, but the shape of the backscatter intensity patterns compared nicely with previous studies for the floating and grounded lake ice types indicating that these types of lake ice can likely be identified with some confidence.

The results of this study highlight the difficulty in using coarse resolution passive microwave spaceborne sensors to estimate SWE in an environment with heterogeneous sub-grid lake cover and snow distribution. There is great potential in using a time series of RADARSAT ScanSAR Wide images for the purpose of mapping regional lake ice conditions to assist in the interpretation of tundra passive microwave brightness temperatures. An accurate regional lake ice map and information on snow cover distribution based on land cover information would be very useful as inputs into future tundra specific SWE algorithms so that appropriate correction coefficients could be applied.

Acknowledgements

The successful completion of this thesis is due to all the help and support I have received from many different people over the last two years, both in the collection and processing of all the data used in this study and in the writing and editing of the finished product.

For the data collection and processing I would like to first express my sincerest appreciation for the tireless efforts of the Environment Canada tundra snow surveyors, Dr. Chris Derksen and 'SWE man' Arvids Silis, and from Wilfrid Laurier University, Andrew Rees, for all their hard work and patience in the collection of such a great dataset! I would also like to thank all the National Research Council and Environment Canada personnel involved with the passive microwave airborne data collection and again Arvids Silis for the many hours spent running the non-linear, multi-iterative airborne brightness temperature calibration procedure. I would also like to thank the staff from the Churchill Northern Study Centre for making our stay comfortable and a very special thanks to the study centre Cook who fueled our tundra snow surveys with his delicious tundra stroodles! Another special thanks is given to our pilot Kenny Dunthorne from Custom Helicopters of Manitoba for all his skills in keeping us aloft in all types of weather and for safely clearing the short tundra trees during take-off! I would also like to thank Ryan Brook from the University of Manitoba for sharing his classified land cover map of the Cape Churchill Wildlife Management Area that overlapped our tundra study site, and Environment Canada's Canadian Ice Services for access to the RADARSAT ScanSAR Wide winter time series. Thanks are also extended to Matt Arkett and John 'Alex' Casey from the Ice Services and Dr. Claude Duguay from the University of Waterloo for their help and guidance in the loading and processing the RADARSAT data into PCI Geomatica.

For the writing and editing stage of this thesis I cannot begin to express my thanks for all the feedback, editing, and suggestions I received from Environment Canada's Dr. Chris Derksen and from the University of Waterloo my advisor Dr. Ellsworth LeDrew and Dr. Richard Kelly.

And lastly, I would like to thank Buffy de Ruiter for all her love, support and patience while I wrote this thesis over the last two years and for at least appearing to be interested in my 'exciting' and 'interesting' results!

Table of Contents

Chapter 1 Introduction 1
1.1 Overview 1
1.2 Remote sensing of SWE 1
1.3 Research objectives 3
1.4 Research significance 4
1.5 Thesis outline 5
Chapter 2 Research Context 6
2.1 Overview of spaceborne passive microwave remote sensors 6
2.2 Fundamental concepts of passive microwave remote sensing of SWE 8
2.2.1 Remote sensing: electromagnetic energy 8
2.2.2 Factors that influence microwave emission 10
2.2.3 Microwave emission from snow 11
2.2.4 Passive microwave SWE retrieval algorithms 12
2.3 Arctic and tundra snowpack properties relevant to passive microwave SWE estimation 13
2.3.1 Arctic and tundra snow distribution 13
2.3.2 Arctic and tundra snow structure and grain size 14
2.4 Passive microwave remote sensing in the arctic and subarctic 15
2.4.1 Passive microwave remote sensing of subarctic depth hoar dominated snowpacks 16
2.4.2 Issues of scale with passive microwave remote sensing of tundra snow distribution 17
2.4.3 Influence of freshwater lakes on passive microwave SWE estimation 18
2.5 Arctic and subarctic lake ice information from synthetic aperture radar 19
2.6 Summary 23
Chapter 3 Tundra Study Site Description and Physical Setting 24
3.1 Hudson Bay Coastal Plains 24
3.2 Tundra study site 24
3.2.1 Climate and weather 26
3.2.2 Land cover information 26
3.2.3 Topographic relief 28
3.3 Summary 29

Chapter 4 Data Collection and Processing Methods 30
4.1 Passive microwave brightness temperature data sources 31
4.1.1 Spaceborne brightness temperatures 31
4.1.2 Airborne brightness temperatures 32
4.2 Snow survey sampling methods 34
4.2.1 Grid Intersection sampling 34
4.2.2 Run & Gun sampling 37
4.2.3 Snow survey classification 37
4.3 Creating a high resolution lake mask 40
4.4 Create a regional tundra lake ice map from a SAR time series 41
4.4.1 Choosing appropriate RADARSAT images for the winter time series 41
4.4.2 Processing of the raw CEOS RADARSAT images to create a winter time series 42
4.4.3 Defining RADARSAT backscatter intensity plots to identify different lake ice types 44
4.4.4 Conducting a principal component analysis on the SAR winter time series 46
4.4.5 Conducting a supervised classification to create a regional tundra lake ice map 47
4.5 Summary 48
Chapter 5 Snow Survey and Brightness Temperature Analysis Results 49
5.1 Summary of tundra study site snow properties 49
5.2 Summary of land cover specific snow properties 51
5.3 Land cover areal-weighted tundra study site SWE 54
5.4 Satellite Scale: snow survey SWE versus passive microwave estimated SWE 55
5.5 Local scale: snow survey SWE versus 37GHz–19GHz brightness temperature difference 58
5.6 Exploring the cause of extremely low estimated airborne SWE values 62
5.7 Summary 63
Chapter 6 Tundra Lake Ice Analysis Results 65
6.1 The influence of tundra lakes on microwave emission 65
6.2 Creating a regional tundra lake ice map from synthetic aperture radar 69
6.2.1 RADARSAT ScanSAR Wide backscatter intensity summary plots 69
6.2.2 Comparison of RADARSAT backscatter values with previous SAR lake ice studies 71
6.2.3 Interpretation of the principal component analysis 74
6.2.4 Accuracy assessment of the regional tundra lake ice map 76
6.3 Interpreting the passive microwave airborne data with the regional tundra lake ice map 80
6.4 Summary 84

Chapter 7 Conclusions, Limitations and Recommendations 86
7.1 Conclusions.....86
7.2 Study Limitations.....89
7.3 Recommendations for future research and SWE algorithm development 90

List of Figures

Figure 2.1 Electromagnetic Spectrum. 9
Figure 2.2 Backscatter intensity patterns observed for the three shallow arctic lakes. 23
Figure 3.1 Map of Hudson Bay: overview of the location of the tundra study site..... 25
Figure 4.1 NRC Twin Otter aircraft with mounted passive microwave radiometers. 32
Figure 4.2 Tundra study site flight grid and snow survey locations..... 35
Figure 4.3 An example of the stepped-line snow survey sampling pattern. 36
Figure 4.4 Photographs of each of the seven snow survey classes..... 39
Figure 4.5 A map of the lakes used to develop the lake ice training sites. 46
Figure 4.6 A schematic diagram of the steps to create a regional tundra lake ice map. 48
Figure 5.1 The relationship between mean ESC-30 measured SWE and mean estimated SWE. 50
Figure 5.2 Boxplot distributions of all snow depths, SWE, and snow density for the seven snow survey classes found within the tundra study site..... 52
Figure 5.3 36GHz brightness temperatures as a function of SWE..... 57
Figure 5.4 A photograph of snow survey site 98..... 59
Figure 5.5 The stepped-line sampling approach used at snow survey site 98. 60
Figure 5.6 Snow survey SWE versus high resolution airborne brightness temperature difference. 61
Figure 5.7 Airborne estimated SWE overlaid on a lake mask of the tundra study site. 62
Figure 6.1 Airborne brightness temperatures flight line segments: lakes versus no lakes. 65
Figure 6.2 Airborne brightness temperatures flight line segment: lakes versus measured SWE. 67
Figure 6.3 Backscatter intensity summary plots for different lake ice types..... 70
Figure 6.4 Comparison of RADARSAT-1 ScanSAR Wide backscatter intensity values with previous SAR lake ice studies in mid/late winter (March) 72
Figure 6.5 Comparison of RADARSAT-1 ScanSAR Wide backscatter intensity values with previous SAR lake ice studies in early winter (November). 72
Figure 6.6 Principal component analysis output images. 74
Figure 6.7 Regional tundra lake ice map. 77
Figure 6.8 Map of the tundra lake used to validate the performance of the supervised classification of the different tundra lake ice types..... 78
Figure 6.9 Airborne estimated SWE overlaid on the regional tundra lake ice map. 80
Figure 6.10 Distributions of airborne estimated SWE for both land and lake classes……. 81
Figure 6.11 Distributions of airborne estimated SWE for different lake ice types…….. 82

List of Tables

Table 2.1 Heritage of spaceborne passive microwave radiometer.....7
Table 2.2 Factors that influence microwave emission from snow.....10
Table 3.1 Brook's (2001) land cover classes of the tundra study site.....27
Table 4.1 Spaceborne brightness temperatures measured from March 6th to March 13th 2006.....31
Table 4.2 Calibration uncertainty of airborne brightness temperatures.....33
Table 4.3 The land cover categories recorded for the snow survey classification.....38
Table 4.4 The proportion of the study site devoted to each of the seven snow survey classes.....38
Table 4.5 Number of RADARSAT-1 images available in the Canadian Ice Service archive for the study site during the 2005-2006 winter season.....42
Table 4.6 Results of the georeferencing of the RADARSAT-1 time series.....44
Table 5.1 Summary of snow survey measurements for the entire tundra study site.....49
Table 5.2 Comparison of tundra study site summary statistics between the original SWE and snow depth sample size versus the larger combined sample sizes.....51
Table 5.3 The mean, median, standard deviation and range of SWE, snow depth and snow density for all seven snow survey classification classes.....53
Table 5.4 Landscape scale snow properties within the tundra study site.....55
Table 5.5 Tundra study site SWE versus brightness temperature estimated SWE.....56
Table 5.6 Ranges of airborne SWE estimates measured over lake features.....63
Table 6.1 Summary of the mean brightness temperatures, brightness temperature difference, airborne estimated SWE, measured SWE, and snow density for four locations along a 12km flight line segment that passed over lakes.....68
Table 6.2 The characteristics of each type of SAR imagery used in the comparison of backscatter values with previous SAR lake ice studies.....71
Table 6.3 The total variance explained by each principal component output.....75
Table 6.4 Percent of the total study site for each class in the regional tundra lake ice map.....76
Table 6.5 Results of the accuracy assessment of the regional tundra lake ice map.....79
Table 6.6 The mean airborne brightness temperatures and estimated SWE for all three different lake ice types and for the land class found in the regional tundra lake ice map.....84

Chapter 1
Introduction

1.1 Overview

The winter snowpack represents a significant storage component in the global hydrological cycle. Improved monitoring capabilities of global snow water equivalent (SWE) distribution and magnitude would lead to enhancements in agricultural production, forestry management, efficiency in hydroelectric energy water resource management and more accurate disaster/flood projections by providing a means of predicting spring runoff and forecasting seasonal water balances. Furthermore, accurate SWE datasets can be used for validation and act as valuable inputs into general circulation and hydrological models (Kite, 1995), as well as numerical weather prediction / land surface data assimilation schemes (Durand and Margulis, 2006). Changes in the distribution and extent of land based snow cover are considered to play an important role in determining the direction and magnitude for predicted global climate change (Frei et al., 2003). Therefore, developing a reliable and accurate means of monitoring global SWE is a current focus of the cryospheric research community.

1.2 Remote sensing of SWE

Conventional methods of in situ snow course measurements used for monitoring SWE in North America are time consuming, inefficient, sparsely distributed and spatially biased towards populated regions of the continent (Brown et al., 2000). A spatially continuous, temporally consistent SWE data source is needed to better monitor this important component of the hydrological cycle. The possibility of using remote sensing as a tool to improve global SWE monitoring is very appealing because of the extensive spatial coverage and frequent re-visit times of polar orbiting sensors. Passive microwave sensors are particularly suited to monitor snow properties at high latitudes during the winter months because of their ability to image day or night.

Efforts to use passive microwave remote sensing for snow monitoring began in earnest in the late 1970's with the launching of the Scanning Multi Channel Radiometer (SMMR) in 1978, which was followed by the Special Sensor Microwave Imager (SSM/I) in 1987, and the Advanced Microwave Sounding Radiometer for EOS (AMSR-E) in 2002. Much of today's science for monitoring snow with passive microwave remote sensors is based on work conducted in North America and Finland in

the 1980's and 1990's which focused on estimating snow water equivalent in both the prairie grassland and boreal forest / taiga environments using data from SMMR and SSM/I. Almost all contemporary SWE algorithms are based on the brightness temperature difference between the 37GHz and 19GHz frequencies found onboard both SMMR (18GHz), SSM/I, and AMSR. These algorithms all rely on the same basic principles: shorter wavelength radiation (37GHz) is more susceptible to volume scattering by the snowpack than the long wavelength frequencies (19GHz). The difference in brightness temperatures between these two frequencies (37GHz – 19GHz) is used to estimate SWE; the greater the difference, the higher the SWE estimates. However, this dual frequency relationship can be complicated because of the influence of snowpack properties including the presence of liquid water in the snowpack, changing snow density, grain size and the formation of wind slabs and ice lenses. In addition the difference may also be caused by other environmental influences such as the presence of overlying vegetation and changes in terrain. Despite the many complicating factors, researchers have used passive microwave remote sensors to monitor snow at hemispheric scales (Chang et al., 1987 and Tait, 1998). However, estimating snow properties at the hemispheric scale raises the issue of not accounting for the changing influences of different land covers, snow properties, and terrain types across an entire hemisphere and how these changes introduce errors into the SWE estimation. A slightly different approach is to work with landscape specific regions. The landscape specific approach takes into account the changing influences of many complicating factors by limiting SWE algorithm applications to areas of known snow properties, land cover and terrain types and applying appropriate algorithm coefficients to account for these influences. The landscape specific approach has the potential to be more accurate, but requires much more effort in the form of conducting detailed snow surveys for defining regional snow characteristics and collecting land cover and terrain information. Recent efforts to further expand the applicability of Environment Canada's landscape specific open environment SWE algorithm to the tundra environment of northern Canada have resulted in limited success. Snow surveys in the open tundra environment of the central Northwest Territories and northern Manitoba over the last four years have found that existing algorithms consistently underestimate tundra SWE (Derksen et al., 2005; Rees et al., 2005).

1.3 Research objectives

The objective of this thesis is to identify and explore the dominant factors that influence microwave brightness temperatures in the tundra environment and thereby drive the consistent underestimation of satellite microwave SWE retrievals.

To investigate the issue of passive microwave SWE underestimation in the tundra, Environment Canada conducted an intensive field campaign in March 2006, just south of Churchill, Manitoba. In situ measurements of snow depth, SWE, snow density, snow grain size and snow stratigraphy were recorded at 87 sites within a 25km by 25km grid located over the Marantz Lake region of the Hudson Bay Coastal Plains. Coincident multi-scale passive microwave airborne (70m resolution) and spaceborne (regridded to 25km resolution) data were measured at approximately 6.9GHz, 19GHz, 37GHz and 89GHz frequencies.

An initial consideration of the snow survey, landscape and airborne data suggest that the factors driving SWE underestimation can be broken down into three main sub-components: 1) extreme local scale snow variability on the open tundra plains, 2) spatially constrained snow deposition in vegetated land covers, and 3) the influence of lakes on microwave emission.

1. Extreme local scale snow variability on the open tundra plains

The first sub-component potentially contributing to passive microwave underestimation of SWE on the tundra is related to the horizontal complexity of the tundra snowpack. Extremely variable snow depths and SWE can be found on local scales ranging from several tens of meters to sub-meter extent, with wind-scoured snow-free hummocks immediately next to substantial snow deposits found in polygonal tundra wedge depressions and depressed tundra ponds. This extremely variable micro-scale snow deposition provides a challenge for determining a mean SWE from ground measurements and for satellite-scale SWE estimation. This micro-scale variability is on such a fine scale that it cannot be measured by any current passive microwave remote sensors due to the coarse resolution of all available data. Current satellite SWE algorithms quantify how much microwave energy is scattered by the snowpack, and relate this quantification to how much SWE is on the ground. In theory, if a large percentage of the wind-swept open land cover within the tundra environment is virtually snow-free, microwave emission from these surfaces undergo minimal scattering, and existing SWE algorithms subsequently predict very low SWE levels.

2. Spatially constrained snow deposition in vegetated land covers

The second sub-component potentially contributing to the passive microwave underestimation of SWE on the tundra is related to the re-distribution of blowing snow from the open tundra plains into vegetated land cover features such as forested creekbeds, lake edge willows, and isolated tundra tree-islands. The snow surveys show that more snow is deposited in these vegetated features compared to the open tundra. However, the percentage of total land cover devoted to vegetated features in a tundra environment is limited. Therefore, these spatially constrained, snow-trapping features likely have a minimal influence on most current spaceborne passive microwave measurements of the tundra, except in isolated vegetated areas and along the boreal forest / tundra transition zone, such as found in the Hudson Bay Coastal Plains.

3. Influence of lakes on microwave emission

It has been documented that longer wavelength passive microwave radiation can be influenced by the water below free-floating lake ice, resulting in a drop in brightness temperatures over lakes compared to adjacent land, while shorter wavelength radiation is largely influenced by the snow overlying the ice (Hall et al., 1981). Subsequently, the response of passive microwave frequencies can vary significantly between land versus lake due strictly to lake ice properties instead of snow. These differences between land and lake brightness temperatures are thought to be at least partly responsible for the very low SWE retrievals using contemporary passive microwave SWE algorithms developed for terrestrial land surfaces. High resolution passive microwave airborne data has shown that negative SWE retrievals are common over some tundra lakes. Negative SWE retrievals from some lakes could in theory contribute to an underestimation of SWE at the satellite scale because lake cover fraction can account for up to 40% of the land cover in a tundra environment (Duguay et al., 2005). The high resolution airborne data collected for this study is used to investigate the extent to which the snow over lakes influences the brightness temperatures relative to the properties of the lake ice itself.

1.4 Research significance

The importance and benefits of improving current methods of SWE monitoring around the world has already been mentioned in section 1.1. The identification of the three sub-components that likely contribute to the underestimation of SWE in a tundra environment is a major step towards understanding the fundamentals of microwave remote sensing of SWE on the tundra. Much work has already been done exploring the influences of complex snowpack properties and heterogeneous land

cover on passive microwave SWE estimation (for example, Hall, 1987; Kurvonen and Hallikainen, 1997; Goita et al., 2003). However, there has been very little work done to explore the influences of lakes on passive microwave SWE estimation, especially in a tundra environment where the lakes have different characteristics compared to southern water-bodies. Tundra lakes are generally shallow, and have much thicker ice compared to lakes that freeze over in more southerly latitudes. Duguay and LaFleur (2003) found the maximum ice thickness in the Churchill area to be about 1.6m, but tundra lake ice thickness has been documented to exceed 2 meters in depth in Alaska (Jefferies et al., 1994), and often completely freezes to bottom in all tundra environments. There is no current literature discussing how tundra lakes that have free-floating ice or are frozen to bottom affect passive microwave emission and subsequent SWE estimation and therefore this research provides insight on a unique and previously unexplored field of passive microwave cryospheric research.

1.5 Thesis outline

In Chapter 2, the context for this research is provided with a review of the literature related to tundra snow properties, passive microwave remote sensing of SWE and lake ice properties and a review on the use of synthetic aperture radar (SAR) for detection of lake ice growth histories. In Chapter 3, details concerning the physical setting and site description of the tundra study site are given. In Chapter 4, a description of the data collection and processing methods are discussed. In Chapter 5, the results of the analysis of the snow survey data and the multi-scale passive microwave brightness temperatures are provided. In Chapter 6, the results of the synthetic aperture radar lake ice and passive microwave brightness temperature analysis are given. In Chapter 7, the conclusions, limitation of certain aspects of this study and recommendations for areas of future research are given.

Chapter 2
Research Context

2.1 Overview of spaceborne passive microwave remote sensors

There are a number of characteristics of microwave remote sensing that distinguish it from optical and thermal imagery. These characteristics make passive microwave data very useful for the purpose of studying snow and ice:

1. Microwave remote sensors are not dependant on reflected solar radiation: measurements in both sunlight and absolute darkness are possible allowing for the recording of information in high latitude regions during the winter months when there are decreased amounts of solar illumination.
2. Traditionally, microwave remote sensors have been treated as all-weather capable, with the understanding that microwaves are able to pass through cloud cover because of their longer wavelengths compared to sensors in the visible portion of the electromagnetic spectrum. It is becoming increasingly clear, however, that atmospheric properties and surface temperatures have an effect on microwave frequencies (Tedesco and Wang, 2006; Markus et al., 2006). Relative to data collected in visible wavelengths, microwave remote sensors still have the added benefit of improved cloud penetration compared with visible imaging remote sensors, although all-weather capable without appropriate corrections may not be entirely true.
3. Microwave remote sensors measure emission from sub-surface features: depending on the wavelength used, these sub-surface features can include forest canopies, dry soils, snowpacks and lake ice.
4. Microwave remote sensors have an almost 30 year record of reliable and continuous data: while shorter than conventional datasets, this is a very long satellite time series with great potential for future change detection studies.

Efforts to use passive microwave remote sensing for snow monitoring began in the early 1970's using ESMR data, but became much more wide-spread with the launching of SMMR in 1978, SSM/I in 1987, and AMSR-E in 2002. Table 2.1 outlines the heritage of spaceborne passive microwave remote sensors used for snow monitoring and estimation of SWE. The sensors in Table 2.1 that are still

active today are SSM/I and AMSR-E. SSM/I is a total power, seven channel, four frequency, conical scanning passive microwave imager (Hollinger et al., 1990), which has been operating almost continuously on the Defense Meteorological Satellite Program (DMSP) Block 5D-2 flights F8-F15 (not F9) since June 1987. The second sensor that is still active is the more recently launched AMSR-E sensor, which is quite similar to SSM/I and is a total power, twelve channel, six frequency, conical scanning passive microwave imager (Kawanishi et al., 2003). AMSR-E has been operating continuously onboard the Aqua satellite platform, which was launched in May 2002.

Table 2.1 Heritage of spaceborne passive microwave radiometry used for the study of snow and ice.

Satellite & Launch Year	Sensor	Scanner Type	Frequency (GHz)	Swath Width (km)	Incident Angle (degrees)	Polarization	Instantaneous Field of View (km)
Nimbus - 5 (1972)	ESMR	Electronically Scanned Phased Array	19.35	3000	+/- 50	Horizontal	25 x 25 to 160 x 45
Nimbus-6 (1975)			37	1300		Dual Polarization	20 x 43
Nimbus-7 (1978) Seasat (1978)	SMMR	Conical Scanner	6.6 10.69 18.0 21.0 37.0	800	50.3	Dual Polarization	95 x 148 70 x 109 43 x 68 36 x 56 18 x 27
DMSP-F8 to F15 (excluding F9) (1987)	SSM/I	Conical Scanner	19.35 22.235 37.00 85.50	1400	53	Dual Polarization	45 x 70 40 x 60 30 x 38 14 x 16
Aqua (2002)	AMSR- E	Conical Scanner	6.925 10.65 18.70 23.80 36.50 89.00	1445	54.8	Dual Polarization	43 x 75 29 x 51 16 x 27 18 x 32 8.2 x 14 3.5 x 5.9

Due to the relatively low amounts of passive microwave energy naturally emitted from the Earth's surface, the Instantaneous Field of View (IFOV) of spaceborne passive microwave sensors are large. The IFOV is frequency dependent, and can be as large as 45km x 70km for 19GHz (SSM/I). Thus, a single passive microwave radiometer footprint can incorporate varying snow cover conditions and contain varying vegetative parameters and lake cover fraction all of which are known to influence brightness temperatures directly, and SWE indirectly. The National Snow and Ice Data Centre (NSIDC) developed the Equal Area SSM/I Earth Grid (EASE-Grid) with a resolution of 25 by 25km or 625km^2 (Armstrong and Brodzik, 1995). This common EASE-Grid format has provided a method in which different frequencies of passive microwave data with varying spatial resolutions, including

SMMR, SSM/I and AMSR-E, can be more easily compared and analyzed. The method used to resample passive microwave swath data to points on to the EASE-Grid involves an interpolation of the satellite swath brightness temperatures to increase the density of brightness temperature measurements within the swath reference frame (Armstrong and Brodzik, 1995). The brightness temperature for a given earth grid cell is then obtained from the oversampled array by the nearest neighbour method. When the data from all past and present spaceborne passive microwave sensors are combined, an almost 30 year historical dataset on a common grid is created. Users of EASE-Grid data should be aware that they are working with interpolated brightness temperatures and not swath data at native resolutions.

2.2 Fundamental concepts of passive microwave remote sensing of SWE

2.2.1 Remote sensing: electromagnetic energy

Lillesand and Kiefer (2000) define remote sensing as "the science and art of obtaining information about an object, area, or phenomenon through the analysis of data acquired by a device that is not in contact with the object, area, or phenomenon under investigation". All remote sensing involves the process of obtaining information indirectly by measuring electromagnetic energy.

All objects with a physical temperature above absolute zero (0K or –273 °C) emit some form of electromagnetic energy. Different types of electromagnetic wave energy can be classified based on two inversely related variables: the wavelength and frequency of oscillation. The wavelength is defined as the length of one cycle of oscillation measured as a distance between two adjacent wave-crests and is typically measured in meters (m) or nanometers (nm). The frequency refers to the number of cycles of a wave passing a fixed point per unit of time. The frequency is normally measured in hertz (Hz), megahertz (MHz), or gigahertz (GHz). The entire range of possible electromagnetic wave types is called the electromagnetic spectrum and is illustrated in Figure 2.1. Although names have been given to specific regions of the spectrum, (visible, radio-waves, microwaves), it should be noted that there are no strictly defined boundaries between different regions of the spectrum. Natural radiation in the microwave portion of the spectrum emanates from features on the earth and can be detected by a radiometer. Microwave radiation is a function of an object's emissivity and physical temperature, and is measured in degrees Kelvin (K) referred to as a brightness temperature (Hall et al., 1978). Microwaves have longer wavelengths than the near and

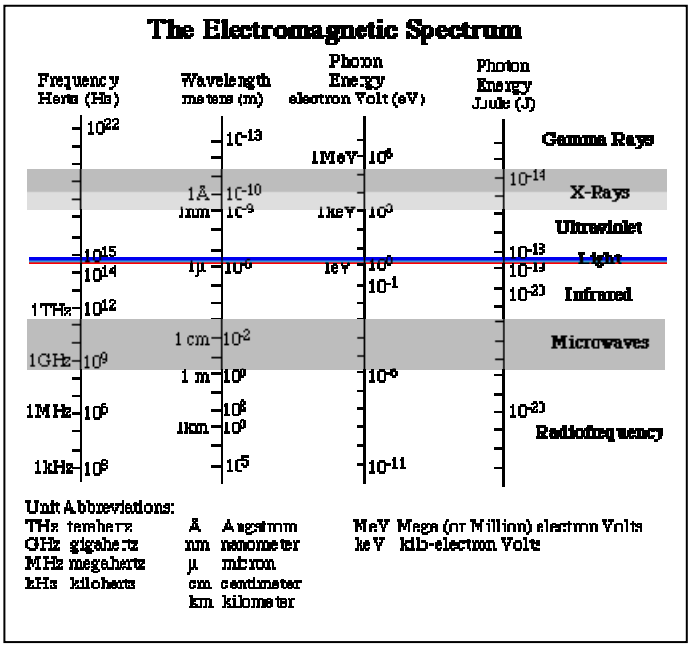

Figure 2.1 Electromagnetic Spectrum (Source: Wilson, 1996).

mid-infrared and visible portions of the spectrum and based on quantum mechanics theory the longer the wavelength of the energy involved, the lower its energy content (Lillesand and Kiefer, 2000). The implications of this relationship mean that remote sensing systems recording information in longer wavelengths must view larger areas of the earth in order to obtain an adequate energy signal, hence passive microwave remote sensing systems have much coarser resolution compared to optical and active microwave remote sensing systems. 'Active' remote sensing systems emit their own electromagnetic energy, such as synthetic aperture radar systems, and are not dependent on naturally reflected or emitted energy from the earth's surface. The understanding of electromagnetic radiation characteristics in terms of their wavelength and frequency is vital for understanding how electromagnetic energy at the microwave frequency interacts with different snowpack and lake ice properties, and how these can influence the estimation of snow water equivalent.

2.2.2 Factors that influence microwave emission

There are many factors that can influence the emission of microwaves from the Earth's surface, however, only those factors most relevant to cryospheric remote sensing will be discussed in this section. A full discussion on all of these factors is beyond the scope of this study, however, a more detailed description of the influence of snow and frozen lakes on microwave emission is provided in sections 2.2.3 and 2.4.4 respectively. Table 2.2 provides a brief summary of specific snow properties and environmental characteristics that influence microwave emission in snow covered environments, accompanied with a brief description of each influence with references to relevant literature on these topics. The first five factors in Table 2.2 are related to snow properties and the last three factors are related to environmental influences.

Table 2.2 Factors that influence microwave emission in a snow covered environment.

Factors	Description	Source(s)
Dielectric Constant	The dielectric constant is dependent on the amount of liquid water in the snowpack and as it increases it drastically increases the amount of absorption and emission of microwave energy that occurs by the snow and subsequently also the scattering of energy	(Hallikainen, 1992), (Mätzler, 1996)
Snow Grain Size	The scattering of microwave emissions increases with increasing snow grain size as the grain size approaches the size of the wavelength. This increased scattering lowers the brightness temperature of the snowpack. The largest snow grains are most common in depth hoar layers.	(Chang et al., 1976), (Hall, 1987), (Hall et al., 1991), (Koenig et al., 2004)
Snow Density	The density of snow (kg/m^3 or g/cm^3) is a measure of the mass per unit volume of snow, and is an indicator of the compactness of a snowpack. The density of snow varies over time and space, and is dependent on the amount of air in the interstices between individual snow crystals, which is a function of the temperature and wind during and after a snowfall event. In addtion, density tends to increase over time due to snowpack settlement. In theory, the larger and more interstices between snow crystals (lower density) the less scattering of microwave energy occurs. This explains why freshly fallen snow compared to a mature snowpack typically has the weakest sensitivty to microwaves.	(Gray, 1981), (Matzler et al., 1982)
Snow Structure (layering)	The layered characteristic of snow can significantly increase the complexity of interpretating passive microwave signals when the wavelength is comparable to the layer thickness, or if there is a significant difference between the dielectric properties of the layers	(Colbeck, 1991)
Snow Depth	The deeper the snow-pack becomes, the more snow crystals are available to scatter microwave energy away from the sensor, there-by lessening the amount of passive microwave energy received at the radiometers, and decreasing the brightness temperatures recorded by the sensors.	(Hallikainen, 1984), (Chang et al., 1997)
Vegetation	Vegetation can scatter, absorb and emit its own microwave energy. It can obscure the snowpack from remote sensors at shorter wavelengths and higher microwave frequencies, but can be penetrated by longer wavelength emissions.	(Kurvonen and Hallikainen, 1997), (Hallikainen, 2000), (Goita et al., 2003)
Topographic Relief	Topography can effect microwave emissions in two ways: Firstly, the elevation of the emitting surface (distance between the sensor and the surface) will dictate the atmospheric contribution to microwaves received by the sensor. Secondly, the emissions from terrain with variable topography interacts not only with the atmospere but with each other which can enhance the the overall emissions	(Mätzler and Standley, 2000)
Frozen Lakes	Compared to adjacent land, microwave brightness temperatures generally decrease over frozen water bodies with increasing wavelength because longer wavelengths have greater penetration through the ice and are influenced by the lower emissivity of the liquid water below the ice. In addition, it is thought that lake ice features such as bubbles and the presence of an ice/water interface (i.e. the lake is not frozen to bottom) also scatters the microwave emission further reducing the brightness temperatures. However, brightness temperatures should increase as the ice thickens and begins to emanate its own radiation reducing the influence of the liquid water below the ice.	(Hall et al., 1978), (Hall et al., 1981), (Chang et al., 1997)

2.2.3 Microwave emission from snow

Microwave emission passing through a snowpack originates mostly from the frozen surface below the pack, as well as from the snow itself. The emission passes through the snowpack and undergoes extinction losses through both absorption and volume scattering processes. The amount of scattering that occurs at higher frequency microwave radiation is largely dependent on the difference in dielectric properties between snow layer boundaries, which can be governed by changing snow grain size and snow thickness (Woodhouse, 2006). Snow grain size is an important factor controlling microwave emission from a snowpack. In a dry snowpack containing ice crystals of 0.5mm in radius, more absorption than scattering contributes to the extinction loss of microwave emission at frequencies less than 5GHz, while at frequencies above 20GHz, scattering becomes the dominant component of the total extinction loss (Ulaby et al., 1986). Microwave emission at frequencies between 5GHz and 20GHz undergo similar degrees of absorption and scattering, both contributing to the overall extinction loss. The difference in scattering processes at different frequencies is very much dependent on the microwave radiation wavelength. When the radii of snow grains approach a few hundredths of the microwave wavelength, volume scattering by the individual ice particles significantly decreases microwave emission (Chang et al., 1976). Therefore at lower microwave frequencies (e.g. 19GHz) where the wavelength is larger, the snow grains are not large enough to scatter any energy, and thus absorption becomes the dominant extinction process. However, in a dry snowpack very little absorption occurs, therefore the emission undergoes almost no extinction processes and snow is largely 'invisible' to longer wavelength microwave frequencies. At the higher microwave frequencies with shorter wavelengths (e.g. 37GHz), it is possible to 'see' the snowpack and discern between snow covered and snow-free ground by measuring the amount of microwave radiation scattered by the snow. The differences in snow grain characteristics found at different depths within a snowpack due to metamorphism and different snowfall events leads to the formation of snowpack boundaries and layering. The layering of the snowpack can add a significant level of complexity in interpreting passive microwave emission for SWE estimation when the emitting radiation wavelength is comparable to snow layering thickness, or when there are notable dielectric contrasts between different snow layers (Colbeck, 1991). Snow depth is also an important factor which can control the influence of snow grains on microwave emission. The deeper the snow-pack becomes, the more snow crystals are available to scatter microwave energy away from the sensor, there-by lessening the amount of passive microwave energy received at the radiometers, and decreasing the brightness temperatures recorded by the sensors (Chang et al., 1997). However, as the

snowpack continues to get deeper, Mätzler et al. (1982) found that deep snowpacks could have higher brightness temperatures than shallower snowpacks because the deep snowpacks begin to emanate their own microwave radiation.

Overall though, most SWE retrieval algorithms were designed for shallower snowpacks and are based on the same basic principles: as the SWE increases, the brightness temperature of short wave radiation typically decreases, and it is this negative relationship which is used to estimate SWE using the 37GHz passive microwave frequency. However, this negative relationship only exists for shallow snowpacks, with deeper snow the relationship becomes positive and passive microwave SWE retrievals become more complex.

2.2.4 Passive microwave SWE retrieval algorithms

Almost all contemporary SWE algorithms are based on the brightness temperature difference between dual microwave frequencies. Dual frequency algorithms make use of one long wavelength and one short wavelength frequency. The 'snow insensitive' long wavelength frequency effectively acts a reference value because it encapsulates the variability in radiation due to other influencing parameters other than the snowpack, such as the atmosphere or change in ground cover (Woodhouse, 2006). Therefore, any change in the short wavelength radiation that is not explained by the 'snow insensitive' long wavelength radiation is likely due to changes in snowpack properties (excluding environmental influences), including variations in SWE. The 19GHz and 37GHz frequencies found onboard SMMR, SSM/I, and AMSR-E are the most commonly used frequencies for SWE algorithms. These algorithms all rely on the same basic principles: shorter wavelength radiation (37GHz) is more susceptible to volume scattering by the snowpack than the stable long wavelength radiation measurements (19GHz). The difference in brightness temperatures between these two frequencies (37GHz – 19GHz) is used to estimate SWE; the greater the difference, the higher the SWE retrievals returned.

2.3 Arctic and tundra snowpack properties relevant to passive microwave SWE estimation

It is difficult to conduct snowpack research in the arctic and subarctic environment, largely due to the remoteness and inaccessibility of the region. Despite the challenges, there has been work conducted in Siberia, Norway, the north slope of Alaska and in the subarctic tundra and arctic archipelago of Canada that characterizes arctic and tundra snow. Current and past research in these areas has shown that tundra snow cover is quite different from snow cover in more southerly latitudes in its distribution, structure, and snow crystal metamorphism.

2.3.1 Arctic and tundra snow distribution

Vegetation on the Canadian tundra, in the form of tall shrubs and sparse forests, trap wind-blown snow which leads to increased rates of snow deposition (Pomeroy et al., 1997). These findings are supported by work completed by Liston and Sturm (1998), on the Alaskan north slope and by Boudreau and Rouse (1994) in the Hudson Bay Lowlands and by the results of the March 2006 snow survey conducted for this study. In the areas where there are no tall shrubs or sparse forests, the snow distribution is determined mainly by the terrain topography (Hirashima et al., 2004). Vegetation sparse areas are found in the far northern latitudes of Norway, Alaska, Siberia and the Canadian arctic. Wind scour and sedimentation of wind eroded snow particles produce a tundra snow cover highly variable in density and depth with numerous exposed areas, drifts, dunes and sastrugi (Gray, 1981). In the tundra environment absent of vegetation, snow is re-distributed by wind and is typically deposited in drifts on concave and leeward slopes, and in topographic depressions as was shown in Norway by Bruland et al., 2001; in Alaska by Liston and Sturm, 1998; and in the Canadian sub-arctic by Rees et al., 2005 and the Canadian arctic islands by Woo, 1998. Most of the literature on the distribution of arctic and tundra snow suggests that it is highly variable, with large volumes of snow stored in drifts induced by vegetation and topography. The snow mass deposited in these arctic / tundra features can be 2 to 3 times more than that found in open vegetation-free land cover (Essery et al., 1999 and Woo, 1998). The hydrologic significance of this spatially constrained snow distribution is dependent on the scale of study.

The spatially constrained distribution of snow is very important to consider from both a remote sensing point of view, and when conducting in situ ground measurements. When conducting snow

surveys, it is paramount that the sample sites are representative of the overall study area. If little is known about the snow distribution and land cover in a particular area, there is risk that the ground measurements become skewed by over-sampling of the snow-trapping features, or vice versa, by over-sampling the wind blown snow-free areas. From a passive microwave remote sensing view point, these snow-trapping features are typically not as important to consider, unless they account for a substantial portion of the imaging footprint of the radiometer.

2.3.2 Arctic and tundra snow structure and grain size

The variability of vegetation cover and terrain in the tundra environment not only influences the distribution of snow, but also influences the snow structure and grain size of the snowpack. Sturm et al. (1995) describe the tundra snow cover as a thin, firm, wind blown snow cover with a depth range of 10-75cm and an average density of ~0.380g/cm^3, with layers of depth hoar overlaid with wind slab layers that are related to individual winter precipitation events. The development of depth hoar is dependent on the temperature gradient in the snowpack from the base to the surface, the larger the temperature gradient, the greater the rate at which water vapour transport and snow metamorphism can occur, producing more depth hoar in the snowpack (Sturm and Benson, 1997). The presence of ground vegetation at the base of the snowpack can act as a thermal insulator to the frozen soil, keeping the ground temperature substantially warmer than vegetation free ground, further intensifying the snowpack temperature gradient (Sturm et al., 2000). The arctic and tundra environments regularly have extremely cold air temperatures which intensify the temperature gradient between the cold arctic air and the warmer ground necessary for depth hoar development, making this a common high latitude snowpack feature. In areas with little to no vegetation, the snowpack structure will invariably be shallower, contain fewer layers, and have smaller snow grains.

Sturm and Liston (2003) noted that in a tundra environment, lakes have fewer snow layers than on land, and that lake snow had a much higher ratio of wind slab to depth hoar, while land snow with vegetation, comparatively had a higher ratio of depth hoar to wind slab. The findings of Sturm and Liston (2003) can be quite significant when one considers that the total land cover occupied by lakes and ponds in the tundra environment can vary from 25% on the north slope in Alaska (Sellman et al. 1975, cited in Sturm and Liston, 2003), to almost 40% of the land cover in other tundra regions (Duguay et al., 2005).

Vegetation, topography and lakes are the dominant factors that can indirectly influence microwave emission in this environment. These factors influence the snow properties, which then directly influence the microwave emission and scattering. The most important snow properties most likely influencing microwave emission in an arctic / tundra environment include: the heterogeneous snow distribution, multiple wind slab snow layers, and the presence of large depth hoar crystals.

2.4 Passive microwave remote sensing in the arctic and subarctic

There has been limited research involving passive microwave remote sensing of SWE in the arctic and subarctic environment because of the difficulties associated with collecting ground-based SWE measurements for validation. The majority of research that has been conducted has been largely restricted to the north slope of Alaska, the Canadian arctic islands, the central Northwest Territories, and northern Manitoba. Research has shown that complications with using passive microwave remote sensors to estimate SWE in this environment are due to the unique characteristics of the tundra snowpack and its distribution as discussed above, and most likely due to the influence of microwave emission from the high number of lakes and ponds. In-addition, Hall et al. (1991), propose that the decreasing density of vegetation as you advance further north may explain a decrease in passive microwave emission over the tundra environment compared to forested environments, because forest vegetation is known to emit its own energy in-addition to the ground emission.

Boudreau and Rouse (1994) conducted algorithm testing of passive microwave monitoring of snow water equivalent in a tundra environment approximately 60km from the location of the tundra study site used in this analysis. Their findings state that Environment Canada's dual frequency SWE algorithm consistently underestimated SWE with the most probable reasons being 1) the contamination of the spaceborne imaging footprint with the influence of the sea ice on spaceborne brightness temperatures near the Hudson Bay coast, 2) the fact that thin snow cover on lakes was not incorporated into the tundra snow surveys, 3) the effects of basal ice on brightness temperatures which was found extensively in the sedge tundra environment, and 4) the limited extent of the snow surveys may not have been representative of the actual snow cover within the passive microwave radiometer's IFOV.

2.4.1 Passive microwave remote sensing of subarctic depth hoar dominated snowpacks

Exploring the enhanced degree of snowpack scattering of passive microwave energy due to the increased presence of depth hoar in a tundra snowpack has been conducted in northern Alaska. Hall (1987) used a two layer radiative transfer model to calculate the microwave brightness temperatures of a modeled snowpack with and without a depth hoar layer. The correlation between observed satellite brightness temperatures for the northern Alaskan tundra snowpack and calculated brightness temperatures of a modeled snowpack improved when a depth hoar layer was added to the model. These results suggest that grain size and depth hoar layer thickness have a prominent effect on the low brightness temperatures observed over the northern Alaskan snow cover (Hall, 1987). However, the effect of depth hoar on reducing the emissivity of a snowpack due to volume scattering has been observed to maximize at a depth hoar layer thickness of approximately 30cm for the 37GHz frequency (Sturm et al., 1993). For depth hoar layers with a thickness greater than 30cm no more volume scattering occurs, instead, self-emittance by the overlying fine-grained snow begins to increase the emissivity from the snow surface, but this increase occurs only at one tenth the rate that volume scattering decreases the signal (Sturm et al., 1993). The increased volume scattering of the microwave signal due to the presence of depth hoar leads to an overestimation of SWE because a snowpack with a high proportion of depth hoar appears radiometrically similar to a much deeper snowpack with more SWE because they both undergo similar amounts of microwave scattering. However, the increased scattering from the depth hoar dominated snowpack is strictly because of the larger grain size, and not necessarily because of more SWE, thus existing algorithms falsely predict higher SWE values from depth hoar dominated snowpacks.

Koenig and Forster (2004), found that their own algorithm specifically developed for their study in the Kuparuk river watershed, Alaska, along with three existing SWE estimating algorithms developed by Chang et al., 1987; Goodison, 1989; and Tait, 1998 were capable of determining the average SWE of arctic snowpacks with significant depth hoar over large geographic areas when averaged over a period of days, indicating that depth hoar in snowpacks do not cause tremendous problems over large spatial averages. However, closer examination of the results of Koenig and Forster (2004), indicate that indeed over larger spatial averages existing algorithms can estimate SWE, but they may be producing these results for the wrong reasons. When the four different SWE algorithms were

examined on a pixel-by-pixel basis with in situ SWE measurements, Koenig and Forster (2004), found that every algorithm tested consistently overestimated which supports previous documentation for tundra snow covers. And at the within pixel, sub-watershed scale, Koenig and Forster (2004), found that the spatial distribution of predicted SWE from Tait's algorithm did not match that of the measured SWE, producing a pattern of overestimation occurring near the coast and underestimation occurring in the foothills which was opposite of what was actually measured. Despite this reversed snow distribution a good basin wide SWE average was still produced. This is a good example of how accurate SWE retrievals may be possible for the wrong reasons over large spatial averages. However, Koenig and Forster (2004), also found that the Goodison and Chang algorithms were able to predict similar SWE distributions compared to measured SWE, but the magnitude of those predictions were too high. Therefore, with re-calibration to account for the influence of depth hoar, existing SWE algorithms may indeed be able to predict tundra SWE magnitude.

2.4.2 Issues of scale with passive microwave remote sensing of tundra snow distribution

The distribution of snow on the tundra is typically controlled by vegetation and topography, as discussed in section 2.3.1. Most of the literature on the distribution of arctic and tundra snow suggests that there are large volumes of snow stored in drifts created by vegetation and topography. The hydrologic significance of this spatially constrained snow distribution is dependent on the scale of study. The large amount of snow stored in drifts may be hydrologically significant at the local scale, but when working at passive microwave spaceborne satellite scales it is important to re-assess this importance based on the spatial percentage of the environment these drifts represent (Rees et al., 2006). Woo (1998) found that gullies and north facing slopes had 2 to 3 times the snow of open areas, but the areas only accounted for approximately 10% of the total land cover, while Rees et al (2006) found similar results with high slopes containing very deep snow, but accounting for only approximately 5% of the total land cover. In these situations, the constrained distribution of large amounts of snow are not necessarily representative of the regional snow cover conditions found within a single passive microwave footprint, and therefore may not be hydrologically significant at the satellite scale. However, in this study of the Hudson Bay Coastal Plains, tall snow-trapping vegetation accounts for approximately 30% of the total land cover and contains 2 to 3 times as much snow as open tundra areas. These snow-trapping features represent a much larger proportion of the

land cover found within a passive microwave radiometer's IFOV, and thus in these situations, the hydrological significance of SWE in tall vegetation and its influence on microwave emission should be accounted for in satellite SWE estimation.

2.4.3 Influence of freshwater lakes on passive microwave SWE estimation

Not until Derksen et al. (2005) and Duguay et al. (2005) has anyone recently addressed the need to study the influence of frozen freshwater lakes and ponds on passive microwave emission at the sub-pixel scale. With the recent push to extend the use of passive microwave SWE estimation into the tundra environment where lake-cover fraction is substantial, it is very important to re-visit the microwave properties of frozen tundra lakes. The majority of published research concerning the influence of frozen lakes on microwave emission measured by high resolution radiometers was conducted several decades ago with the majority of it taking place in non-tundra environments (Schmugge et al., 1974; Swift et al., 1980; Hall et al., 1978; and Cameron et al., 1984).

Lower microwave frequencies with long wavelengths pass right through the overlying snow as if it were invisible making these frequencies useful for studying sub-snowpack lake ice compared to the shorter wavelengths, which sense only the upper layers of the ice and overlying snow (Hall et al., 1978). Refer to section 2.2.3 for further details on the penetration characteristics of microwave frequencies for snow. Longer wavelength microwave emission emanates from deeper within the ice and/or from below the ice. Hall et al. (1981) stated that the microwave emission from freshwater ice can be affected by the ice/air interface, bubbles in the ice, ice/water interface, and the ice thickness but did not quantify these effects. Hall et al. (1981) also found that bubbles unevenly distributed throughout the ice across a lake can lead to non-uniform brightness temperatures across that lake. Cameron et al. (1984) found that in subzero temperatures, the microwave signature of a frozen lake remains constant over the course of a day. Derksen et al. (2005) and Duguay et al. (2005) noted that the brightness temperatures over some frozen lakes are higher at 37GHz than 19GHz, which is a reversal of brightness temperature patterns measured over most land surfaces, and as a result the current brightness temperature difference algorithms used to estimate SWE over land can produce negative SWE values over lakes.

Liquid water has a very low emissivity compared to ice (Hall et al., 1978), therefore a frozen water body with liquid water below the ice will have much lower microwave emission at longer

wavelengths and subsequently lower brightness temperatures compared to adjacent land. However, over the course of the ice-growing season, the growth of ice and subsequent increase in its thickness increases the brightness temperature compared to thinly iced lakes (Swift et al. 1980). The thicker ice reduces the influence of the lower emissivity of liquid water below the ice and emits its own microwave energy thereby increasing the brightness temperatures over water bodies. However, in tundra and arctic environments many shallow lakes freeze completely to their beds, but the impact of this grounded ice on passive microwave brightness temperatures is presently unknown (Derksen et al., 2005). However, one may hypothesize that lakes frozen to bottom likely have higher brightness temperatures compared to lakes with free-floating ice because the influence of sub-ice liquid water on emissivity has been removed.

2.5 Arctic and subarctic lake ice information from synthetic aperture radar

As discussed in section 2.4.3, the influence of some freshwater lakes on microwave brightness temperatures has been documented, however, the influence of tundra lakes has not. Furthermore, the influence of lakes completely frozen to bed, a common trait in the Hudson Bay Coastal Plains (Duguay et al., 2002), is unknown. During the March 2006 field campaign, no lake ice information was collected and during the post-field campaign examination of the airborne microwave brightness temperatures, a markedly different response in brightness temperatures to different tundra lakes was observed mostly in the longer wavelength frequencies. It was hypothesized that the different response was due to differences in lake ice properties, because the measured snow properties were quite similar. Therefore, information on lake ice properties was desired, and a review of the literature found that this was potentially possible using a winter time series of synthetic aperture radar (SAR) imagery.

The usefulness of SAR systems, such as the European Remote-Sensing Satellites (ERS-1 and ERS-2) and the Canadian RADARSAT-1, for monitoring sea and lake ice has been shown by the United States National Ice Center (NIC) and the Canadian Ice Service (CIS) for many years (Bertoia and Ramsay, 1998). The SAR systems offer many benefits for ice monitoring and research applications which are very similar to the advantages of passive microwave systems already discussed in section 2.1, but with the added advantage of higher spatial resolution.

Active microwave data are sensitive to a number of characteristics which include: surface roughness, moisture and dielectric constant, land / water boundaries, anthropogenic features and topography. The sensitivity to surface roughness and changes in dielectric properties are the characteristics that make RADARSAT quite useful for ice monitoring. Sea ice typically has a rough surface (except immediately after freeze-up) and therefore more signal is returned to the satellite compared to the surrounding open water. Different types of ice have different surface roughness characteristics and different dielectric properties, making it possible to distinguish between more than one type of sea ice. Due to the longer wavelength of the microwave frequency used by RADARSAT (5.3GHz), and the low dielectric constant of dry snow, an overlying snowpack on the ice is largely transparent to the satellite signal and does not interfere with the monitoring of ice conditions (Ulaby et al., 1982). It is these same unique penetrating properties which make RADARSAT quite useful for freshwater ice studies. Freshwater ice typically has a lower dielectric constant than sea ice, and therefore the 5.3GHz microwave frequency used by the RADARSAT satellite has a greater penetration depth over freshwater ice than sea ice and can be used to identify lake ice properties well below the surface (Ulaby et al., 1986). Sea ice typically has a higher dielectric constant because of the presence of small brine pockets in the ice which increase the dielectric constant and reduces radar ice penetration (Ulaby et al., 1982).

The penetration depth of the 5.3 GHz frequency in pure ice at -10°C can be up to 10m (Ulaby et al., 1982). However, the presence of pure water or ice in a natural environment is unlikely, and therefore the real penetration depth would be far less than 10m, but still greater than the documented penetration depth of 0.1m to 0.6m for multi-year sea ice (Ulaby et al., 1982). Even in the most extreme North American environments it would be unlikely for lake ice to far exceed 2m in thickness, well within the pure ice depth penetration maximum, thus making RADARSAT a likely tool for measuring sub-surface lake ice characteristics.

Jeffries et al., (1994), Morris et al., (1995) and Duguay et al., (2002) analyzed a winter time series of SAR images of shallow tundra lakes to monitor changes from low backscatter in early winter, to progressively higher backscatter as the winter progressed, and if the lake froze to bed, a subsequent return to low backscatter values. Both Morris et al. (1995) and Jeffries et al. (1994) used ERS-1 SAR (C band-VV) low resolution imagery that was distributed by the Alaska SAR facility (ASF). The ASF low resolution imagery has 100m pixel spacing and a 240m resolution with a swath width of 100km and incident angles ranging from 20-26°. Duguay et al. (2002) used RADARSAT SAR (C band-HH)

standard beam modes (S1-S7) which has 12.5m pixel spacing and a 25m resolution with a swath width of 100km and incident angles ranging from 20-49°.

To understand why radar returns vary so much between lakes, and as the winter season progresses, one must examine the lake ice structure and look for the presence of liquid water below the ice. Tundra lake ice can be clear, contain bubbles or a combination of both. It is common for shallow tundra lakes to have a layer of clear ice overlying ice containing tubular bubbles (Jeffries et al., 1994, Morris et al., 1995, and Duguay et al., 2002). The top layer of clear ice represents the earlier stages of ice growth, when the concentration of gases in the lake water are not very high and the gases that are absorbed during ice growth can be expelled from the ice back into the water. The clear ice allows for penetration of incoming radar energy which interacts with the liquid water below the ice. The strong contrast in dielectric properties between the ice $\varepsilon_I' = 3$ and water $\varepsilon_I' = 80$ (Ulaby et al., 1986), results in a specular reflection (Morris et al., 1995). This explains why during the early part of the winter season, the backscatter intensity from shallow tundra lakes ice is typically low. However, as the winter season progresses the deeper layers of lake ice containing elongated tubular bubbles continue to increase in size causing a steady increase in backscatter values. As the amount of liquid water present in a lake decreases over the winter (more ice than water), the lake becomes supersaturated with gases and the ice cannot expel the gases absorbed during growth back into the water resulting in the formation of large bubbles (Morris et al., 1995). These bubbles are thought to act as forward scatters of incoming radar energy, which leads to a "double-bounce" radar return, which results in a significant portion of the radar energy returning to the satellite (Kozlenko and Jeffries, 2000). This double-bounce refers to the initial interaction of the radar energy with the tubular bubbles, which then gets forward scattered to the ice-water interface where its second interaction occurs with the sharp discontinuity in the dielectric characteristics of ice and water resulting in a very strong radar return but this time directed towards the satellite because of the re-direction of the bubbles. And finally, it is the dielectric characteristics and bottom composition that explain why lakes that freeze to bottom have much lower radar backscatter compared to lakes that are free-floating. The amount of tubular bubbles remain the same in the ice, but the second bounce in the double-bounce reaction no longer occurs without the sharp discontinuity in the dielectric constant at the ice-water interface. Instead, the dielectric constants for the frozen lake bed and the lake ice are similar, and therefore the radar energy continues to penetrate and is absorbed into the ground (Jeffries et al., 1994, Morris et al., 1995, Duguay et al., 2002, and Duguay and Lafleur, 2003). The amount of absorption is dependent on the composition of the lake bottom. Rocky lake bottoms create a rougher, harder interface compared to

soft organic bottoms and hence less radar energy is absorbed into the ground, resulting in a higher radar return measured at the satellite (Duguay and Lafleur, 2003).

The work by Jeffries et al., (1994), Morris et al., (1995) and Duguay and Lafleur (2003) found that a single winter SAR image was not sufficient to identify lakes that have frozen to bottom with any certainty because of the variation in backscatter intensity between lakes with different bottom compositions and because lakes with free-floating ice, devoid of bubbles, would likely have very similar backscatter responses to lakes that are frozen to bottom. Therefore, to accurately measure lake ice information from SAR, a time series is needed to plot the change in backscatter for each individual lake throughout the winter season. The typical method used to assess the variation in backscatter intensity from a time series of SAR images is to plot out the backscatter intensity sigma nought (σ°) values for a select number of lakes in a study area and match the fluctuations in σ° with changes in ice conditions observed by field measurements. Two distinct backscatter intensity patterns have consistently been defined using these methods: one pattern provides a good indication of a lake that freezes to bottom later in the winter season and the other pattern indicates that a lake has free-floating ice. These two patterns of backscatter intensity plots have been observed in multiple studies (Jeffries et al., 1994, Morris et al., 1995, and Duguay et al., 2002). A third backscatter intensity pattern observed in each of these studies can be interpreted as two different ice types. One interpretation of this third backscatter intensity pattern is of a lake that freezes to bottom early in the season and remains frozen until melt, and the other interpretation is the backscatter return from a lake with clear, bubble-free ice. Figure 2.2 illustrates the approximate backscatter intensity patterns observed by Morris et al., (1995) for three shallow arctic lakes 1) a free-floating Barrow lake, 2) a late season grounded 'B' lake, 3) an early season grounded 'C' lake, over the 1992/1993 winter season (November – March). Morris et al., (1995) used ERS-1 SAR images with a spatial resolution of 240m and 100m pixels. The backscatter intensity values illustrated in Figure 2.2 are the mean of 9 ERS-1 pixels. These same backscatter intensity patterns are consistently defined among the different SAR lake ice studies already mentioned, however, the magnitude of the backscatter intensity can differ between studies. Despite the difference in magnitude, the consistency of the backscatter intensity patterns provides confidence in the feasibility of using a winter time series of RADARSAT-1 ScanSAR Wide images to provide a post-field campaign indication of whether a lake was frozen to bottom or not with out having conducted any field observations during the study time period.

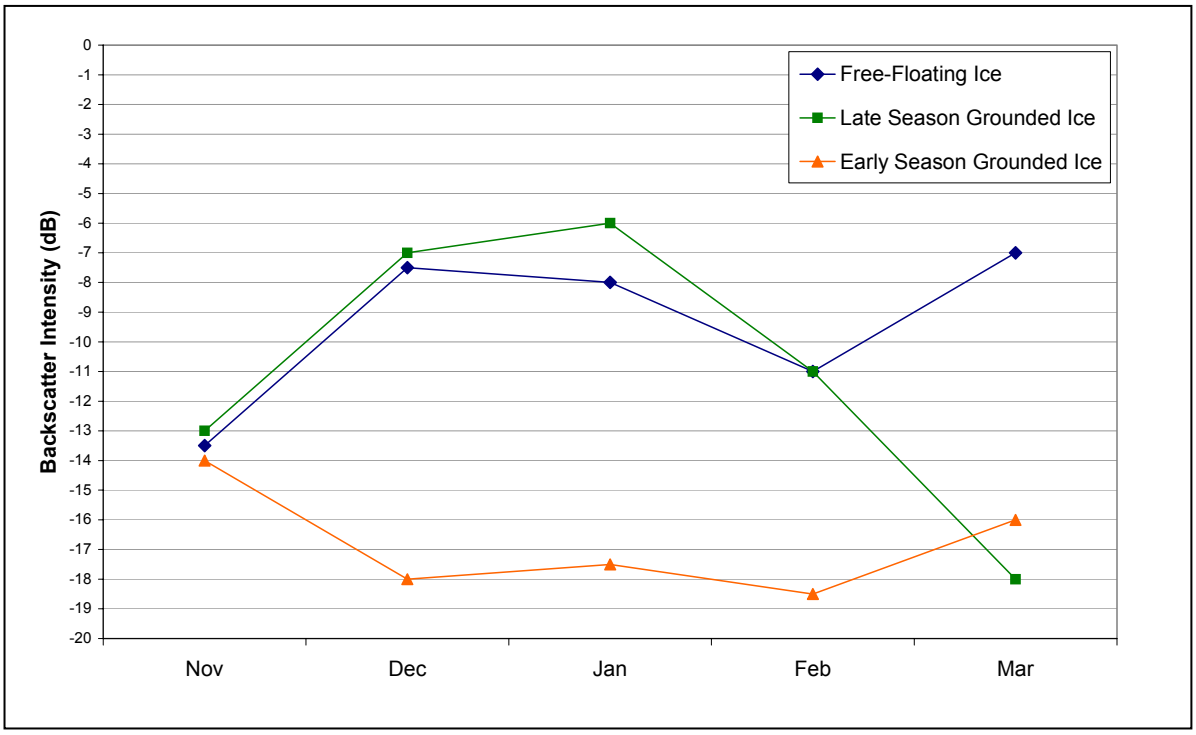

Figure 2.2 Backscatter intensity patterns observed over the 1992/1993 winter season (November – March) for the three shallow arctic lakes by Morris et al. (1995).

2.6 Summary

To identify the dominant factors that influence microwave brightness temperatures in the tundra environment, it is necessary to understand what are the controlling factors influencing microwave brightness temperatures in regions where passive microwave SWE retrievals have been successful. Chapter 2 provides a good overview on many of these known influences, with greater detail given to those most relevant to the tundra environment including, snow structure (layers), SWE, snow grain size and microwave emission from lakes. All of these influences coupled with the discussion on the spatially constrained nature of the tundra snow distribution provide a good indication of why current methods of SWE estimation underestimate for the tundra environment. The potential of using a SAR winter time series to provide lake ice information to assist in the interpretation of the airborne microwave brightness temperatures is discussed and provides a means of gaining valuable lake ice information well after the field campaign has been conducted.

Chapter 3
Tundra Study Site Description and Physical Setting

3.1 Hudson Bay Coastal Plains

The Atlas of Canada has created a classification of the entire Canadian landmass which subdivides the country into 53 unique ecoprovinces based on physiographic similarities (National Scale Frameworks Hydrology, 2003). The tundra study site falls within the Hudson Bay Coastal Plains ecoprovince, which is a subcomponent of the Hudson and James Bay Lowlands. The Hudson Bay Lowland contain one of the most southerly expanses of tundra in the world outside of the alpine environment and its extent is depicted in Figure 3.1. The Hudson Bay Lowland is a vast plain that slopes gently toward the sea at a gradient of less than 1m/km (Parks Canada, 1977). Up to 85 percent of the region is muskeg and is one of the largest expanses of peat in the world (Parks Canada, 1977). This region borders the northern extent of the treeline, separating the treeless tundra from the boreal forest with a mosaic of forest and tundra. Taller vegetation tends to grow on well-drained riverbanks and lake shores making for linear patterns of vegetation growth. The Hudson Bay Coastal Plain is a land of water. Water covers the land in shallow lakes and ponds, in rivers and streams, and in bogs and fens; where up to 50 percent of the surface can be covered by water (Parks Canada, 1977). There is even water below the surface with over 90 percent of the study area underlain with continuous permafrost and almost 20 percent of the surface underlain with ground ice (The State of Canada's Ecosystems in Maps, 2002).

3.2 Tundra study site

The tundra study site for this thesis is located 60km south of Churchill, Manitoba and 60km from the west coast of Hudson Bay as illustrated by Figure 3.1. The extent of the study site is approximately 25km x 25km (625km^2) and encompasses the EASE-Grid cell centered at 58º 18´N, 94º 11´W. The tundra study site was sampled between March 6th and March 13th 2006.

Figure 3.1 The map of Hudson Bay provides a regional overview of the location of the tundra study site. The location of the study area is highlighted by the black circle, and the extent is outlined by the square. The extent of the Hudson Bay Coastal Plain is shaded grey

3.2.1 Climate and weather

The climate normals (1971-2000) for the study site are taken from the closest climate station found at the Churchill airport located at 58° 44' N, 94° 3' W (National Climate Data, 2007). The mean annual temperature from 1971-2000 is -6.9°C, with January being the coldest month (-26.7°C) and July the warmest (12°C). The normal daily air temperature in the month of March is -19.5°C and the wind speed is 20.4km/h. During the study time period an automated weather station located within the boundaries of the study site measured an average air temperature of -13.2°C recorded hourly compared to the average air temperature of -10.8°C measured at the Churchill climate station. The difference between the automated station within the study site and Churchill's climate station indicate that the inland tundra study site may experience slightly cooler air temperatures than those measured near the coast, and so the climate normals for the study site may actually be slightly cooler. The automated weather station within the study site recorded a minimum and maximum air temperature of -24.1°C and -5.2°C during the study period. It is important to note that there were no days with above zero temperatures, because even the slightest amount of liquid water within the snowpack due to melt can have a profound influence on the brightness temperatures measured from the snowpack making it impossible to estimate SWE from passive microwave data. During the study period from March 6th to March 13th 2006, the Churchill airport reported a total of 2mm of precipitation which occurred on the 9th and 10th of March. This trace amount of snow accumulation means that observed changes in satellite brightness temperatures during the study time period are not due to any winter precipitation events.

3.2.2 Land cover information

Vegetation in the Hudson Bay Lowlands exists as a complex mosaic of tundra and treed communities across the landscape as a result of a wide variety of factors that influence plant growth, reproduction and dispersal. The distribution and composition of plant communities present in this region are determined by broad-scale conditions such as climate, geology, soils, length of the growing season and isostatic uplift; and at more local scales, the temperature, snow cover, drainage, water chemistry, slope and aspect (Brook, 2001). These various influences contribute to a high variability in vegetation across the landscape. The three major vegetation types are fen, bog and upland, with the fen communities dominating the geologically younger sites near the coast and the bog and upland communities more common further inland (Brook, 2001).

Brook (2001) used a combination of Landsat-5 TM imagery (30m resolution) and extensive ground data collected at 600 sites over 3 years in Wapusk National Park and the Cape Churchill Wildlife Management Area of northern Manitoba to characterize the land cover of the region and to create a land cover map. The tundra study site visited in this study overlaps a portion of the Cape Churchill Wildlife Management Area of northern Manitoba and therefore a detailed land cover map of the study area is available. Brook (2001) sub-divided the Cape Churchill Wildlife Management Area into 16 vegetation classes using a multivariate analysis based on the field vegetation surveys. These 16 classes were then used to classify the Landsat-5 TM imagery for the study area. A subset of the classified image was provided by Ryan Brook to assist in this analysis. The extent of the subset slightly exceeds the boundaries of the EASE-Grid cell centered on the tundra study site (58º 18´N, 94º 11´W). Out of the 16 classes in Brook's (2001) land cover map, 9 were identified within the study area and these classes are listed in Table 3.1, accounting for 99.7 percent of the total land cover within the tundra study site with the remaining 0.03 percent not classified. Similar to the rest of the Cape Churchill Wildlife Management Area, the three dominant terrestrial land cover types found within the tundra study site are fens, bogs, and upland peat plateaus accounting for 83 percent of the total land cover. The remaining 17 percent of the tundra study site is composed of surface water features.

Table 3.1 Brook's (2001) land cover classes of the tundra study site.

Landcover Class	Percent of Study Area
Willow Birch Shrub Fen	0.9
Sedge Rich Fen	1.2
Sphagnum Spruce Bog	3.2
Sedge Larch Fen	3.6
Sedge Bulrush Poor Fen	6.3
Lichen Spruce Bog	14.5
Water	16.9
Lichen Peat Plateau	19.6
Lichen Melt Pond Bog	33.6
Total Landcover	99.7

It should be noted that these percentages are based on satellite data with 30m resolution. This pixel resolution is quite high when compared to the scale of spaceborne passive microwave sensors, but improved resolution data is available. A Landsat 7 ETM+ pan-sharpened mosaic (bands 7, 4, 2) of the study area with 14.25m resolution was available (GeoCover, 2000). This pan-sharpened mosaic was used to create a new high resolution lake mask of the tundra study site. The total land cover covered by surface water within the tundra study site increased to approximately 23 percent, which closely matches the 25.2 percent provided by The State of Canada's Ecosystems in Maps (2002) digital vector data. The amount of surface water visible in Quickbird imagery (2.5m – 0.6m resolution) on Google Earth™ for the tundra study site provides an indication that the total surface water land cover percentage may be even higher than 25 percent. The breakdown of the tundra study site land cover percentages is very dependent on the scale of the data used to create these numbers. Brook's (2001) land cover data contains the most detailed terrestrial land cover information for the study site and will be used for the analysis of the snow survey data, but the higher resolution Landsat 7 ETM+ lake mask created for this study will be used for the preliminary lake ice analysis. For the more detailed RADARSAT lake ice analysis an even coarser resolution lake mask will be utilized because of the 200m resolution SAR imagery, which further reduces the lake cover fraction to 14 percent.

3.2.3 Topographic relief

The tundra site chosen for this analysis has very little topographic relief. This was observed during the field studies and from 1:250,000 Canadian Digital Elevation Data (CDED) available for the region (Canadian Digital Elevation Data, 2003). The CDED consists of an ordered array of ground elevations at regularly spaced intervals (north-south x east-west - 93m x 65-35m). The CDED are based on National Topographic Data Base (NTDB) digital files at the scale of 1:250,000, according to the National Topographic System (NTS). The mean elevation above sea level for the tundra study site is 48m with a min/max range of 29m-67m. There is a very gradual change in elevation of ~1m/1km from the southern half of the study area to the northern half (moving from the inland uplands towards the lowland coastal areas). The lack of topographic variation for the tundra study site simplifies the interpretation of microwave brightness temperatures and the synthetic aperture radar sigma-nought backscatter intensity values used in this analysis.

3.3 Summary

The tundra study site is found in the Hudson Bay Coastal Plains, along the west coast of Hudson Bay. It is an environment with a cold subarctic climate covered by snow and ice for much of the year. It is one of the most southerly expanses of tundra in the world (excluding alpine areas) and is covered with lakes and ponds, mosses & lichens, low lying shrubs, and isolated tree islands and taller vegetation which grow mainly along creekbeds and lake edges. Because of its southern location and proximity to the boreal forest, the presence of trees are common, although limited in extent and small in size. There is minimal topographic relief, but due to isostatic rebound, there is a gradual slope in elevation from the inland uplands towards the low lying coastal areas. The representativeness of this location in relation to the more northern Canadian tundra may not be high, but the accessibility of this southern tundra study site for an intensive ground / air field campaign and its representation of the boreal forest / tundra transition zone were the main reasons for choosing this study site.

Chapter 4
Data Collection and Processing Methods

The objective of this thesis is to identify and explore the dominant factors that influence microwave brightness temperatures in the tundra environment and thereby drive the consistent underestimation of satellite microwave SWE retrievals

To address the issue of passive microwave SWE underestimation in the tundra, Environment Canada conducted an intensive field campaign from March 6th to 13th 2006, south of Churchill, Manitoba on the Hudson Bay Coastal Plains. A number of complementary datasets were collected, including passive microwave brightness temperature data at various resolutions from airborne and spaceborne radiometers, a full suite of coincident data on snowpack properties, and recently acquired information on land cover derived from Landsat data. In-addition, a late winter (March) regional lake ice map was created depicting different ice types using a 2005-2006 winter time series of RADARSAT-1 ScanSAR Wide imagery.

The strategy used to identify the dominant factors controlling SWE underestimation in the tundra environment was to quantify, at the satellite scale, the uncertainty associated with Environment Canada's open environment algorithm at this tundra study site. To do this the high resolution airborne microwave brightness temperatures were used to identify the sub-grid cell brightness temperature distribution that were contributing most to this underestimation; and the coincident snow survey, land cover and/or lake ice information was then used to interpret and explain the localized areas of underestimation within the satellite grid cell.

4.1 Passive microwave brightness temperature data sources

4.1.1 Spaceborne brightness temperatures

Passive microwave brightness temperatures acquired from spaceborne radiometers were measured at the various spatial resolutions and frequencies listed in Table 4.1. The Level 2A SSM/I and AMSR-E swath data were downloaded from the National Snow and Ice Data Center (NSIDC) by Environment Canada and converted to EASE-Grid format. The swath brightness temperature footprint centre locations vary between orbits and both the AMSR-E and SSM/I sensors have slightly different spatial resolutions. Therefore the EASE-Grid re-sampling routine spatially standardizes the microwave brightness temperatures to a fixed grid for easier comparison with one another. The spaceborne sensors pass over the study site twice a day with a morning (AM) and afternoon / evening (PM) overpass. The AM overpasses are more suitable for snow cover applications because during the early morning hours, the influence of solar heating with potential for snowmelt, is very low. Therefore, for this study only the AM overpasses for both AMSR-E and SSM/I were analyzed for the March 6th to March 13th 2006 study period, making available a total of 8 satellite brightness temperature measurements for each sensor for the entire study period.

Table 4.1 Spaceborne brightness temperatures measured from March 6th to March 13th 2006.

Sensor	Frequency (GHz)	Incident Angle (degrees)	Polarization	Original Swath IFOV (km)
SSM/I	19.35	53	Dual Polarization	45 x 70
	22.235			40 x 60
	37.00			30 x 38
	85.50			14 x 16
AMSR- E	6.925	54.8	Dual Polarization	43 x 75
	10.65			29 x 51
	18.70			16 x 27
	23.80			18 x 32
	36.50			8.2 x 14
	89.00			3.5 x 5.9

4.1.2 Airborne brightness temperatures

Airborne brightness temperature data were acquired from dual-polarized 6.9, 19.35, and 37 GHz microwave radiometers mounted on board the National Research Councils' (NRC) Twin Otter aircraft. Figure 4.1 illustrates the locations of the radiometers that are installed in a special baggage door located on the port-side of the aircraft and the underside of the aircraft, each with a 6º antenna, mounted in the door at a 53º incidence angle to simulate the earth-viewing characteristics of the satellite–based SSM/I passive microwave sensor (Walker et al., 2002). Also mounted in the door with the same view angle, is a surface temperature sensor and a video camera for recording the characteristics of the ground within the radiometer footprint.

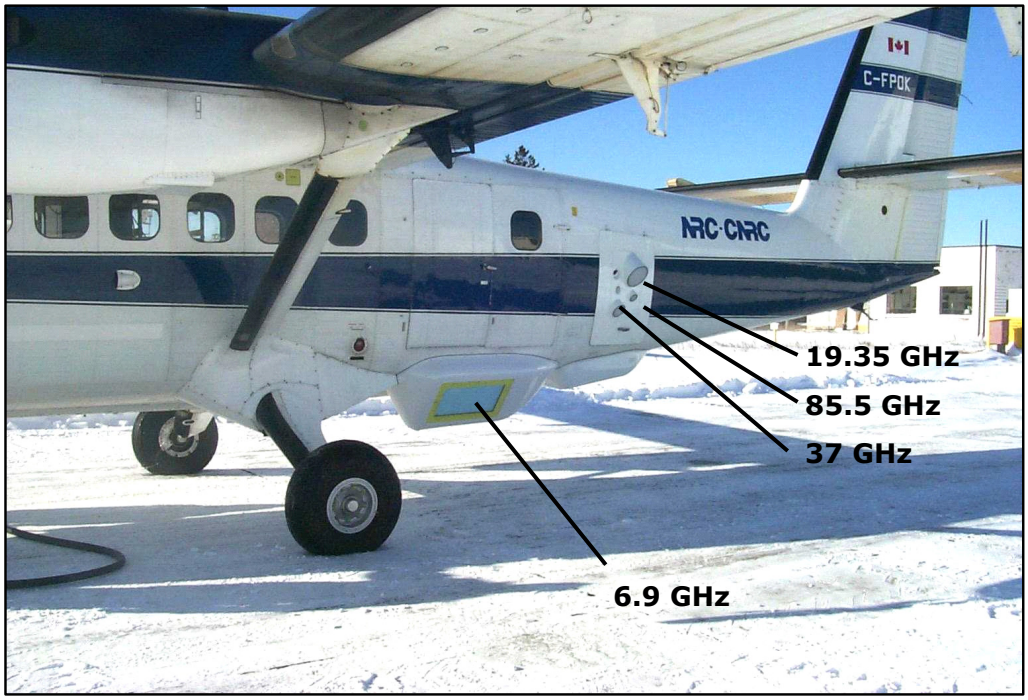

Figure 4.1 NRC Twin Otter aircraft with mounted passive microwave radiometers onboard.

Before and after each Twin Otter flight, the microwave radiometers were calibrated by measuring the brightness temperatures from targets with known radiometric properties. A two-point, hot and cold target calibration technique was performed, using a microwave absorbing material with blackbody properties (ECCOSORB) as the "hot" reference, and liquid nitrogen as the "cold" reference. Over the course of all flights involving the airborne data acquisition, the differences between the actual

measured brightness temperature values and the known values of the hot and cold reference targets are plotted out, and the difference range provides an indication of the level of uncertainty for each frequency. The uncertainty associated with each airborne frequency is provided in Table 4.2. To adjust the airborne brightness temperatures to best account for this range of uncertainty, non-linear equations were used to adjust post-flight brightness temperatures of both the hot and cold reference targets with what should have been theoretically measured given the temperature of the calibration targets and their well known emissivity. Because the equations are non-linear, an iterative process was used where coefficients were adjusted to see if the actual measured and theoretical brightness temperatures of the calibration targets more closely matched, when actual measurements matched the theoretical brightness temperatures of the calibration targets the calibration is complete and all measured airborne brightness temperatures for that flight are adjusted accordingly using the appropriate coefficients.

Table 4.2 Calibration uncertainty of airborne brightness temperatures.

Airborne Frequency	Uncertainty
6.9GHz	5-7 K
19.35GHz	1-3 K
37GHz	0.5-1 K
85.5GHz	1-2 K

Radio frequency interference (RFI) for passive microwave frequencies has been observed on a global scale (Kidd, 2006). RFI is largely due to the exploitation of the microwave region of the electromagnetic spectrum for telecommunications. Low frequency microwave frequencies are more susceptible to RFI compared to higher frequencies. This interference result in dramatic increases in brightness temperatures at the lower microwave frequencies. Fortunately, the dramatic increases in lower frequency brightness temperatures make the identification of RFI relatively simple, and these contaminated brightness temperatures can be filtered out. Because of its connection to telecommunications, RFI is largely restricted to populated areas, and RFI is non-existent at the tundra study site. However, RFI at the 6.9GHz frequency was almost non-existent at the Churchill airport and observed intermittently at the Thompson airport where grid flight calibrations occurred, and all affected brightness temperatures were removed from the dataset.

A gridded flight network of evenly spaced north-south and east-west oriented flight lines (11 in each direction) was flown over the 25km x 25km EASE-Grid cell surrounding the tundra study site to help determine the within-grid satellite scale brightness temperature variability. Data were acquired at two flying heights producing two brightness temperature datasets with approximate footprint resolutions of 70m and 500m over the EASE-Grid cell, between March 6th and March 13th 2006. Due to the scope of this study, only the 70m airborne data was analyzed. Each airborne brightness temperature dataset consists of approximately 9500 individual airborne brightness temperature measurements.

4.2 Snow survey sampling methods

In situ snow surveys were conducted to complement the collection of the airborne and satellite passive microwave data. Two slightly different approaches were used for this snow survey: "Grid Intersection" sampling and "Run & Gun" sampling, which will be explained in greater detail in sections 4.2.1 and 4.2.2. An attempt was made to evenly space the sampling to cover the full extent of the EASE-grid cell. Figure 4.2 illustrates the extent of the 25km x 25km EASE-Grid cell covered by the 22 flight lines. The Grid Intersection sampling occurred where a north-south and east-west flight line crossed paths. The Run & Gun sampling occurred along a single north-south flight line in the western half of the EASE-Grid cell. There were four snow surveyors involved with the measuring of SWE, snow depth, density and approximate snow grain size at 87 sites across the tundra study area. The snow surveyors used a helicopter to travel to the flight grid and in between snow survey sites

4.2.1 Grid Intersection sampling

The main sampling approach referred to as Grid Intersection sampling, involved conducting snow surveys at the intersecting point of a north-south and east-west flight line. A total of 22 flight lines were flown with 121 intersecting points, however due to time and budgetary constraints a total of only 60 intersecting points were surveyed. Figure 4.3 illustrates the stepped-line sampling pattern that was used at each grid intersection to assess the variability in snow properties along a flight line, in both the across-track and along-track directions. The goal of snow surveying along a transect was to sample the snow properties within the footprints of several airborne brightness temperatures along a flight line to see if changes in airborne brightness temperatures reflected changes in snow properties. At each Grid Intersection sampling site, the helicopter would arrive at the intersection point using

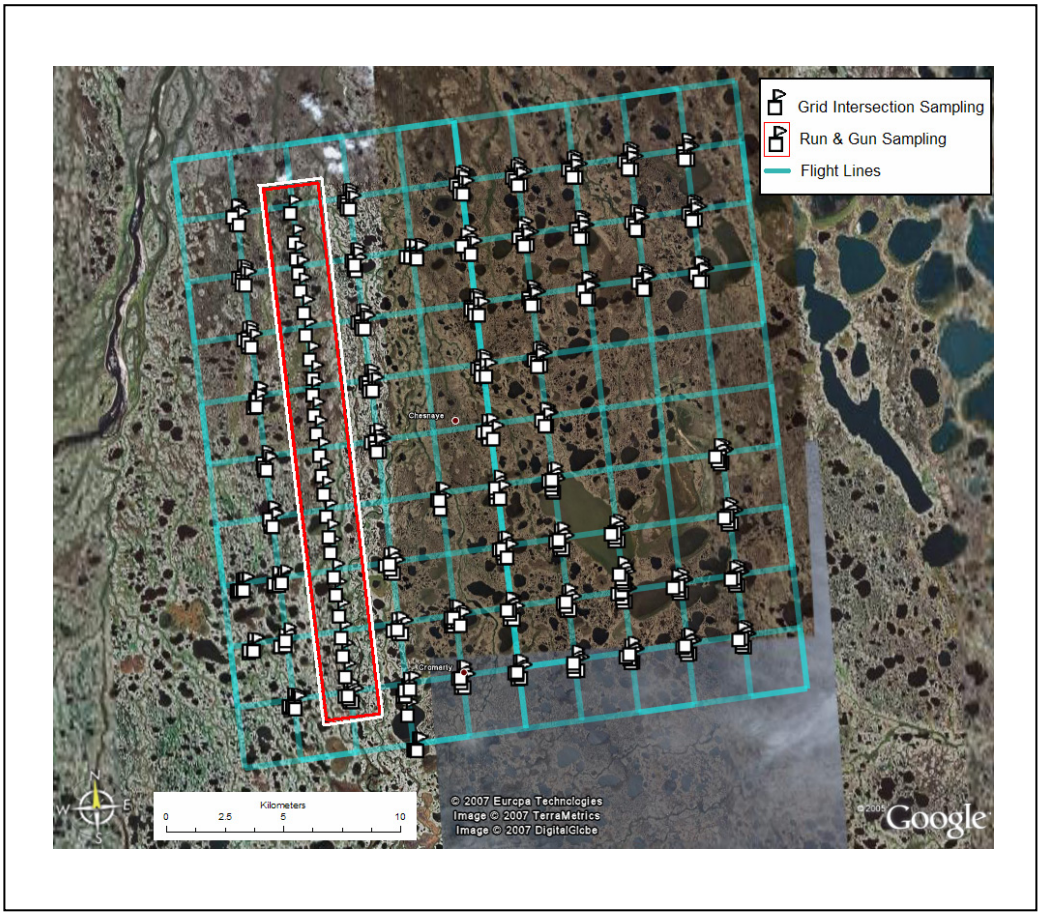

Figure 4.2 Tundra study site flight grid and snow survey locations with a Google Earth™ background image.

Global Positioning System (GPS) navigation. Once over the intersection point, the helicopter would then fly in a north-west direction for 100m-200m and land, but not shut down. The snow survey team would disembark from the helicopter with their snow sampling equipment, which included an ESC-30 snow core tube for measuring SWE and density, a number of depth probes (1 meter sections, which can be attached for deeper snow drifts), and a hand-held GPS. The helicopter would then take-off and land at the grid intersection point. As shown in Figure 4.3, the GPS was used to mark waypoints (shown by a square with a flag on top in Figure 4.3) at the beginning of the snow survey line (Waypoint 173), at all turns in the line (Waypoints 174 and 176), at the snow pit (Waypoint 175), and at the end of the snow survey line (Waypoint 177). It would also record a GPS track log of the

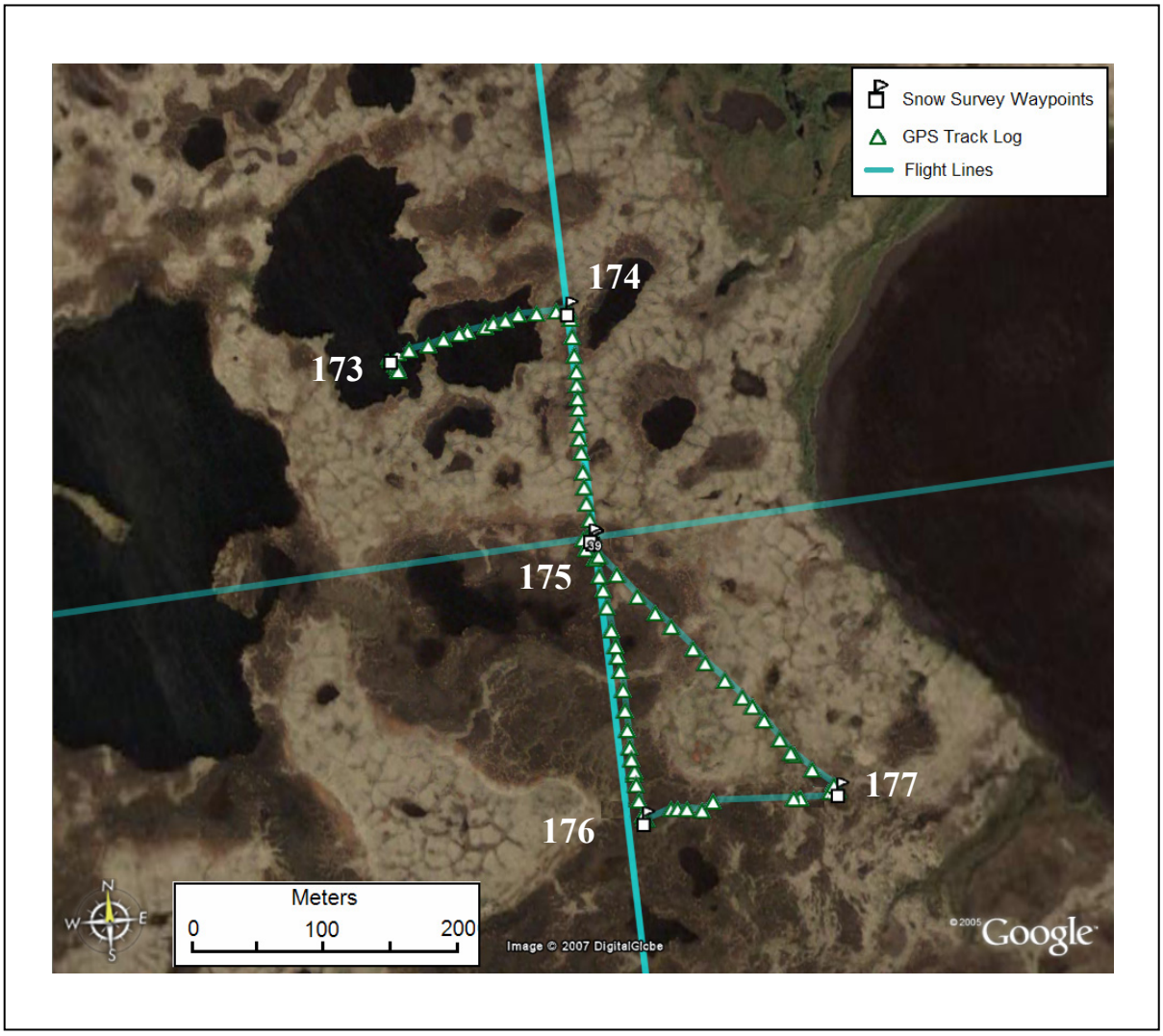

Figure 4.3 An example of the stepped-line sampling pattern used at each Grid Intersection sample site. The GPS track log (triangles) indicates the path taken by the snow survey team and the large whit numbers are the locations of the waypoints marked at this site. High resolution (2.5m) Quickbird imagery is used as the background image and highlights the high concentration of ponds and wedges of the polygonal tundra (black = water, grey brown = tundra).

route walked by the snow surveyors with an accuracy that was typically +/- 5m to 10m (route shown by the triangles in Figure 4.3). As the snow surveyors traveled in a stepped-line pattern across the Grid Intersection, SWE core and depth measurements were recorded at regular intervals along the track log route with depths being recorded every 10m to 15m and SWE being recorded every 40m to 50m. The relative location of each depth and SWE measurement (between which waypoints) along with a site description for each measurement (a note indicating whether the SWE or depth

measurement was recorded on land or ice and if any type of vegetation was present) was recorded into log books. A typical Grid Intersection site would result in anywhere from 10-25 SWE core measurements and 40-70 depth measurements. At each Grid Intersection site, the snow surveyors would dig a snow pit at the point where the flight lines actually intersected. In the snow pit, snow stratigraphy and approximate grain size were recorded for each snowpack layer. Each Grid Intersection site would typically take about one hour to sample.

4.2.2 Run & Gun sampling

The second approach referred to as Run & Gun sampling was named because of its much quicker sampling technique. The idea behind this technique was to pick a single north-south oriented flight line and attempt to sample in the along-track direction of that flight line at a higher frequency, instead of just at the grid intersections. To increase the number of sites sampled using this technique the amount of time taken was significantly reduced. Typically at each Run & Gun site five SWE core measurements, and 30-40 depth measurements were recorded at a point location (usually 25m-30m radius) and then the snow surveyors moved on to the next site. Similar to the Grid Intersection sampling, a site description for each measurement (measured on land or ice, type of vegetation present, if any) was recorded into the log books at these sites. This whole process would take approximately 10 minutes for each site including transit between sites.

4.2.3 Snow survey classification

Every SWE core and depth measurement was classed into one of seven land cover categories based on the site descriptions recorded in the field, and with the help of site photos and high resolution Quickbird satellite imagery available on Google Earth™. The site classes were decided on prior to gaining any access to the Brook (2001) land cover data. These seven classes are subjective and were strictly based on field observations of what seemed to be the major land cover categories within the tundra study site that might influence snow properties. Table 4.3 illustrates the number-key and description of each category developed to simplify the process of recording site descriptions for each SWE and depth measurement. Photographs of each of the seven snow survey classes are illustrated in Figure 4.4. The polygonal tundra and tundra ponds are combined in one photo. The seven categories of land cover identified in the snow survey classification for this study were compared to Brook's (2001) detailed land cover classification discussed in Section 3.2.2. This was done to assess the percent of the tundra

study site devoted to each of the seven snow survey classes. Brook's (2001) detailed land cover category descriptions and pictures were used to identify which of the seven snow survey categories matched Brook's nine land cover categories found within this study area. The seven snow survey classes had to be condensed into five less specific classes to better match Brook's (2001) descriptions. Table 4.4 shows the land cover percentage for the combined five snow survey classes identified within the tundra study site.

Table 4.3 The land cover categories recorded for each SWE and depth measurement used in the snow survey classification.

#	Description
1.1	Ponds and Flooded Land
1.2	Lakes
2.1	Polygonal Tundra
2.2	Shrub Tundra
2.3	Willow Bushes
2.4	Tree Islands
2.5	Creekbed - Larger Trees/Bushes

Table 4.4 Assessing the proportion of the tundra study site devoted to each of the seven snow survey classes using Brook's (2001) land cover of the Cape Churchill Wildlife Management Area.

Seven Snow Survey Classes	Brooks (2001) Classes	Percent of Study Area
Ponds and Flooded Land Polygonal Tundra Shrub Tundra	Lichen Peat Plateau Lichen Melt Pond Bog	53%
Lakes	Water	17%
Willow Bushes	Willow Birch Shrub Fen Sedge Rich Fen Sedge Bulrush Poor Fen	8%
Tree Islands	Sedge Larch Fen	4%
Creekbed - Larger Trees/Bushes	Sphagnum Spruce Bog Lichen Spruce Bog	18%

Figure 4.4 Photographs of each of the seven snow survey classes with the polygonal tundra and tundra pond classes combined into one photo as both land covers were identified within this photo.

4.3 Creating a high resolution lake mask

Brook's (2001) land cover map indicated that 17 percent of the tundra study site was covered by water. Based on the high resolution Quickbird satellite imagery of the study site available on Google Earth™, this percentage was thought to be too low. The importance of exploring the influence of all sized water bodies on the microwave brightness temperatures was desired and an improved resolution lake mask was created. Due to budget constraints, the high resolution Quickbird data was not purchased and instead a new high resolution lake mask was created from a Landsat 7 ETM+ pan-sharpened mosaic resampled to 14.25m pixel resolution (GeoCover™, 2000). This mosaic is a false colour composite of bands 7 (mid-infrared), 4 (near-infrared), and 2 (green). The lake mask was created using a similar technique as applied by Kloiber et al. (2002). A K-means unsupervised classification was conducted, with 10 clusters specified and a change threshold of 5% or a maximum of 10 iterations. Because water features have very different spectral characteristics compared to terrestrial features, especially in the near-infrared band, water is put into distinct cluster classes. The 10 output clusters were then aggregated into a binary land and water classification map using high resolution Google Earth™ and the original Landsat imagery as reference sources. Further post-classification processing was done using a majority / minority analysis. This analysis changes spurious pixels within a large single class to that class (majority analysis). A minimum kernel size of 3x3 was entered and the center pixel in the kernel was replaced with the class value that the majority of the pixels in the kernel had. The same kernel size was used for both land and lake classes to remove spurious water pixels from the land class and to remove the spurious land pixels from the water class. The majority / minority analysis helped to filter out the smaller spurious water and land pixels that had the greatest potential for being misclassified, improving the overall accuracy. However, another potential source of error using this unsupervised classification technique is the misclassification of a fen or bog that has a high moisture content as a lake feature, which introduces some potential errors in the interpretation of the passive microwave airborne data and the SAR winter time series because of the similarities of a frozen fen or bog to a terrestrial land surface.

Using the high resolution lake mask, the total tundra study site land cover percentage devoted to surface water increased to approximately 23 percent compared to Brook's (2001) 17 percent. The higher percentage more closely matches the 25.2 percent provided by The State of Canada's Ecosystems in Maps (2002) digital vector data. The improved resolution lake mask was very useful for analyzing the airborne brightness temperatures, but was unnecessarily detailed for use with the

synthetic aperture radar (SAR) winter time series of lake ice information because of the 200m resolution of the SAR imagery.

4.4 Create a regional tundra lake ice map from a SAR time series

This study exploits the established concept of using a SAR winter time series for identifying which shallow tundra lakes are frozen to bottom and which have free floating ice. Once the time series was created, a number of lakes were analyzed from within and around the tundra study site and the backscatter intensity was plotted versus time. Three unique backscatter intensity patterns were identified. These backscatter intensity patterns very closely matched the patterns identified in previous studies (Jeffries et al, 1994, Morris et al., 1995, and Duguay et al., 2002), and therefore similar lake ice characteristics were assumed to be associated with these backscatter intensity patterns. Using these select few lakes for validation and as training sites, a principal component analysis was applied to the SAR time series and a supervised classification was conducted on the principal component analysis outputs to create a regional tundra lake ice map identifying lakes most likely frozen to bottom or not within and around the tundra study site. All SAR data used in this analysis was RADARSAT-1 ScanSAR Wide-A imagery provided by the Canadian Ice Services (CIS) for the 2005-2006 winter season.

4.4.1 Choosing appropriate RADARSAT images for the winter time series

The CIS is interested in monitoring changing sea ice conditions in Hudson Bay and therefore the majority of images available for this time series were acquired during the earlier part of the winter season during the dynamic stages of ice growth, and only single images were acquired during the more stable winter months when Hudson Bay was relatively unchanging and completely frozen over. Table 4.5 lists the number RADARSAT images available in the CIS archive for the study time period. When conducting an analysis of a time series of SAR images to ascertain how a particular image feature changes over time, it is important to ensure that each image in the time series is as geometrically and radiometrically similar as possible. This ensures that if a change in backscatter intensity is detected over time, this difference can be attributed to a change in the feature of interest, not in how the data were measured. The Canadian Data Processing Facility (CDPF) calibrates the

Table 4.5 Number of RADARSAT images available in the Canadian Ice Service archive for the study site during the 2005-2006 winter season.

Month	Number of Images
September	0
October	6
November	11
December	13
January	1
February	1
March	1

ScanSAR Wide data products used in this analysis to provide both geometric and radiometric corrections to the image data (RADARSAT International, 2000). However, RADARSAT-1 uses a sun-synchronous orbit with descending and ascending passes and therefore has different "look" directions for each orbit, west-looking for a descending pass, and east-looking for an ascending pass (RADARSAT International, 1999). Therefore to further reduce geometric distortion between image dates all of the available images were scrutinized for similar orbit passes and that the study area fell within the same approximate image location. Four final dates were chosen that most closely matched. The December 23rd ~2341hr 2005 image and the March 29th ~2345hr 2006 image matched almost exactly, while the Nov 19th ~2336hr 2005 and January 30th ~2345hr 2006 images matched almost exactly. The two pairs of images were both ascending orbits, but the study sites were located in slightly different image locations, possibly introducing small geometric and radiometric error into this analysis.

4.4.2 Processing of the raw CEOS RADARSAT images to create a winter time series

The raw CEOS RADARSAT images were acquired from the CIS archive. The CIS in Ottawa receives this data in almost near real-time from the CDPF in Gatineau, Quebec. Each RADARSAT CEOS file is automatically resampled on arrival at the CIS to reduce storage space prior to archiving (Bertoia and Ramsay, 1998). A 2x2 block averaging is applied to the original ScanSAR Wide image. This averaging reduces the SAR image resolution from 100m to 200m and consequently reduces the presence of speckle noise reducing the need to apply any additional SAR filters. The CIS also alters

each data filename before archiving and does not archive the *.nvol or *.vol files that accompany all raw CEOS files from the CDPF. Therefore to import the CIS archived data into PCI Geomatica 10.0 for processing it was necessary to rename the files to the standard CEOS file naming convention (DAT_01.00n, LEA_01.00n, TRA_01.00n), and to use a "dummy" *.vol file (VDF_01.00n). PCI uses the *.vol file simply for image date information and does not use the *.nvol file.

Once the four images chosen for the winter time series had been renamed and imported into PCI, steps were taken to convert digital numbers in the images to the normalized radar backscatter intensity values, or sigma nought (σ°). Converting the radar data into backscatter intensity values is desirable because it quantifies measurements relative to the ground surface and is not a property of the measurement geometry or imaging footprint (Woodhouse, 2006). Sigma nought values or backscatter intensity are measured in decibels (dB) representing a measure of the scattering cross-section (amount of energy that arrives back at the radar system after interacting with the surface) per unit area of surface (Woodhouse, 2006). However, to accurately measure backscatter intensity it is necessary to know the precise amount of ground surface area with which the radar system is interacting. The amount of surface area can vary substantially with variations in topography. Thus, without topographic information accurate backscatter intensity values cannot be calculated. The tundra site chosen for this analysis has very little topographic relief. The 1:250,000 CDED already discussed in section 3.2.3 was found to have an approximate change in elevation of 1m/1km from the southern half of the study area to the northern half with a range in elevation of only 38m across the entire 625km^2 tundra study site. This lack of vertical relief made it possible to disregard the need for accurate topographic information to calculate backscatter intensity values. No topographic data were used to calculate the backscatter intensity values for the tundra study site, other than entering the mean elevation above sea level.

In order to georeference the RADARSAT images, the PCI software makes use of the orbit ephemeris data which is embedded in the raw CEOS data files. However, the positional accuracy of these data were off by several hundred meters for the tundra study site. Additional georeferencing was necessary to align the SAR data with existing data sources to ensure that the multiple image dates were aligned correctly for layer stacking to create a single multi-layered time series image. Because the RADARSAT imagery were already partially georeferenced, only a small number of ground control points (GCPs) were needed to more accurately georeference the different image dates (Table 4.6).

Table 4.6 Number of ground control points (GCPs) used to georeference each image and the resulting root mean square (RMS) error.

SAR Image Dates	Number of GCPs	RMS Error (pixels)
November 19th 2005	7	0.26
December 23rd 2005	7	0.53
January 30th 2006	8	0.41
March 29th 2006	7	0.36

The Landsat 7 ETM+ mosaic was used as the geocoded image to reference the RADARSAT images. It can be a challenge to accurately georeference a coarse resolution image such as the ScanSAR Wide because of the inability to identifying distinct surface features. Most of the GCPs were lake or coastal features, but these were also a challenge to use because of difficulty in distinguishing the lake and coastal margins due to the formation of ice. Therefore, despite the RMS errors being limited to under half a pixel (~50m), it is likely that the error could potentially be upwards of a full pixel or greater (100m-200m) in some locations. The locations of the GCP were recorded largely around the study area, and not necessarily across the entire image swath because after the georeferencing had taken place an image subset was taken. The image subset was based on the extent of the high resolution lake mask created for the tundra study site. Once all of the GCPs had been collected, a first order polynomial transformation was used with a nearest neighbour re-sampling method and a sampling interval of 1 to preserve the original backscatter intensity values (dB). Layer stacking was then used to create a four band, November 19th, December 23rd, January 30th, March 29th SAR time series image of the tundra study site.

4.4.3 Defining RADARSAT backscatter intensity plots to identify different lake ice types

Jeffries et al. (1994), Morris et al. (1995), and Duguay et al. (2002), used a winter time series of SAR images to define plots of backscatter intensity (dB) as a function of time for shallow tundra lakes. The dB values in these plots showed substantial variation in backscatter intensity over the course of the winter. During early winter, right after freeze-up, the backscatter values were at their lowest. Then as the season progressed the backscatter values climbed steadily and reached a winter maximum between January and March. With the onset of the spring melt the backscatter values dropped back to

pre-winter conditions. At any time during the winter season the backscatter could drop significantly and when this occurred, field observations confirmed that the tundra lake had frozen to bottom.

Using the work of Jeffries et al. (1994), Morris et al. (1995), and Duguay et al. (2002) as examples, 14 lakes were analyzed (Figure 4.5) and the backscatter values were plotted over time. 4 lakes were identified as unchanging ice types because they appeared dark in each date of the SAR image time series with one of these unchanging lakes found outside the extent of the flight grid. The longer wavelength 6.9 GHz frequency of the airborne brightness temperatures was used to help identify 4 lakes that were likely frozen to bottom, and 4 that likely had free-floating ice. Hall et al. (1981) documented that lakes with liquid water below the ice affect longer wavelength microwave radiation by substantially lowering the brightness temperatures compared to adjacent land due to the lower emissivity of the water below the ice. Therefore, using a dramatic decrease in the 6.9GHz brightness temperatures compared to the surrounding land surface as an indication that a lake likely has liquid water below the surface, 4 lakes were chosen to be analyzed that appeared to have free-floating lake ice. And like-wise, if the 6.9GHz frequency showed no apparent difference in brightness temperatures over a lake compared to the adjacent land, then this was an indication that lakes were frozen to bottom, and 4 more lakes with this type were identified. An additional 2 lakes were chosen outside the extent of the airborne data with one lake likely frozen to bottom, and another lake likely to be free-floating based on a visual interpretation of the SAR backscatter values in the time series. For most lakes, the average backscatter value of between 10 and 6 RADARSAT pixels was recorded for each of the four image dates in the time series. For the lakes with the matching airborne data, the pixels were chosen to match along the same transect as the airborne measurements. For the 3 lakes outside the airborne data extent, a cluster of pixels was chosen. The average backscatter value for each of the 14 lakes in each image date was then plotted out to produce the backscatter intensity plots that were visually compared to those defined in the previous SAR studies already mentioned. Those lakes that matched the backscatter intensity patterns of the previous studies were used to create backscatter intensity summary plots for the tundra study site. The backscatter intensity summary plots characterized the average backscatter return for each image date for each of the three ice types identified: free floating ice, frozen to ground ice (mid winter), unchanging ice (early season frozen to ground or bubble free ice). Those lakes that had backscatter intensity patterns that matched the summary plots were used for to validate the principal component outputs and as training sites for the supervised classification used to create the regional tundra lake ice map.

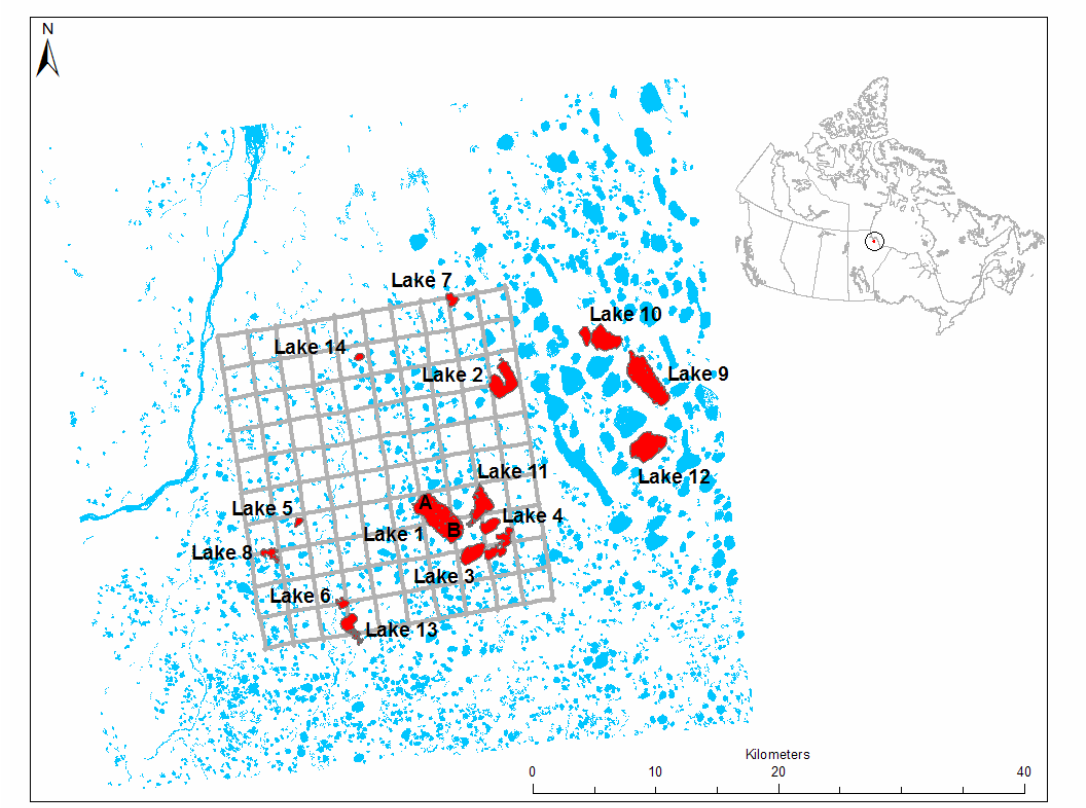

Figure 4.5 A map of the lakes used to develop the lake ice training sites are provided and the flight grid is shown as a reference. The training site lakes are highlighted a darker colour (red) and labeled.

4.4.4 Conducting a principal component analysis on the SAR winter time series

Principal component analysis (PCA) is a powerful method for analyzing correlated multitemporal and multidimensional data. When conducting change detection for a particular area it is the portions of the image dataset which show an absence of correlation which are of interest because they represent areas of change (Byrne et al., 1980). A PCA is a technique that can highlight these uncorrelated parts of the image by transforming the original remotely sensed data into a smaller and easier to interpret set of uncorrelated principal components (Jensen, 2005).

A principal component analysis was conducted on the four-date winter time series image created in section 4.4.2. The analysis was limited strictly to lake features using an even further filtered version of the lake mask created in section 4.3. Lakes smaller than 200m x 200m were filtered out because the coarse resolution (100m pixels) of the RADARSAT ScanSAR Wide data used in this analysis

cannot capture such small lake features. The coarse resolution lake mask would also reduce land / water mixed pixels which would introduce more errors into the PCA change detection and subsequent supervised classification used to produce the regional tundra lake ice map.

The principal component analysis tool available in ENVI 4.2 was utilized for this analysis. The principal component analysis in this software uses a linear transformation of the multitemporal SAR time series to translate and rotate the data into a new coordinate system to maximize the variance of the data about the new axis. This was done by finding a new set of orthogonal axes that have their origin at the data mean and that were forward rotated so the data variance was maximized. The principal component was based on the covariance matrix of the winter time series of images. The eigenvalues (λ) define the amount of variance explained by each PC, and are commonly expressed as a percentage of the total variance by dividing each individual eigenvalue by the sum of all calculated eigenvalues. Eigenvectors (a) are intermediate values which define the relationship between the original data and each PC. The output principal component images were used as input images for a supervised classification.

4.4.5 Conducting a supervised classification to create a regional tundra lake ice map

Using the backscatter intensity plots defined in section 4.4.3, and the principal component outputs created in section 4.4.4, a number of training sites were identified in the four principal component output images. These training sites identified lakes that most likely were frozen to bottom, were most likely free-floating ice, or had changed little over the course of the winter season. A minimum distance supervised classification was conducted on the first three PC output images (PC 1, PC 2, PC 3). The classification was limited strictly to lake features using the lake mask created in step 4.3. A schematic diagram of the steps involved with from taking the individual SAR images to creating a regional tundra lake ice map is provided in Figure 4.6.

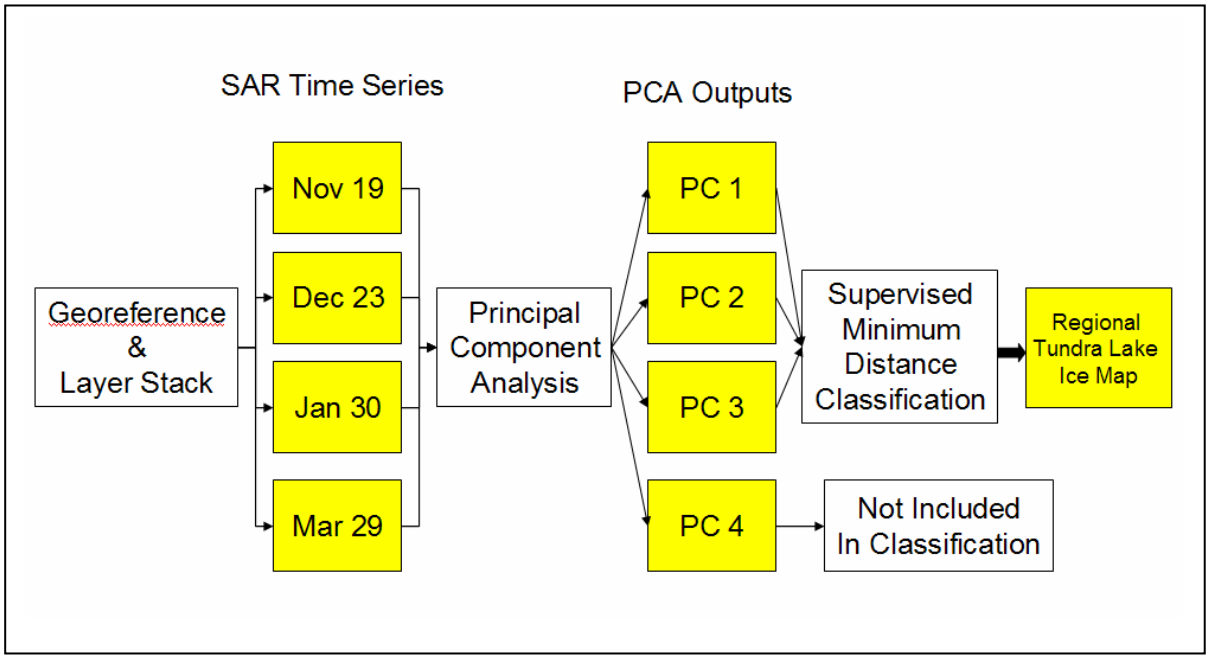

Figure 4.6 A schematic diagram illustrating the steps taken to create a regional tundra lake ice map for this study; starting from the georeferencing and layer stacking of the original SAR imagery, followed by the principal component analysis and the supervised minimum distance classification on the PC outputs to produce the lake ice map.

4.5 Summary

A wide range of data were collected and processed to support this study. These data are typical of most research investigating the use of passive microwave remote sensors to estimate SWE and include spaceborne and airborne microwave brightness temperatures, measured SWE, snow depth, density, stratigraphy and grain size information, along with high resolution Landsat ETM+ imagery. Atypical of this research, is the integration of RADARSAT-1 ScanSAR Wide imagery into this analysis to assist in the interpretation of the microwave brightness temperatures, by providing information on lake ice properties. This has not been done before and is an exciting new direction for this area of research. Furthermore, what is also unique about this study is the precise integration of all of the snow survey and remote sensing information using GPS data and Geographic Information Systems (GIS) providing a level of data integration accuracy to this study not typically seen in passive microwave SWE retrieval research.

Chapter 5
Snow Survey and Brightness Temperature Analysis Results

5.1 Summary of tundra study site snow properties

In situ snow surveys were conducted to complement the collection of the airborne and satellite passive microwave data. Snow surveys were conducted at 87 sites across the tundra study area measuring snow depth, SWE, snow density, snow grain size and snow stratigraphy. The tundra study site averages and standard deviations for all measured snow variables are provided in Table 5.1. The snowpack examined within the study area typically had an average grain size of 2.5mm with approximately 4 distinct stratigraphic layers of wind slab and depth hoar. The average measured depth was 31cm, with a density of 0.303 g/cm^3, and a snow water equivalent of 95mm. The standard deviations for the depths and SWE are very large due to the heterogeneous nature of the snow-trapping micro-topographic relief and taller vegetation found within the study site.

Table 5.1 Summary of snow survey measurements for the entire tundra study site

Measurement Type	Unit of Measurement	Measuring Instrument	Number of Recorded Measurements	Arithmetic Mean	Standard Deviation
Depth	cm	depth probe - 1m sections	4246	31	26
SWE	mm	ESC-30 sampler	1120	95	72
Density	g/cm^3	ESC-30 sampler	1120	0.303	0.077
Snow Grain Size	mm	snow pit card	54	2.5	1.1
Snow Stratigraphy	number of layers	observation	54	4.4	1.5

To further increase the sample size of the SWE measurements, all ESC-30 SWE measurements (n=1120) were combined with estimated SWE measurements (n=4246) for a total 5366 SWE measurements. The estimated SWE was calculated for all 87 snow survey sites visited within the grid. All depths recorded at each site were multiplied by the average snow density measured with the ESC-30 sampler at that site to produce an estimated SWE value. To test the validity of using estimated SWE measurements, a linear regression was conducted between the mean SWE ESC-30 measured at all sites with the mean estimated SWE calculated for all sites (Figure 5.1), excluding two sites with unusually high ESC-30 SWE measurements. The relationship between these two variables is statistically

significant at 99%, with the regression model explaining a high percentage of variation in SWE (R^2 = 82.5%). Therefore, combining these two datasets to produce a larger, more rigorous SWE sample size appears warranted. In addition, all snow depths recorded with the ESC-30 sampler were also combined with the depths recorded with the snow probes to further increase the depth sample size for a

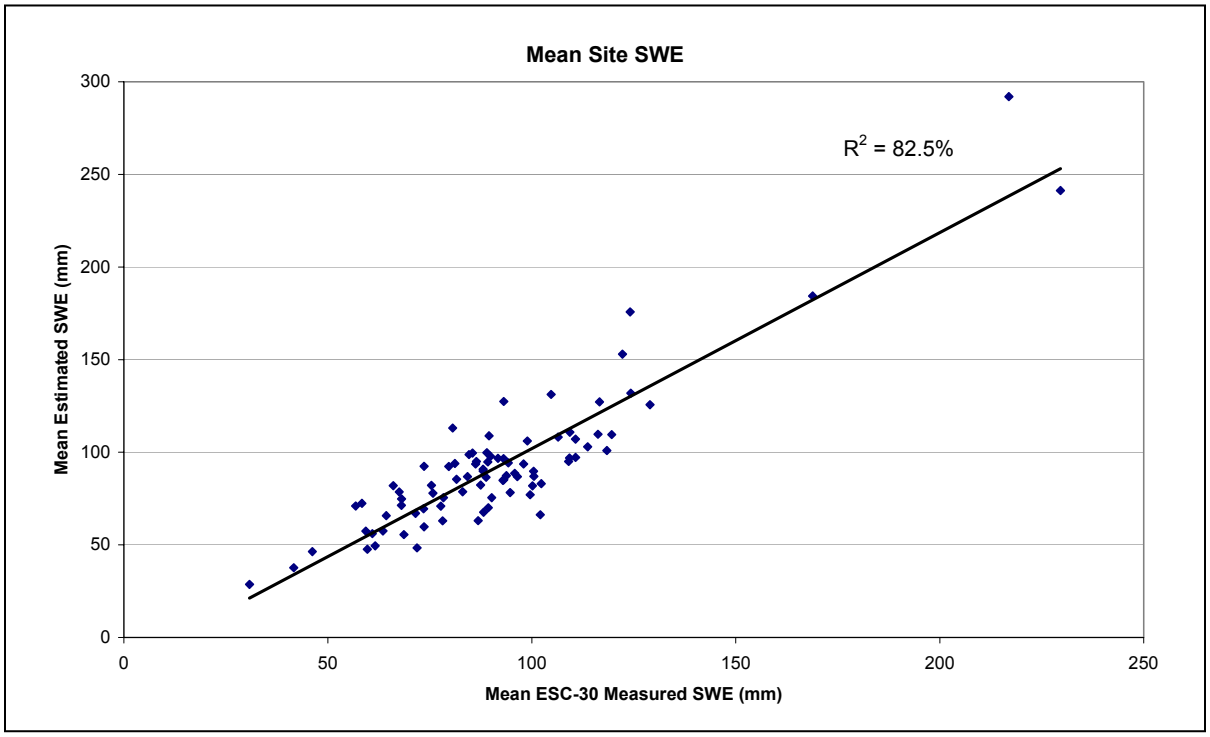

Figure 5.1 Relationship between the mean ESC-30 measured SWE and mean estimated SWE for 85 snow survey sites visited within the tundra study area. Solid line shows the linear best fit.

total of 5366 depth measurements. The larger sample sizes for all depth and SWE measurements do not make a dramatic difference in the mean measurement values or standard deviations when looking at the entire tundra study site (Table 5.2). However, when the snow properties are broken down into separate land cover classes, combining the measured and estimated SWE datasets helped reduce a bias in the distributions of the measured SWE dataset. This bias is a common problem when measuring SWE at non-staked snow course sites, as was the case for this study. When using the ESC-30 sampler for this study, the snow surveyors did not record trace SWE amounts or values of zero SWE, but the surveyors measuring snow depths did. Therefore, combining these datasets results in a more representative sample of low SWE values, thereby reducing sampling bias.

Table 5.2 Comparison of tundra study site summary statistics between the original SWE and snow depth sample size versus the larger combined sample sizes.

Measurement Type	Unit of Measurement	Number of Recorded Measurements	Arithmetic Mean	Standard Deviation
ESC-30 SWE	mm	1120	95	72
Estimated SWE	mm	4246	93	79
ESC-30 SWE and Estimated SWE	mm	5366	93	77
Depth Probe	cm	4246	31	26
ESC-30 Depths	cm	1120	32	22
Depth Probe and ESC-30 Depths	cm	5366	31	25

5.2 Summary of land cover specific snow properties

Every SWE core and depth measurement was classed into one of seven land cover categories as described in section 4.2.3. Noticeable differences in snow depths and SWE between some land covers, but not all, were discovered. The most notable differences were between land cover classes with and without tall vegetation (open tundra vs. willow bushes, tree islands and forested creekbeds). Figure 5.2 illustrates the boxplot distributions of all snow depth, SWE and snow density measurements for all seven snow survey land cover classes. The length of the boxes represents the interquartile range, there is a line drawn horizontally across the boxes at the sample median and the whiskers sprouting from the two ends of the boxes extend until they reach the sample minimum and maximum. The boxplots reveal that the seven land cover categories chosen to represent the different classes of snow in the tundra study site were unnecessarily specific. Instead, the tundra snow characteristics are divided by black vertical lines in Figure 5.2a and Figure 5.2b that separate the snow depths and SWE measurements into two broad categories: 1) short low lying vegetation typically less than 1m in height, including lakes (lightly shaded boxplots - yellow) and 2) taller vegetation typically greater than 1m in height (darker boxplots - green). This natural separation is made obvious by the similarities in sample distributions and medians for the specific land cover categories within these two groupings of vegetation height. The land covers with vegetation less than 1m in height, consistently have 2 – 3.5 times lower magnitude mean snow depths and SWE compared to the land cover with taller vegetation. Table 5.3 summarizes the snow survey mean, median, standard deviation and range of values for each snow survey class presented in Figure 5.2.

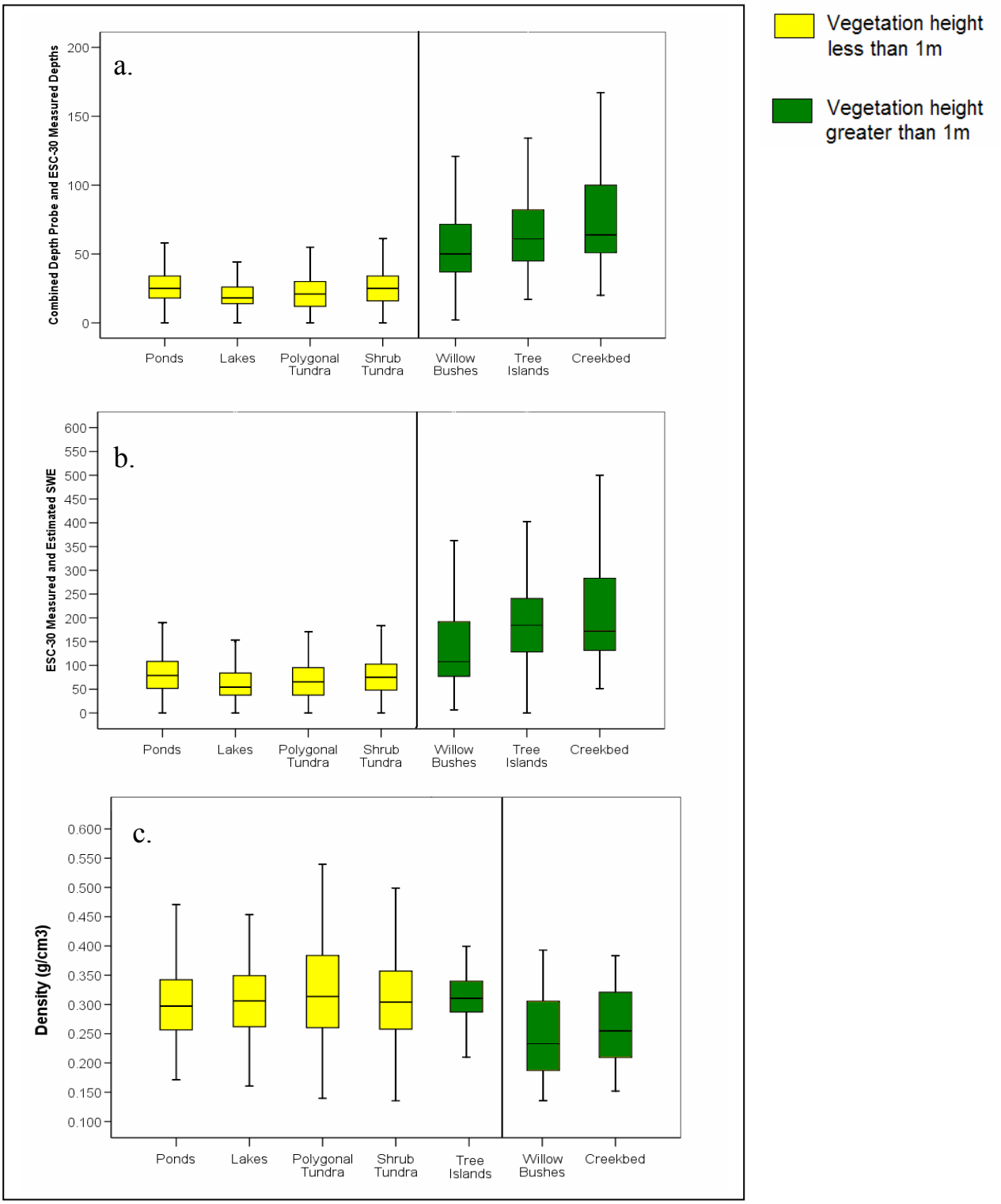

Figure 5.2 Boxplot distributions of a.) snow depths, b.) SWE, and c.) snow density for the seven snow survey classes found within the tundra study site. The lightly shaded (yellow) boxplots represent the short/non vegetated land covers with a vegetation height not exceeding 1m, including lakes. The dark shaded (green) boxplots represent the taller vegetated land covers, with a vegetation height greater than 1m. There is a black vertical line in each graph that separates the SWE, snow depth and density into two broad categories.

Table 5.3 The mean, median, standard deviation and range of SWE, snow depth and snow density for all seven snow survey classification classes.

#	Description	Measurement	Mean	Median	Standard Deviation	Range
1.1	Ponds and Flooded Land	SWE (mm)	85	79	45	445
		Snow Depth (cm)	27	25	13	145
		Snow Density (g/cm^3)	0.304	0.297	0.070	0.342
1.2	Lakes	SWE (mm)	76	54	73	637
		Snow Depth (cm)	25	18	23	200
		Snow Density (g/cm^3)	0.311	0.305	0.067	0.353
2.1	Polygonal Tundra	SWE (mm)	69	65	43	352
		Snow Depth (cm)	22	21	13	105
		Snow Density (g/cm^3)	0.326	0.314	0.089	0.516
2.2	Shrub Tundra	SWE (mm)	79	75	47	564
		Snow Depth (cm)	26	25	15	156
		Snow Density (g/cm^3)	0.312	0.304	0.077	0.425
2.3	Willow Bushes	SWE (mm)	152	108	115	630
		Snow Depth (cm)	60	50	35	198
		Snow Density (g/cm^3)	0.247	0.234	0.069	0.258
2.4	Tree Islands	SWE (mm)	210	184	121	631
		Snow Depth (cm)	70	61	38	193
		Snow Density (g/cm^3)	0.310	0.309	0.052	0.268
2.5	Creekbed - Larger Trees/Bushes	SWE (mm)	218	172	125	629
		Snow Depth (cm)	77	64	38	180
		Snow Density (g/cm^3)	0.261	0.255	0.061	0.231

More snow is present in the taller vegetation land covers because of the interactions between the taller vegetation and wind transported snow. After a snowfall event, the taller vegetation prevents the wind from redistributing freshly fallen snow; whereas, snow on the exposed open tundra is not sheltered and is easily redistributed by the wind leaving a more windswept shallower snowpack. Wind transported snow is re-distributed into wind breaks such as micro-topographic depressions (hummocky terrain and sunken tundra ponds), isolated tree islands, tall willow bushes and into forested creekbeds, which break up the wind flow. Behind these wind breaks the wind speed decreases in velocity and becomes turbulent, losing its snow transport capacity.

The snow densities illustrated in Figure 5.2c show that the natural separation of snow properties into categories based strictly on vegetation height is not universal. The snow density of the tree island land cover category has a median value more similar to the classes with a vegetation height of less than 1m and therefore the black vertical line pushes the tree island class into the class of short/non vegetated land covers. The willow bushes and creekbed vegetation categories have lower snow densities, and the shorter vegetation have higher wind induced densities. The explanation for the snow density

dissimilarity of the tree island class with the other taller vegetation classes is due to wind exposure. The isolated tree islands are typically found in the exposed open tundra or along the creekbed margins where the wind speeds are still near their maximum, inducing increased snow densities. However, the wind still decelerates on contact with the tree islands, explaining the higher magnitude of snow deposition compared to the surrounding open tundra. The snow found in the tree island category is largely exposed to the same wind forces as the land cover categories without taller, higher density wind-sheltering vegetation and thus have similar mean and median snow densities.

The tundra snow distribution and snow properties of this study site are largely dictated by the forces of the wind, however, the presence of taller vegetation can influence the wind, and subsequently have a bearing on both the snow properties and distribution. Establishing snow properties based on two broad land cover categories provides a simple means of estimating the true satellite-scale SWE for this area by allowing for the calculation of an areal-weighted landscape scale SWE average using Brook's (2001) regional land cover map.

5.3 Land cover areal-weighted tundra study site SWE

In section 4.2.3 the original seven categories of land cover identified in the snow survey classification were compared to Brook's (2001) detailed land cover map for this region to assess the proportion of the tundra study site devoted to each snow survey class with the results shown in Table 4.4. However, the snow survey summary statistics discussed in section 5.2 suggest that the original seven snow survey classes can be grouped into two broader land cover categories based on similar snow properties and land cover characteristics. These two broad categories can be distinguished by their difference in vegetation height (short vs. tall). The two broad categories of land cover have notably different mean SWE values and account for considerably different proportions of the total tundra study site. Table 5.4 summarizes the differences in SWE characteristics and land cover percentages between these two different vegetation classes and provides a representative areal-weighted SWE average for the entire tundra study site. The tall vegetation class accounts for only 30 percent of the total study area land cover, but it typically contains 2 – 3.5 times the magnitude of SWE compared to the more open short/non vegetated portion of the study area. When the areal-weighted SWE averages are calculated the contributions of SWE to the entire study site from both the short and tall vegetation classes are virtually equal despite the difference in their land cover proportions. These results indicate that half of the tundra study site SWE is stored in

Table 5.4 Landscape scale snow properties within the tundra study site.

Vegetation Type	Landcover Class	Landcover Percentage	Mean SWE (mm)	Mean SWE (mm)	Areal-Weighted Mean SWE (mm)
Short Vegetation (< ~1m)	Polygonal Tundra	70%	69	78	55
	Shrub Tundra		79		
	Tundra Ponds		85		
	Lakes		76		
Tall Vegetation (> ~1m)	Willow Bushes	30%	152	185	56
	Tree Islands		210		
	Creekbeds		218		
		Total Study Site SWE		**93**	**111**

70 percent of the study area, while the other half is stored in the remaining 30 percent of the study area. In theory, at the satellite scale, 70 percent of the study site with less SWE (short vegetation), contributes more to the spaceborne imaging footprint microwave emission than the smaller 30 percent of the study site with more SWE (tall vegetation); strictly based on the larger proportion of microwave emitting surface area of the short vegetation land cover within the satellite's IFOV. This uneven contribution of microwave emission is likely a factor in the spaceborne passive microwave underestimation of SWE in the boreal forest / tundra transition zone where there is a higher concentration of taller vegetation that traps large amounts of SWE, but accounts for only a small proportion of the total land cover within the satellite's IFOV.

5.4 Satellite Scale: snow survey SWE versus passive microwave estimated SWE

To assist in the identification of the dominant factors associated with passive microwave underestimation of SWE in the tundra, Environment Canada's open prairie algorithm was applied to both the airborne and spaceborne microwave brightness temperatures measured over the tundra study site. At the satellite scale, a single spaceborne SWE retrieval is estimated from the microwave emission emanating from surface found within the tundra study site. Table 5.5 compares the areal-weighted

Table 5.5 Tundra study site SWE versus brightness temperature estimated SWE

Snow Survey		Microwave Brightness Temperature		
		Open Environment Algorithm = -20.7 - 2.59(37V - 19V)		
SWE (mm)		SSM/I (8 days)	AMSR-E (8 days)	Airborne (1 day)
Averge	111	59	61	50
Min	0	42	34	-26
Max	680	75	79	135
Standard Deviation	77	10	15	19

average study site SWE to the spaceborne estimated SWE and the average SWE estimated from all 9500 airborne microwave brightness temperatures. The snow surveys from this study confirm that Environment Canada's open environment SWE algorithm consistently underestimates in the tundra. The tundra study site areal-weighted SWE average is almost twice the magnitude of the spaceborne estimated SWE, and is over two times the magnitude of the average airborne SWE retrieval. Interestingly, the average satellite SWE estimates in Table 5.5 for both SSM/I and AMSR-E (~60mm) more closely match the average SWE of the short vegetation class <1m (~78mm) compared to the average SWE of the tall vegetation class (~185mm) shown in Table 5.4. Therefore, it appears that Environment Canada's open environment algorithm satellite SWE estimates are more influenced by the short vegetation class open tundra, accounting for 70 percent of the study site land cover, and does not capture the deeper SWE deposits found in the taller vegetation class >1m that account for the remaining 30 percent of land cover within the study site.

Two other interesting points to take away from Table 5.5 are the wide range of snow survey SWE values recorded across the tundra study site (0mm - 680mm) and the negative value of the minimum airborne estimated SWE (-26mm). The wide range of snow survey SWE introduces some problems discussed in section 2.2.3 and Table 2.2, concerning the issues involved with microwave emission from snowpacks in excess of 200mm of SWE. Approximately 30 percent the tundra study site land cover had SWE values in excess of, or just below 200mm, making this a very relevant issue.

In Figure 5.3, the brightness temperature measurements for a snowpack under natural conditions are plotted as a function of SWE (Mätzler et al., 1982). Snowpacks with SWE magnitudes greater than

200mm begin to emit their own microwave energy. The snowpack emission leads to higher brightness temperatures measured over sites with very high SWE. Figure 5.3 illustrates how sites with very different SWE magnitudes (90mm and 310mm) emit the same microwave brightness temperature (220 K). The linear relationships used in existing SWE algorithms mean that the lower SWE values are always retrieved, and therefore underestimation occurs. The data in Figure 5.3 were collected in Switzerland at 2450m above sea level from the beginning of the snow season through to the late winter condition at the end of March between March 1977 and December 1980 (Mätzler et al., 1982).

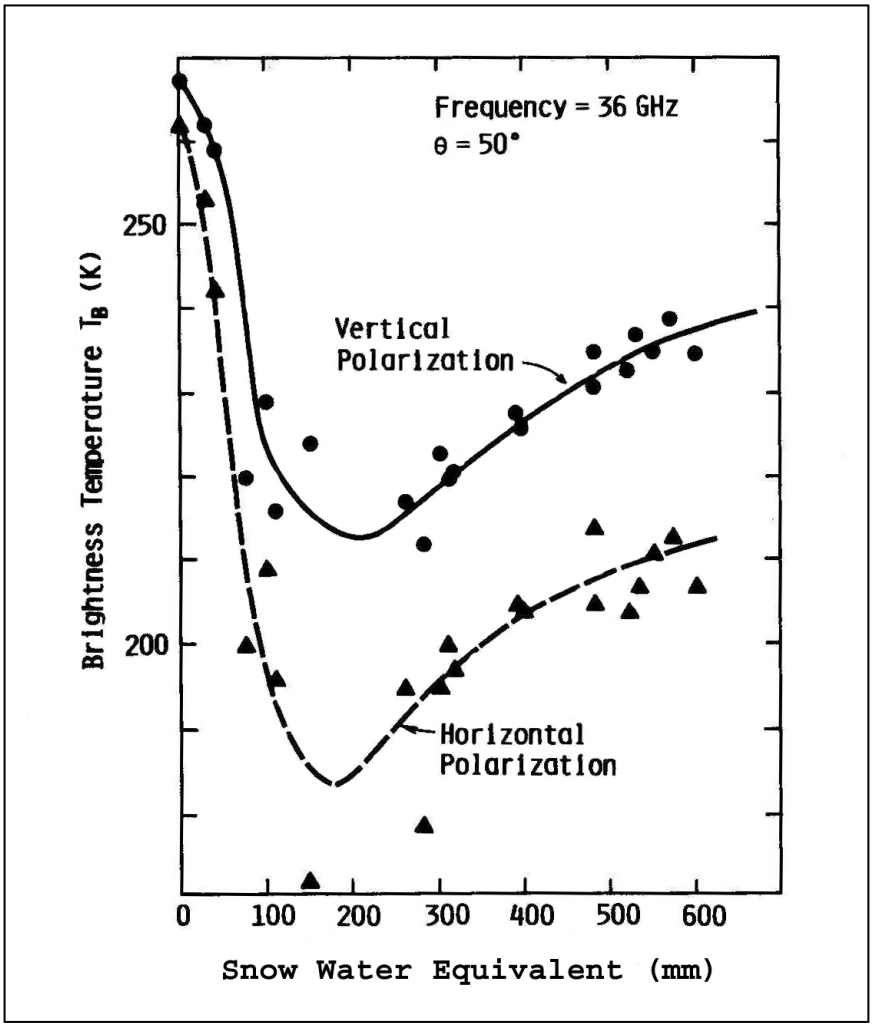

Figure 5.3 Brightness temperatures at 36GHz horizontal and vertical polarization at 50°nadir angle as a function of SWE (Source: Mätzler et al., 1982 – Modified by: Toose 2007)

The second point to take away from Table 5.5 is the negative minimum SWE retrieval from the airborne brightness temperatures. The airborne brightness temperatures have much smaller footprints (~70m) and thus are able to pick up on the sub-grid scale variability in microwave emission within the footprint of the spaceborne microwave data. Analysis of the high-resolution airborne data has shown that Environment Canada's existing SWE algorithm is particularly sensitive to some (but not all) lake features within the study site, and this sensitivity is contributing to the estimation of negative SWE values. The spatial relationship between lakes and negative SWE estimates are explored in section 5.6. It is clear to see how negative SWE values estimated over small proportions of the tundra study site would contribute to an underestimation of SWE at the satellite scale.

5.5 Local scale: snow survey SWE versus 37GHz–19GHz brightness temperature difference

The relationship between SWE and the 37GHz – 19GHz brightness temperature difference is the basis for almost all contemporary SWE algorithms. When a particular brightness temperature is measured by the radiometer it is used to predict a SWE value. A rigorous relationship between these two variables has yet to be defined in the tundra environment. To explore the reasons why, a transect of measured SWE from snow survey site 98 was plotted with the airborne brightness temperature difference (37GHz – 19GHz) measured for the same site. A picture of the land cover found at site 98 is provided in Figure 5.4. Site 98 appears to be homogeneous land cover and falls into the short vegetation category of <1m in height and is described as an open polygonal tundra site. Quickbird imagery of site 98 is available from Google Earth™ and is provided in Figure 5.5, showing a high concentration of ponds which are very hard to distinguish from the frozen tundra when looking at the picture in Figure 5.4. The SWE was measured along a ~550m transect between waypoints 207 to 208 to 209 shown in Figure 5.5. The snow survey transect falls within the flight line footprint while crossing both ponds and tundra, with variations in micro-topographic relief producing sastrugi patterned snow (seen in Figure 5.4). The micro-topographic variation produces dramatic fluctuations in measured SWE shown in Figure 5.6, with ranges of over 100mm within the same airborne brightness temperature footprint. The airborne data footprints are illustrated in Figure 5.6 at the top of the graph by the oblong circles with the 37GHz – 19GHz brightness temperature difference provided inside. Each oblong shape represents the extent of the ~70m airborne data footprint. The blue line below each white circle represents the range of measured SWE within that airborne data footprint.

Figure 5.4 This is a photograph of snow survey site 98. This site is described as an open polygonal tundra site with frozen ponds which falls into the short/non vegetated category of <1m in height. An approximate scale is provided for foreground image features.

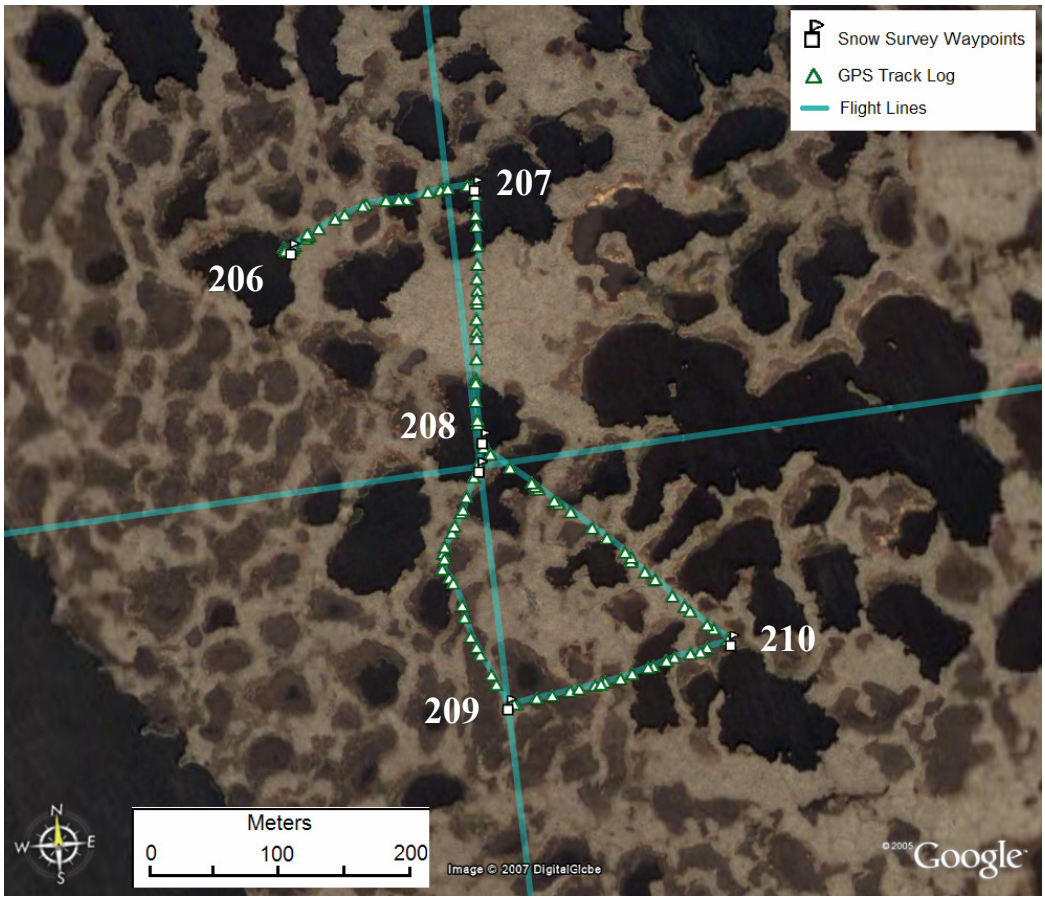

Figure 5.5 The stepped-line sampling approach used at snow survey site 98. High resolution (2.5m) Quickbird imagery is used as the background image and highlights the high concentration of ponds (black = water, grey brown = tundra).

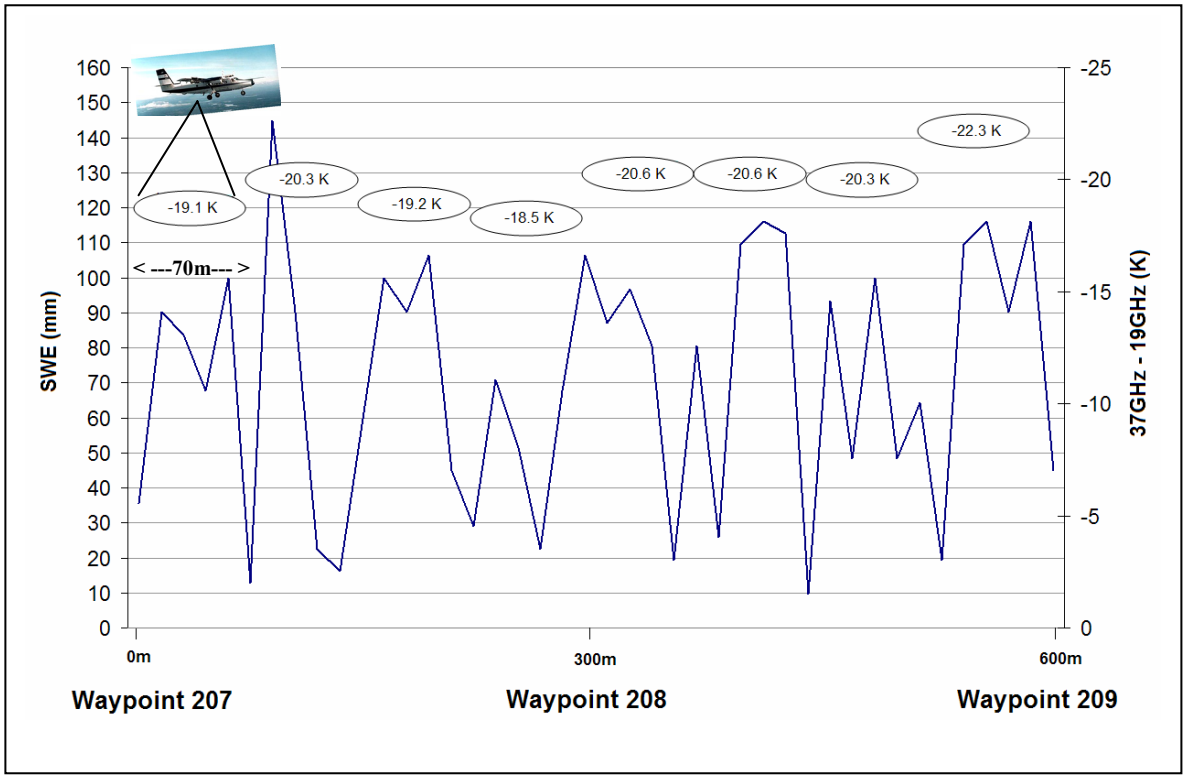

Figure 5.6 The solid line illustrates the fluctuating SWE levels (left y-axis) measured along a ~550m transect at snow survey site 98. The oblong shapes along the top represent the extent of the eight airborne brightness temperature ~70m footprints recorded along the same transect. The brightness temperature difference between the 37GHz – 19GHz frequencies (right y-axis) are shown inside the airborne data footprints.

There is very little change in brightness temperature difference along the entire transect highlighting a lack of response to fluctuating SWE levels. Figure 5.6 illustrates the difficulty in using high resolution brightness temperature measurements to estimate SWE in an environment with such heterogeneous SWE levels controlled by local sastrugi snow patterns and micro-topographic relief. The scale of SWE variation is much finer (meter to meter) than the airborne measurements and thus is not captured by the high resolution airborne brightness temperatures. This problem is similar to estimating SWE in areas where SWE exceeds 200mm, because the same brightness temperature can be associated with more than one SWE value as discussed in section 5.4 and illustrated by Figure 5.3.

5.6 Exploring the cause of extremely low estimated airborne SWE values

All ~9500 airborne SWE estimates were mapped using GIS software to identify which sub-grid features are influencing the airborne brightness temperatures leading to the estimation of negative SWE values. Figure 5.7 shows all flight lines and the calculated SWE estimates for the tundra study site and the lake mask which extends just beyond the boundaries of the study area. It is quite obvious in Figure 5.7 that the lowest SWE estimates (darkest) are measured over some of the larger lake features within the study area. To explore this further, all airborne SWE estimates were overlaid with the lake mask, and a count of how many SWE estimates were measured over lakes was conducted for each range of airborne estimated SWE shown in the legend of Figure 5.7. The results of this count are provided in Table 5.6. It is useful to note that the total percentage of all airborne brightness

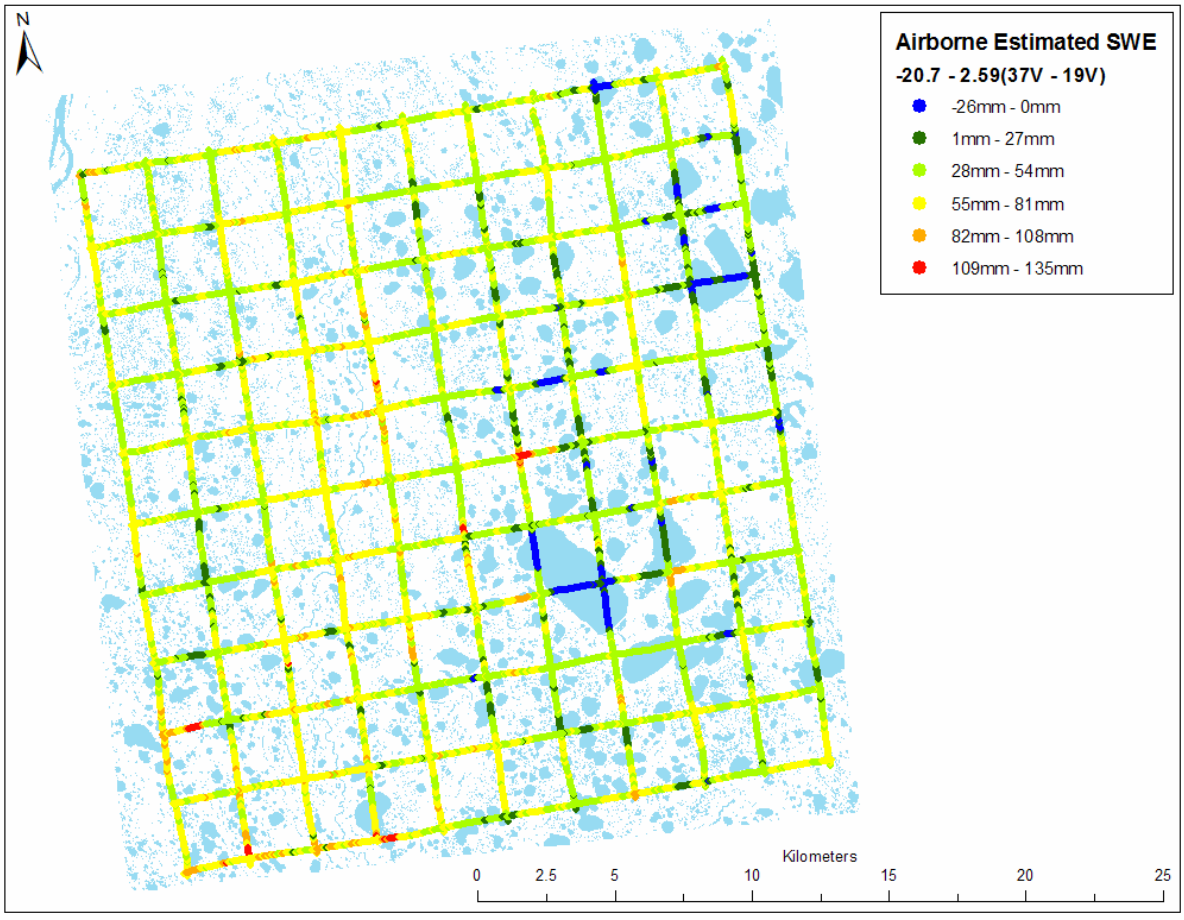

Figure 5.7 Tundra study site airborne estimated SWE. The lowest SWE values are predominantly estimated over lake features. However, not all lakes have low SWE estimates.

temperatures measured over lakes is 25 percent, just slightly higher than the overall study site lake cover fraction of 23 percent so the grid flight line approach provided a reasonably weighted dataset. Table 5.6 shows that the two lowest ranges of SWE values account for only 10 percent of all airborne measurements, (-26mm – 0mm and 1mm - 27mm) but are mostly measured over lakes (94 percent and 68 percent respectively). This indicates that lake features are likely one of the dominant factors driving the underestimation of SWE in the tundra environment at the sub-grid satellite scale because the snow surveys have already shown that the measured SWE over lakes is comparable to the surrounding tundra, and therefore the underestimation is most likely caused by sub-snowpack lake ice characteristics. The majority of the two middle ranges of SWE estimates (28mm – 54mm and 55mm – 81mm) accounting for 86 percent of all airborne measurements are mostly measured over land. The two highest ranges of SWE values accounting for only 3 percent of all airborne measurements (82mm – 108mm and 109mm – 135mm) and are almost all measured over old dried lake bed features with a high concentration of willow bushes present, and snow survey results indicate a large amount of SWE found in these landscape features.

Table 5.6 Extremely low airborne SWE estimates are mostly measured over lake features.

SWE Range	Total Count of Airborne Measurements	Percent of Total Airborne Measurements	Count Over Lakes	Percent of SWE Class Measured Over Lakes
-26mm to 0mm	229	2%	216	94%
1mm to 27mm	745	8%	508	68%
28mm to 54mm	4688	49%	1148	24%
55mm to 81mm	3491	37%	450	13%
82mm to 108mm	319	3%	46	14%
109mm to 135mm	47	0%	13	28%
Total SWE Estimates	9519	100%	2381	25%

5.7 Summary

Analysis of the snow survey data has shown that similar snow depths, SWE, and snow densities are found within land covers with short vegetation less than 1m in height (including lakes), versus land covers with tall vegetation greater than 1m in height. The short vegetation class typically has higher density, lower snow depths, and less SWE compared to the taller vegetation class which usually has lower density, but greater snow depths and subsequently higher SWE. Satellite SWE estimates are more similar to the short vegetation class average SWE measurements which encompass approximately 70 percent of the entire tundra study site but account for only 50 percent of the study

site SWE, providing some insight on why current satellite scale SWE underestimation occurs. In addition, passive microwave SWE retrievals over deeper snowpacks (greater than 200mm of SWE), such as found within the tall vegetated land cover are too low, also contributing to satellite scale SWE underestimation. The airborne SWE estimates are also too low because even the high resolution airborne brightness temperatures cannot capture the extremely local scale SWE variability found in the tundra environment. Further complicating SWE retrievals are the microwave emission from some tundra lakes found within the tundra study site that are quite different from the surrounding terrestrial land surfaces, and produce negative SWE estimates, potentially contributing to an underestimation of passive microwave SWE retrievals.

Chapter 6
Tundra Lake Ice Analysis Results

6.1 The influence of tundra lakes on microwave emission

The preliminary analysis conducted in section 5.6 indicated that some lake features (not all) are likely a dominant factor driving the passive microwave underestimation of SWE in the tundra environment. The results of the snow survey analysis in section 5.2 showed that the measured SWE over lakes is comparable to the surrounding tundra, and therefore the extremely low SWE values estimated over some lake features cannot be a reality, but instead are most likely caused by sub-snowpack lake ice characteristics. To further explore the influence of lakes on passive microwave SWE estimation the 19GHz and 37GHz vertically polarized microwave brightness temperatures of two flight line segments illustrated in Figure 6.1, were examined in greater detail.

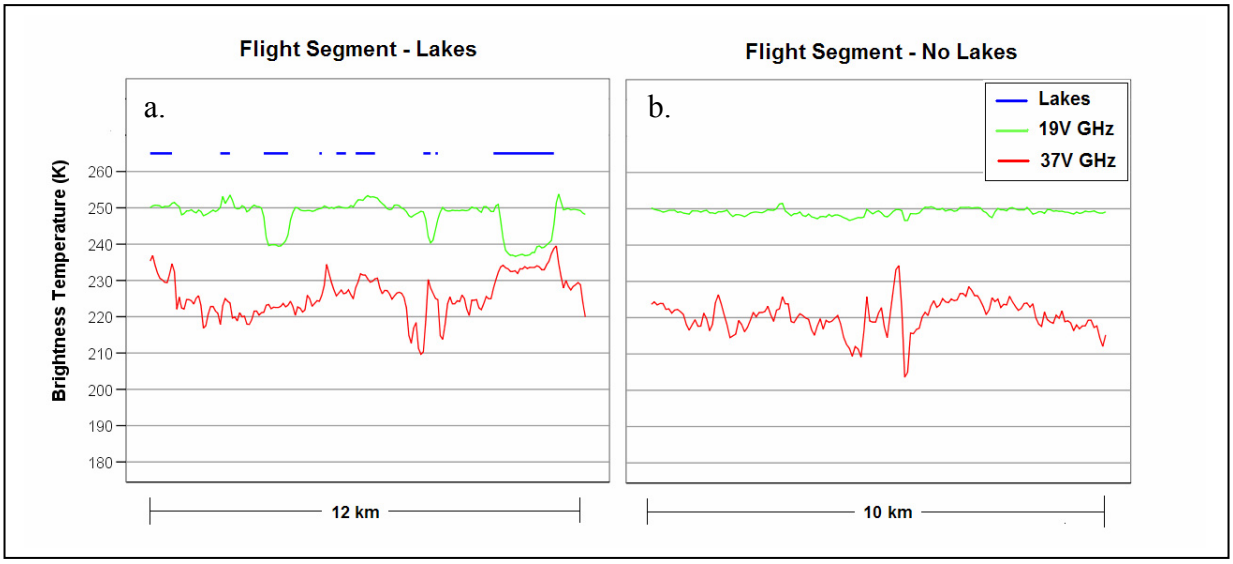

Figure 6.1 Vertically polarized 19GHz and 37GHz passive microwave brightness temperatures (K) are plotted out versus time for two flight line segments: a.) 12km long segment that passed over both land and lakes, and b.)10km long segment that passed strictly over land with no lakes. Those brightness temperatures directly below the straight dark lines (blue) at the top of graph a.) were measured over lakes.

Figure 6.1a contains the brightness temperatures measured along a 12km long transect which passes over a number of lakes of various sizes. The locations of these lakes on the flight line are indicated by the solid dark lines (blue) along the top of the graph. All brightness temperatures directly below these lines were measured over lakes. Figure 6.1b contains the brightness temperatures measured along a

10km long transect which passed over tundra with no lakes (transect passed over a number of small ponds under 200m x 200m). In both graphs, the 37GHz brightness temperatures show quite a large range of variability, on the order of 30K. It is not surprising that the 37GHz is so variable, because this frequency has shorter wavelengths that are more susceptible to snowpack scattering due to variations in SWE, as well as other factors discussed in section 2.2.3. A more notable contrast between the line graphs exists in the variability of the 19GHz frequency. In Figure 6.1b, where the flight line passes over land with no lakes, there is very little variation in the 19GHz brightness temperatures with a range of 5K. The longer wavelengths of the 19GHz frequency appears largely unaffected by the changing snow or environmental influences along the 10km flight transect and acts as a stable reference value to compare to the 37GHz frequency. However, for Figure 6.1a, where the flight line passes over a number of lakes, there is a very noticeable, non-random variability with a range of 17K. The 19GHz brightness temperatures drop over 10K as the flight line transitions from land to lake features. The drop in brightness temperatures occurs three times, for three separate lakes along the 12km transect, and is repeated at other lakes across the study area. A similar systematic pattern of brightness temperature fluctuation is not seen for the 37GHz frequency over lakes. This is important to note because the role of the snow insensitive 19GHz frequency in contemporary SWE algorithms is to act as a stable reference value to compare to the 37GHz frequency. In most algorithms, a change in the brightness temperature difference between these two frequencies (37GHz – 19GHz) for a cold dry snowpack over frozen ground is usually linearly related to changes in SWE, and its effect on the volume scattering of microwave emission at the 37GHz frequency. Clearly though, it is not only the volume scattering of the 37GHz that is resulting in a smaller 37GHz – 19GHz brightness temperature difference over lakes in the tundra environment, it is also the pronounced drop in the 19GHz brightness temperatures contributing to the smaller differences.

The variability in the 19GHz frequency for Figure 6.1a, is focused on three major pulses that coincide exactly with being measured over lake features. However, the dark solid lines at the top of Figure 6.1a, indicate that the flight segment passed over more than 3 lakes, again highlighting the fact that not all lakes influence microwave emission in the same way. Figure 6.2 indicates one land and three lake locations along the 12km flight line that were investigated more closely to explore how brightness temperatures vary between land versus lake and lake versus lake, and how these differences affect SWE retrievals. Snow surveys were conducted within the IFOV of the airborne radiometers at the Land, Lake 1 and Lake 2 locations indicated in Figure 6.2. There were no snow surveys in IFOV at the Lake 3 location, however two survey sites 2 to 3km away were conducted on

the same body of water directly below a parallel flight transect. Very similar brightness temperatures for the same body of water were recorded along that parallel transect and therefore a comparison of those measured SWE values with the brightness temperatures measured along this flight transect is deemed acceptable.

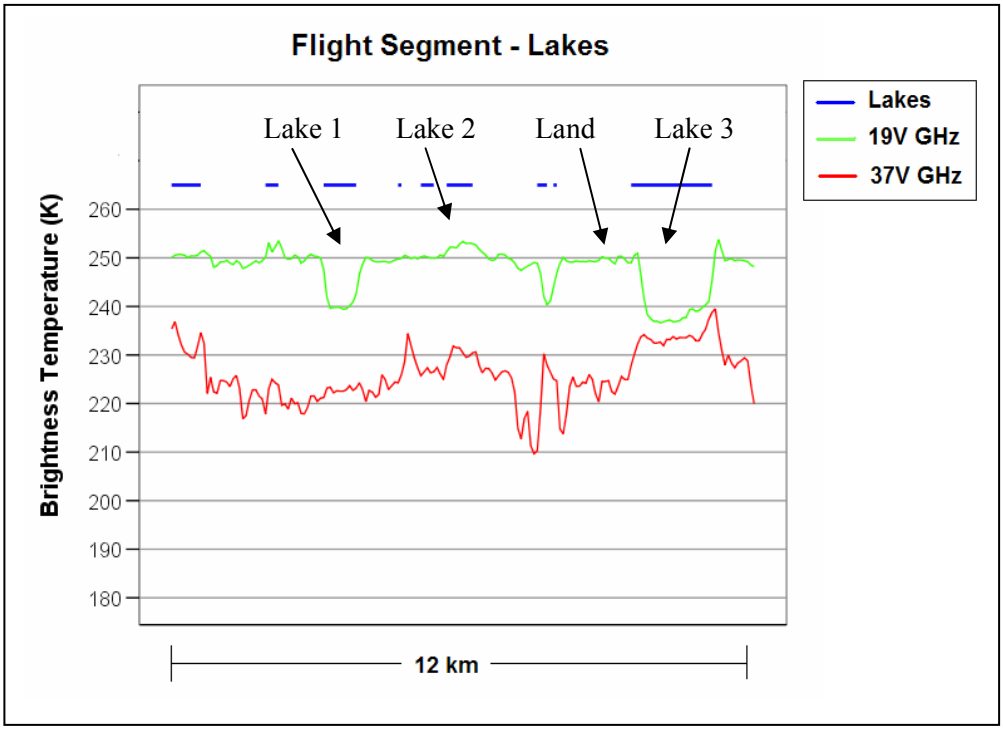

Figure 6.2 Vertically polarized 19GHz and 37GHz passive microwave brightness temperatures (K) are plotted out versus time for a 12km long flight line that passes over multiple lakes. The airborne brightness temperatures and estimated SWE are compared to measured SWE in Table 6.1 at each of the four sites indicated in the graph (3 Lake sites and 1 Land site).

Table 6.1 provides a summary of the mean brightness temperatures, brightness temperature difference, airborne estimated SWE, measured SWE, and snow density for four locations along the 12km flight transect in Figures 6.2. All airborne estimated SWE are far below the measured SWE values, as already established in section 5.4. The brightness temperature difference is the greatest at the Land site location, subsequently producing the highest airborne SWE estimate of 46mm, which is just below the study site average airborne estimate of 50mm. The Land site and Lake 3 site have similar measured SWE values and far different airborne estimated SWE, once again reinforcing that it is most likely the sub-snowpack lake ice characteristics that are controlling the difference in microwave emission from land versus lake and not the snow properties. All three lake sites have

lower airborne SWE estimates than the Land site, with Lake 1 and Lake 3 producing the lowest airborne SWE values. Figure 6.2 illustrates the dropping 19GHz brightness temperatures for Lake 1 and Lake 3 providing an explanation for the extremely low SWE values over these sites. Curiously, the Lake 3 site which has the highest measured SWE also has the highest measured 37GHz brightness temperature, which is the complete opposite of what is expected, it should have the lowest 37GHz values. The higher 37GHz brightness temperatures at the Lake 3 location may be attributed to the higher snow density measured at this site, with greater emission emanating from the denser snowpack, such as would be found from a lower density deeper snowpack greater than 200mm as discussed in section 5.4. The higher 37GHz and lower 19GHz brightness temperature measured at the Lake 3 site result in the impossible mean value of -9mm of airborne estimated SWE.

Table 6.1 Summary of the mean brightness temperatures, brightness temperature difference, airborne estimated SWE, measured SWE, and snow density for four locations along the 12km flight transect in Figure 6.2, highlighting the different microwave response between land versus lake and lake versus lake

	Mean Brightness Temperatures (K)		Mean 37V - 19V	Mean Airborne Estimated SWE	Snow Survey Site	Mean Snow Survey SWE	Mean Snow Survey Density
	37V Ghz	19V Ghz					
Land	224	250	-26K	46mm	Site 40	87mm	0.318
Lake 1	223	240	-17	24mm	Site 14	63mm	0.304
Lake 2	230	252	-22	37mm	Site 29	54mm	0.283
Lake 3	232	237	-5K	-9mm	Sites 41 & 41A	91mm	0.355

Lake 2 does not have the dropping 19GHz brightness temperatures that are found at the Lake 1 and Lake 3 sites and therefore the brightness temperature difference at this location is greater than the other lake sites, subsequently producing an airborne SWE estimate more similar to the Land site than the other Lake sites. To understand why the 19GHz frequency is influenced by some lakes and not others an analysis of a winter time series of RADARSAT ScanSAR Wide imagery was conducted to extract probable sub-snowpack lake ice information to construct a regional tundra lake ice map.

6.2 Creating a regional tundra lake ice map from synthetic aperture radar

Previous studies of tundra lake ice properties using SAR have focused largely on defining the relationships between backscatter as a function of time and incident angle (Jeffries et al, 1994, Morris et al., 1995, Duguay et al., 2002, and Duguay and Lafleur, 2003). There has also been some work to create regional lake ice maps of shallow tundra lakes by French et al. (2004). They created a regional tundra lake ice map for the north slope of Alaska defining those lakes frozen to bottom or not based on a supervised classification of a single late season winter SAR image. This study applied the current techniques of using a SAR winter time series for creating backscatter intensity plots to identify a known (probable) set of lakes that were most likely frozen to bottom or had free-floating ice (most likely because no field observations were conducted). Once the SAR time series was created and the known set of lake ice types were identified, a principal component analysis was conducted solely on the lake features within the study area to identify areas within the time series that had similar levels of backscatter variance over the course of the winter season, highlighting groups of lakes that likely had similar lake ice properties. The set of lakes with known (probable) lake ice characteristics based on backscatter intensity patterns were then used for interpreting the principal component outputs so that training sites could be defined that would be used as inputs into a supervised classification, resulting in a regional tundra lake ice map identifying lakes frozen to bottom or not. The production of a regional tundra lake ice map provided a potential explanation on why the longer wavelength 19GHz microwave brightness temperatures were influenced differently by different tundra lakes.

6.2.1 RADARSAT ScanSAR Wide backscatter intensity summary plots

Using the work of Jeffries et al. (1994), Morris et al. (1995), and Duguay et al. (2002) as examples, 14 lakes were analyzed and the backscatter values were plotted over time as described in section 4.4.3 For most lakes, the average backscatter value of between 10 and 6 RADARSAT pixels was recorded for each of the four image dates in the time series and then plotted versus time. Out of the 10 lakes identified as either free-floating or frozen to bottom using the 6.9GHz frequency, only two of them (Lake 7 and Part B of Lake 1) did not match the typical backscatter intensity patterns of a lake with free-floating ice based on the results of the previous works of Jeffries et al. (1994), Morris et al. (1995), and Duguay et al. (2002). Instead the backscatter patterns more closely matched those of lakes with an unchanging ice type. Therefore a total of 12 lakes were used to create the backscatter intensity summary plots shown in Figure 6.3 for the tundra study site. The backscatter intensity patterns for three shallow tundra lakes from Morris et al. (1995) are provided in Figure 2.2 for

reference and comparison with Figure 6.3. Figure 6.3 illustrates the three types of lake ice plots defined: a.) free-floating lake ice, b.) frozen to bed lake ice (mid winter freezing) and c.) lakes that were unchanging, meaning they had consistently low backscatter values with very little backscatter variation over the winter season (possibly free-floating clear bubble-free ice or early season frozen to bed).

Although the expected pattern and progression of changing backscatter intensity values was seen for each type of tundra lake ice over the course of the winter, it should be noted that there was a difference in magnitude and decibel range for the backscatter intensity measured for this study compared to previous SAR lake ice studies. A comparison of the different ranges of backscatter dB measured by Morris et al. (1995) and Duguay et al. (2002) with this study for both early (November) and mid (March) winter conditions is provided in the following section 6.2.2.

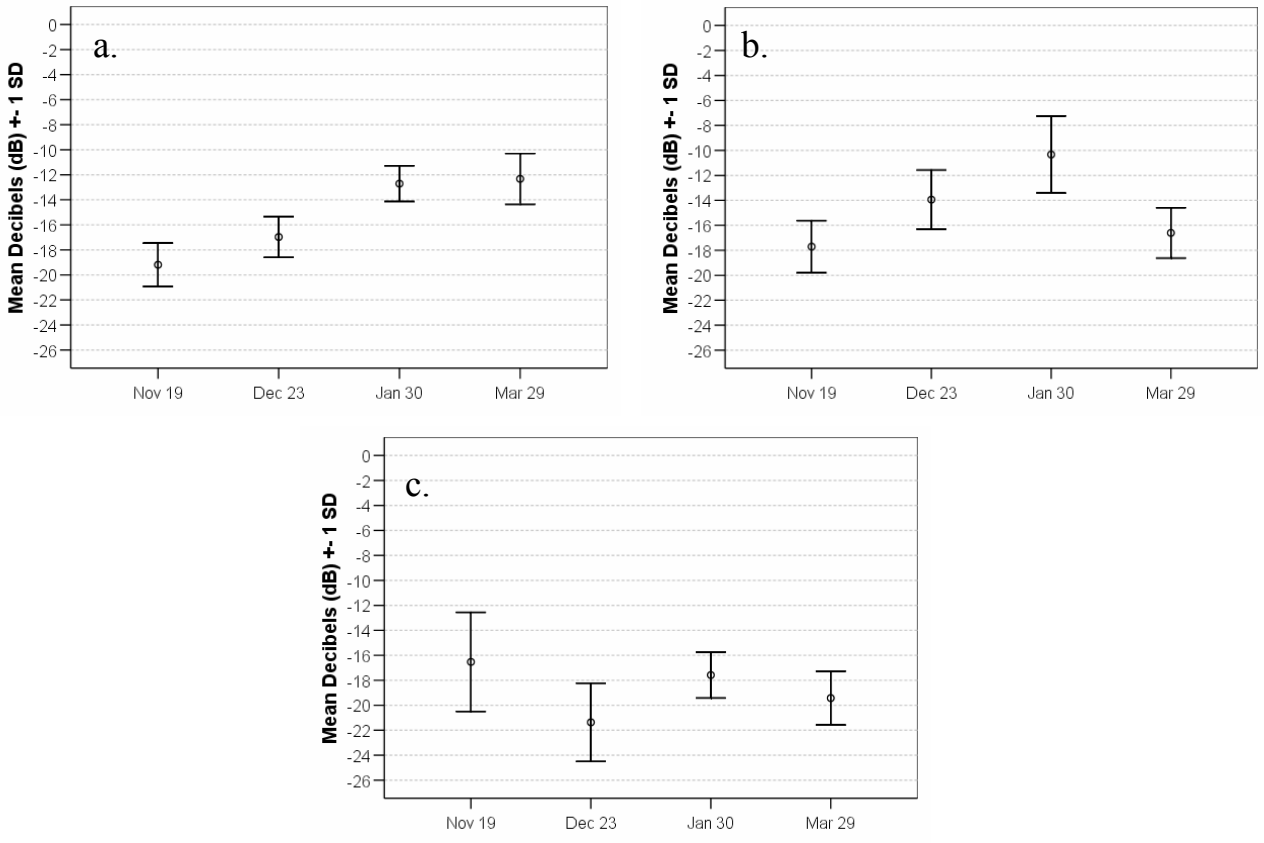

Figure 6.3 Backscatter intensity summary plots for mean backscatter values for each ice type are provided for a.) Backscatter intensity plot of free-floating ice, b.) Backscatter intensity plot of frozen to bottom (mid winter), and c.) Backscatter intensity plot of lakes with low variability and low or unchanging backscatter values.

6.2.2 Comparison of RADARSAT backscatter values with previous SAR lake ice studies

A comparison of the different ranges of backscatter dB measured by Morris et al. (1995) and Duguay et al. (2002) for different tundra lake ice types was conducted with this study for both early (November) and mid (March) winter conditions. The results are illustrated in Figures 6.4 and 6.5 and the different characteristics of the different SAR images compared are provided in Table 6.2.

Table 6.2 The sensor characteristics of each type of SAR imagery used in the comparison of backscatter values from this study with previous SAR lake ice studies.

Study	Satellite Sensor	Beam Mode	Frequency	Polarization	Resolution	Pixel Spacing	Incident Angle	Swath Width
Morris et al. 1995	ERS-1	N/A	5.3GHz	VV	240m	100m	20 - 26°	100km
Duguay et al. 2002	RADARSAT-1	S1	5.3GHz	HH	25m	12.5m	20 - 27°	100km
Toose 2007	RADARSAT-1	SWA	5.3GHz	HH	200m	100m	20 - 31°	500km

Using ERS-1 low resolution imagery, Morris et al. (1995) found that in mid-winter, shallow arctic lakes with floating ice had a range of backscatter values between -8 to -4 dB and that grounded ice had a range of backscatter values between -19 to -11 dB. The deeper tundra lakes were found to have backscatter values around -10 dB. Using RADARSAT-1 standard beam mode S1, Duguay et al. (2002) found that in mid-winter, tundra lakes with floating ice had a range of backscatter values between -9 to -2 dB and that grounded ice had a range of backscatter values between -15 to -11 dB. Using resampled RADARSAT-1 ScanSAR Wide A imagery for this study, the range of backscatter values for floating ice was -14 to -10 dB and for grounded ice the range of backscatter values was -18.5 to -14.5 dB. Figure 6.4 illustrates the range of backscatter values and middle points between those values for each type of ice for each study. The contrast between floating and grounded ice backscatter values for the previous studies was much larger than what was seen during this study. In this study there was only a small difference in backscatter between free floating and grounded ice (~1 dB). In fact, the backscatter values for floating ice measured in this study overlapped the range of backscatter values for grounded ice in both of the previous studies. However, the range of backscatter values for floating ice in this study is very close to the backscatter values for floating ice over deep tundra lakes defined by Morris et al. (1995), which could indicate that the lakes sampled at this study site may be deeper than many of the lakes sampled on the north slope of Alaska.

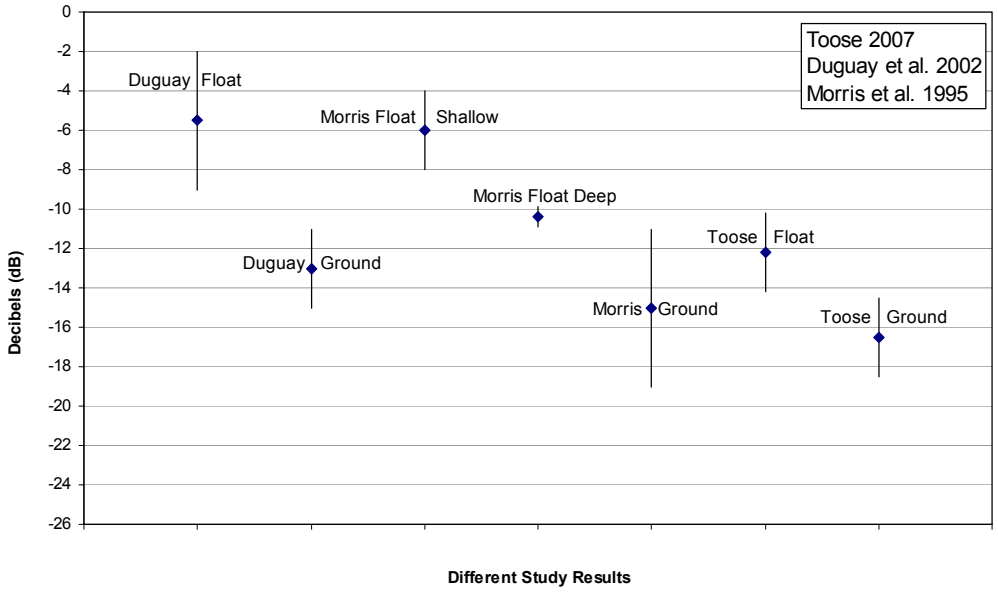

Figure 6.4 Range of backscatter values and the middle of that range for the tundra lakes from different SAR lake ice studies for mid to late winter (March). Float refers to free-floating ice, ground refers to lakes frozen to bottom, and float deep refers to lakes with free-floating ice on a deep tundra lake.

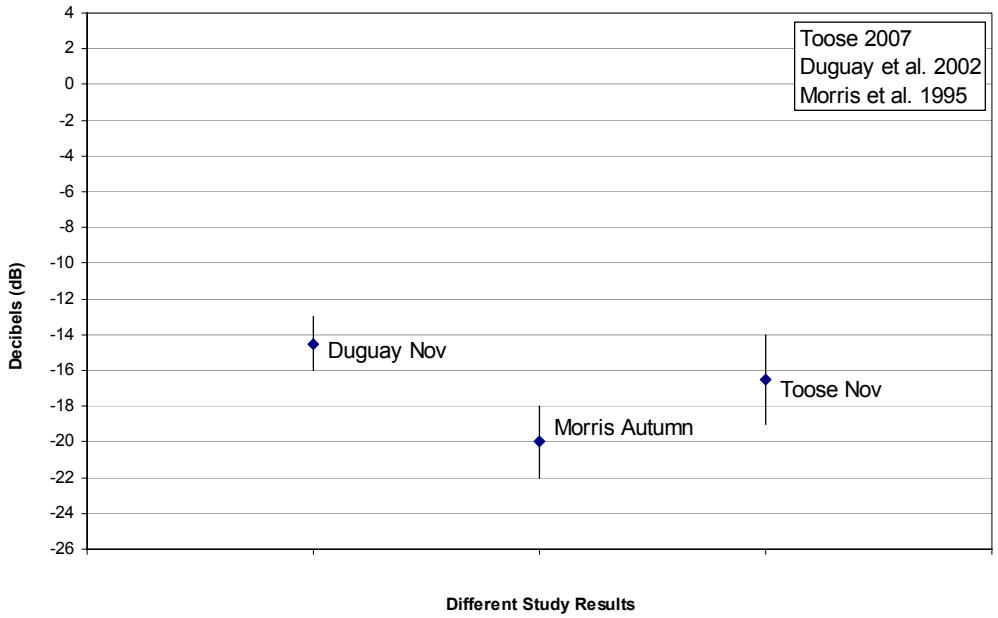

Figure 6.5 Range of backscatter values and the middle point of that range for tundra lakes from different SAR lake ice studies for early winter/late autumn (November).

However, Duguay et al. (2002) recorded their backscatter values for this same environment (albeit ~60km away) and measured much higher backscatter values. Jefferies et al. (1994) indicate that if the lake ice is devoid of bubbles then it would likely have a lower backscatter response, possibly hinting that the lakes in this study site may have lower bubble content compared to the previous studies, which could also help explain the lower range of backscatter values for grounded ice in this study compared to the previous works. The grounded ice backscatter values did however fall within the ranges of the grounded ice of the previous studies. Interestingly, the range of backscatter values for the early winter / autumn time period (November) is much closer overlapping across all studies (Figure 6.5). Another possible explanation for the smaller range of backscatter values measured in this study could be attributed to the coarser resolution of the SAR imagery used. Duguay et al. (2002) used RADARSAT-1 standard beam mode 25m resolution imagery for their study, and the original ERS-1 imagery used by Morris et al. (1995) was recorded at 25m resolution, but then resampled by the Alaska SAR Facility down to 240m resolution. So although Morris et al. (1995) never actually worked with the higher resolution data, the magnitude of backscatter values found in the low resolution ERS-1 data products could have been higher than the RADARSAT-1 ScanSAR Wide backscatter values because of the increased sensitivity of the original higher resolution measurements. This study used the RADARSAT-1 ScanSAR Wide 2x2 block-averaged data from the CIS, with a 200m resolution, that before resampling by the CIS, had a 100m resolution which is four time as coarse as the original ERS-1 data products and RADARSAT-1 standard beam mode resolutions. The coarser resolution may not be sensitive enough to pick up on the full range of backscatter values from different lake ice types.

Despite the differences in magnitude and ranges of backscatter values for each study discussed above, Figure 6.3 highlights the tundra study site backscatter intensity patterns nicely for the floating and grounded lake ice types indicating that these types of lake ice can likely be identified with some confidence. Lakes with matching backscatter intensity patterns were used to interpret the principal component analysis outputs and to define the training sites for the supervised classification used to make the regional tundra lake ice map.

6.2.3 Interpretation of the principal component analysis

Zoomed in subsets of the four output Principal Components (PCs) are shown in Figure 6.6. In a temporal PCA change detection both surface proportion and the magnitude of the changed area in an image determine which PC output will contain change information (Parra et al., 1996). It is the relative amount of variance between the changed area and the unchanged part in an image that determines which particular PCs contain change information. Small differences in magnitude may come out in low order PCs if they affect large areas. Conversely, large differences in magnitude may

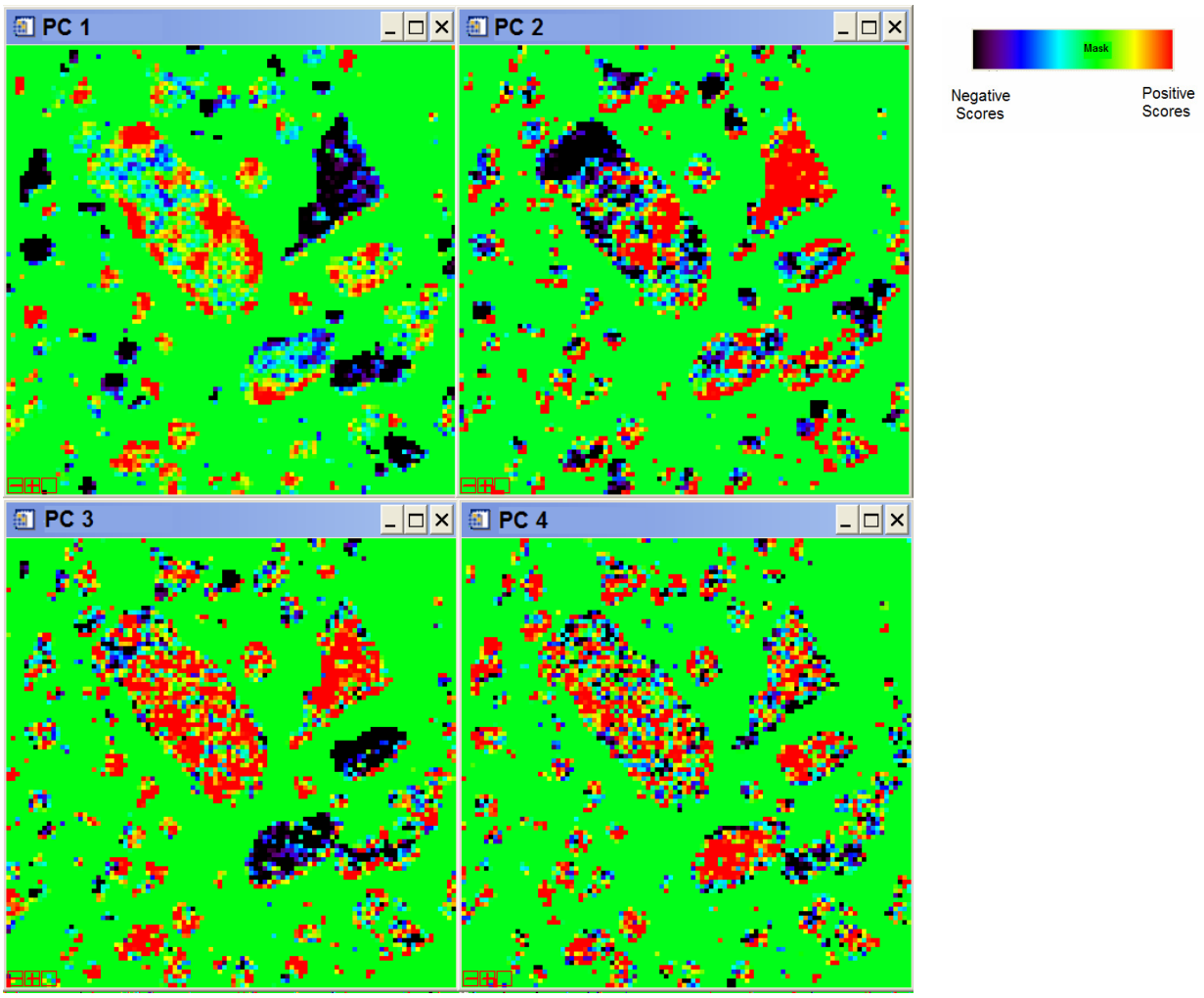

Figure 6.6 Zoomed in view of the output principal component images. Bright colours represent areas of high variance and dark colours represent areas of low variance. The colour green represents the masked land features. The principal component analysis was applied only to the water features.

Table 6.3 The total variance explained by each principal component.

Component	Eigenvalue		
	Total	% of Variance	Cumulative %
PC1	36.12	70.3%	70.3%
PC2	7.21	14.0%	84.3%
PC3	4.91	9.6%	93.9%
PC4	3.14	6.1%	100.0%

come out in high order PCs if they occupy only a small proportion of the analyzed area (Parra et al., 1996). The lower order outputs for a PCA of a SAR time series typically contain significant information, while the higher order PCs are dominated by speckle noise. The total variance explained by each principal component output is provided in Table 6.3. The first three PCs (1,2,3) contained 93.9% of the variance.

PC 1 accounts for 70.3% of the explained variance. The dark areas in PC1 represent negative scores and these areas correspond very well with the unchanging ice type defined by the backscatter intensity plots. The dark features in PC1 were used to define the training sites for the supervised classification of the unchanging ice type. It is difficult to tell apart the free-floating and grounded ice types in PC 1 because both have high positive scores and appear bright in Figure 6.6.

PC 2 accounts for 14% of the explained variance. The dark areas in PC 2 represent negative scores and these areas correspond very well with the free-floating ice defined by the backscatter intensity plots. These dark areas were used to help define the extent of the training sites for this type of ice.

PC 3 accounts for only 9.6% of the explained variance. The amount of noise is starting to increase in this PC, but some very important information can still be gained. The dark areas in this PC represent negative scores and correspond very well with the backscatter intensity plots for grounded ice (mid winter frozen to bottom) and these areas were used to help define the extent of the training sites for this ice type.

PC 4 accounts for only 6.1% of the explained variance. This PC had the most noise out of all PCs and there was no obvious spatial pattern or lake ice feature which stood out. No training sites were defined using this PC and it was not used as an input into the supervised classification.

6.2.4 Accuracy assessment of the regional tundra lake ice map

Using the backscatter intensity plots defined in section 6.2.1, and the principal component outputs defined in section 6.2.3, 6 training sites for unchanging and grounded lake ice and 5 training sites for free-floating lake ice were identified in the winter time series principal component output images. These training sites were used as inputs into a minimum distance supervised classification that was conducted on the first three PC output images (PC 1, PC 2, PC 3).

The resulting lake ice classification map had four classes that are listed in Table 6.4, with the breakdown of the proportion of study area devoted to each class. A zoomed in subset of the regional lake ice classification map is provided in Figure 6.7. At the RADARSAT ScanSAR Wide resolution, lakes account for approximately 14 percent of the study area which is substantially lower than the 23 percent calculated from the high resolution lake mask, indicating that the tundra study site is covered by a lot of water, but the majority of the water is found in small ponds and wetlands. The proportion of land cover provided in the supervised classification devoted to each ice type is 3%, 5%, and 6% for unchanging, free-floating and grounded ice types respectively. According to this lake ice map the percentage of the type of lake ice within the study area is almost equal between the grounded ice and free-floating ice. As mentioned previously, it is difficult to tell whether the unchanging ice type is simply early season grounded lake ice, or is free-floating bubble-free lake ice, so therefore there is some uncertainty in the true proportion of the study area devoted to free-floating and grounded ice.

Table 6.4 Percent of total land cover for each class in the supervised classification of the regional lake ice map.

Regional Lake Ice Map Classes	Proportion of Study Area	Accumulated Area
Unchanging Ice (Early Season Frozen to Bottom or Bubble Free Clear Ice)	3%	3%
Free-Floating Ice	5%	8%
Grounded Ice (Mid Season)	6%	14%
Land Mask	86%	100%

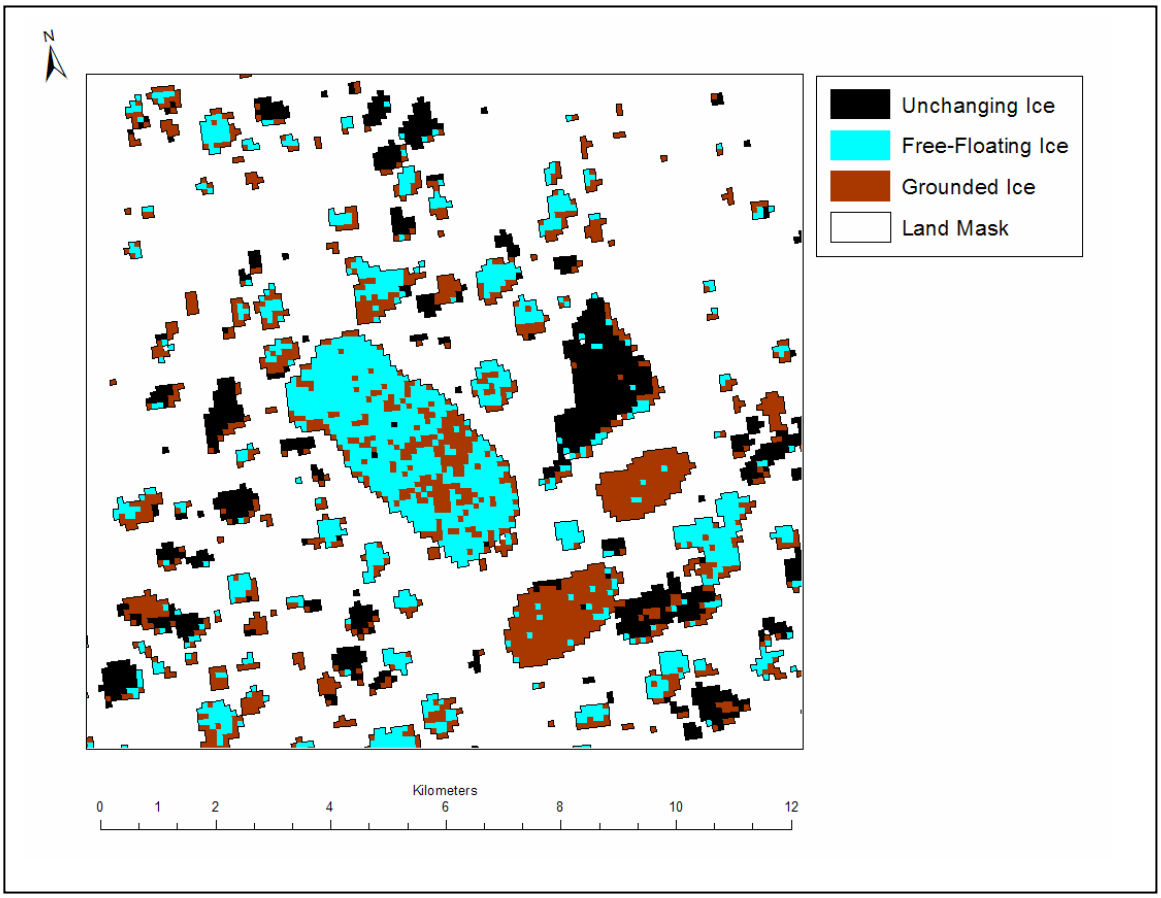

Figure 6.7 Supervised classification map of different ice types for a subset of the tundra site.

Without field observations, it is impossible to assess the absolute accuracy of this tundra lake ice map. Therefore, to evaluate whether or not the supervised classification made an accurate regional tundra lake ice map that highlighted the different lake ice types, new backscatter intensity plots were created from the SAR winter time series for a new set of lakes. The goal was to find out if the type of ice identified with the backscatter intensity plot matched the type of ice defined by the supervised classification. To accomplish this task ENVI's tool that links image displays was used to ensure that the same geographic pixels were being measured in the SAR winter time series and in the regional tundra lake ice type map. Figure 6.8 shows the location of 13 new lakes analyzed to create 17 new backscatter intensity plots. Some lakes had more than one type of ice defined in the regional lake ice map, and so two intensity plots were created for different parts of that lake. At each of the 13 new lake sites the average backscatter intensity value for 8 pixels of each ice type was calculated and then plotted versus time. The backscatter intensity plots were then visually compared to the original

training site intensity plots illustrated in Figure 6.3, and the accuracy of the classification was assessed. If the new backscatter intensity plots had the typical progression of changing dB values over the course of the winter season found in the summary backscatter intensity plots illustrated in Figure 6.3, then these lakes were deemed accurately classified. If the lakes did not match the backscatter intensity plots in Figure 6.3, then they were considered incorrectly classified. Table 6.5 illustrates the results of this accuracy assessment.

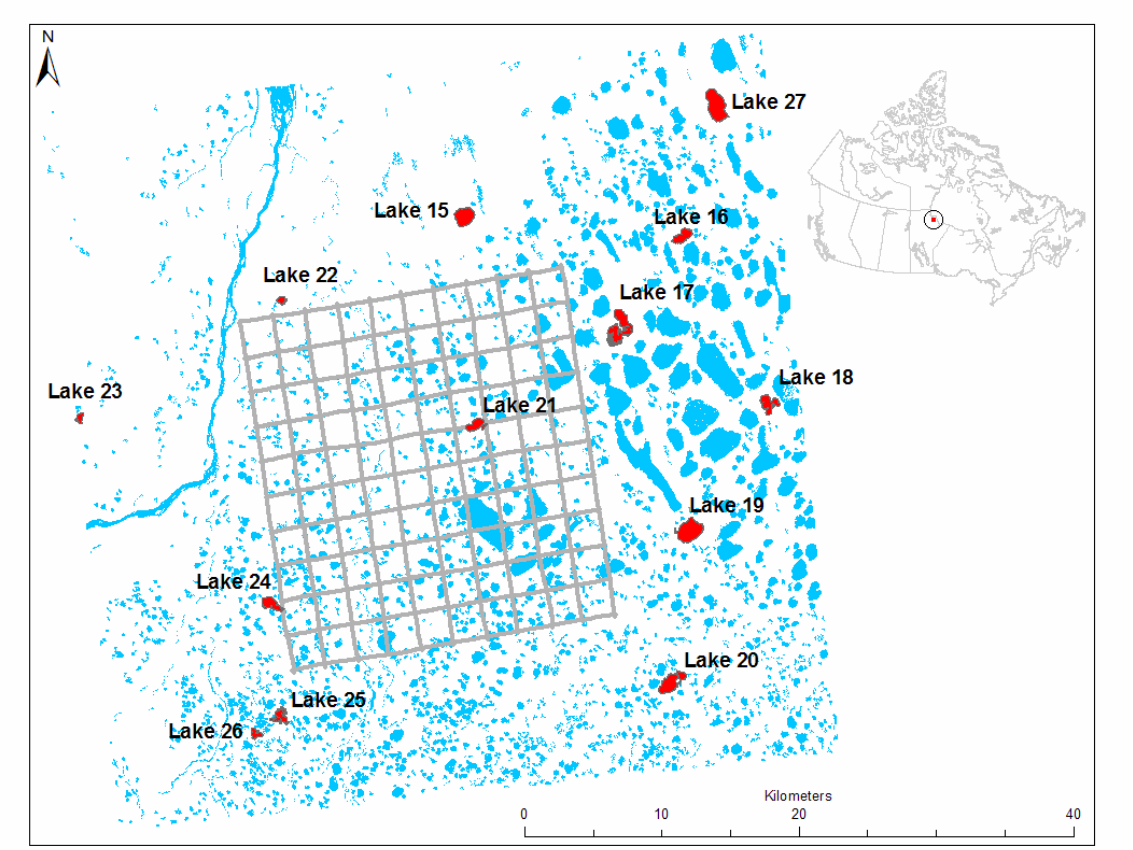

Figure 6.8 Map of the tundra lakes used to validate the performance of the supervised classification of the different tundra lake ice types. The validation lakes are highlighted a darker colour (red) and labeled.

Table 6.5 Results of the accuracy assessment of the regional tundra lake ice map.

Lake	Class	Matched?
Lake 15	Grounded	Yes
Lake 15	Floating	Yes
Lake 16	Grounded	Yes
Lake 16	Unchanging	Yes
Lake 17	Unchanging	Yes
Lake 17	Grounded	No
Lake 18	Grounded	No
Lake 19	Unchanging	Yes
Lake 19	Grounded	No
Lake 20	Floating	Yes
Lake 21	Floating	Yes
Lake 22	Unchanging	Yes
Lake 23	Unchanging	Yes
Lake 24	Floating	No
Lake 25	Floating	Yes
Lake 26	Unchanging	Yes
Lake 27	Floating	Yes
Overall	Yes = 76.5%	No = 23.5%
Grounded	Yes = 40%	No = 60%
Floating	Yes = 83.3%	No = 16.7%
Unchanging	Yes = 100%	No = 0%

Overall, 76.5% of all lake ice types evaluated were considered classified correctly and 23.5% were classed incorrectly. When the different ice types were examined individually, the results were a bit different. The grounded ice type was classed correctly only 40% of the time, the floating ice type 83.3% and the unchanging ice type 100% correct. For the free-floating and grounded ice lakes that were classed incorrectly, the actual observed backscatter intensity patterns were for the unchanging lake ice type. There was never a misclassification of grounded ice being confused with floating ice, or vice versa.

6.3 Interpreting the passive microwave airborne data with the regional tundra lake ice map

Tundra lake features were identified as one of the dominant factors causing extremely low SWE retrievals using passive microwave airborne brightness temperatures. However, only some lakes seemed to cause extremely low SWE values, while others did not. It was theorized that the reason for this difference was due to the microwave brightness temperatures being influenced by some lakes that had free-floating ice with liquid water below and not by lakes that were frozen to bottom. To investigate this theory, the regional tundra lake ice map produced was overlaid with the airborne estimated SWE (Figure 6.9), and the SWE distributions and were plotted out (Figures 6.10 and 6.11), for both land and lake categories and for each ice type found in the tundra lake ice map.

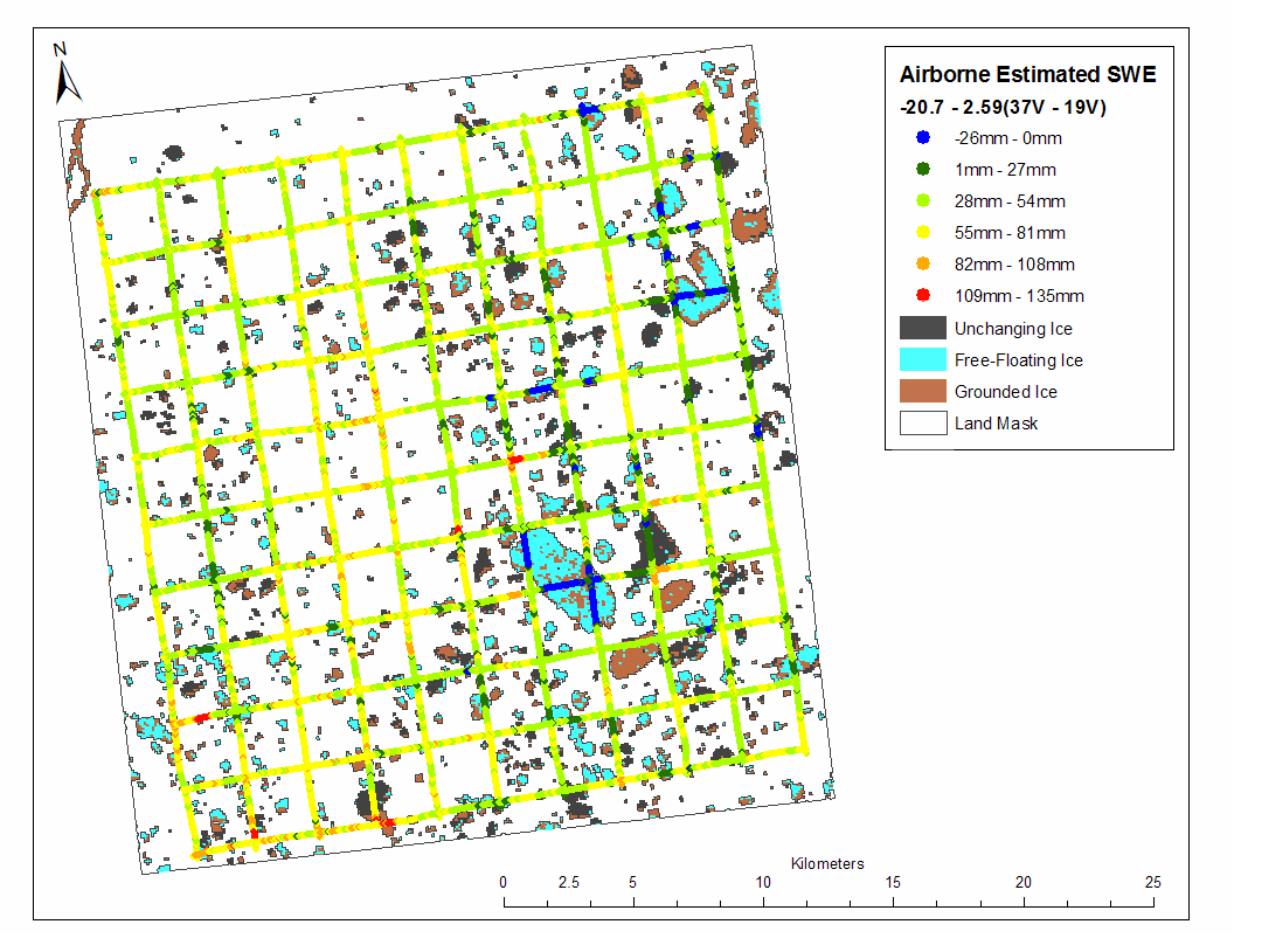

Figure 6.9 Illustrates the tundra study site airborne estimated SWE in relation to different lake ice types defined by the regional tundra lake ice map. The lowest SWE values (darkest airborne data colours) were predominantly estimated over the free-floating lake ice type.

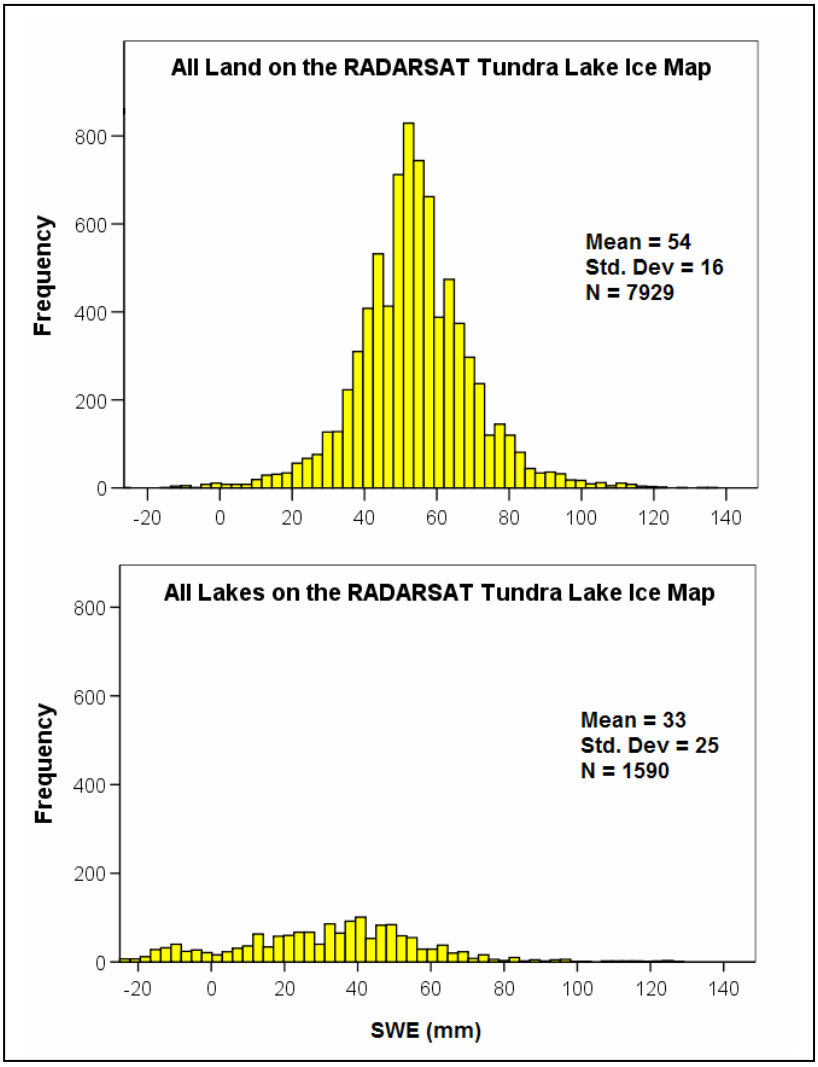

Figure 6.10 Distributions of airborne SWE measured over both land and lake classes found on the RADARSAT tundra lake ice map.

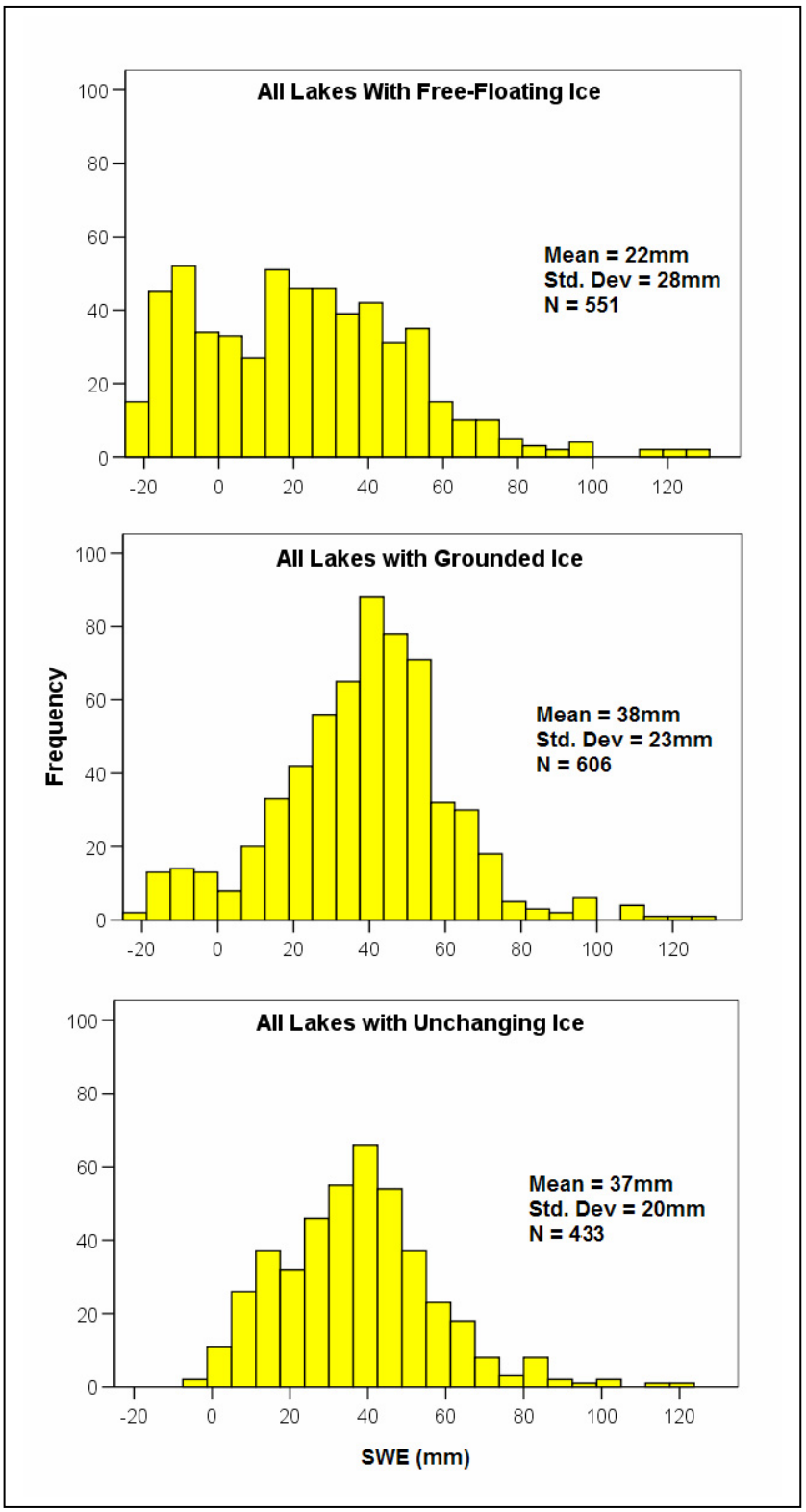

Figure 6.11 Distributions of airborne SWE measured over different lake ice types found on the RADARSAT tundra lake ice map

The 37GHz – 19GHz brightness temperature differences measured over the land mask class of the regional tundra lake ice map produced a mean airborne estimated SWE of 54mm, a value that was slightly higher than the 50mm mean of all land and lake airborne estimated SWE together. The 54mm land SWE was closer to the satellite SWE estimates listed in Table 5.5, indicating that the satellites may be less influenced by the tundra lakes because of the mixed influence of both land and lake with land accounting for a much higher proportion of the area within the radiometer's IFOV. It should be noted that the presence of a very small number of negative SWE values in the land category are likely a result of the coarse resolution lake mask employed in the development of the tundra lake ice map. Because of the coarse resolution, some smaller tundra ponds and lakes (less than 200m x 200m) that did not freeze to bottom are likely causing these extremely low airborne SWE values. The 37GHz – 19GHz brightness temperature differences measured over all the lakes in the regional tundra lake ice map were smaller than those of the land mask class, producing a lower mean airborne estimated SWE of 33mm. The SWE distribution of the lake class had a higher frequency of extremely low SWE estimates compared to the land class as expected, most like due to the influence of on the 19GHz frequency over lakes with free-floating ice.

The production of the regional lake ice map allowed for a more detailed analysis of the distribution of airborne estimated SWE based on different lake ice types. The mean airborne SWE for the grounded and unchanging ice types were 38mm and 37mm respectively. The free-floating ice type is of the greatest interest because in theory, lakes with this type of ice cause a pronounced drop in microwave emission in the longer wavelength microwave frequencies, which subsequently lead to the underestimation of SWE. The brightness temperature differences are the smallest over these lake ice types, producing a mean airborne estimated SWE of 22m. These results reaffirm the theory that the longer wavelength of the 19GHz frequency is being influenced by the liquid water below the ice.

Table 6.6 contains the mean airborne brightness temperatures and airborne estimated SWE values for all three different lake ice types and for land. The mean airborne estimated SWE for all lakes was lower than that estimated for land, because the brightness temperature difference between the 37GHz and 19GHz vertically polarized frequencies were smaller. As hypothesized and illustrated in section 6.1, lakes with free-floating lake ice had the lowest mean 19GHz brightness temperatures contributing to the lower SWE retrievals. Further contributing to lower SWE retrievals over lakes, were the lower

37GHz brightness temperatures measured over all lake ice types compared to land, despite the grounded and unchanging lake ice types having similar or slightly higher mean 19GHz brightness

Table 6.6 This table lists the mean airborne brightness temperatures for the vertically polarized 19GHz and 37GHz frequencies and the mean airborne estimated SWE values for all three different lake ice types and for the land class found in the regional tundra lake ice map

Free-Floating Lake Ice		Grounded Lake Ice		Unchanging Lake Ice		Land	
19GHz	37GHz	19GHz	37GHz	19GHz	37GHz	19GHz	37GHz
244	227	250	227	252	229	249	221
22mm		38mm		37mm		54mm	

temperatures to land. At first glance, the consistently lower 37GHz brightness temperatures over lakes were not easily explained when looking at the mean measured SWE for lakes versus land as shown in Table 5.3 in section 5.2. The mean measured SWE for lakes was 76mm, which was the second lowest SWE average next to the open polygonal tundra land cover with a mean of 69mm. The higher mean measured SWE over lakes does not explain the higher 37GHz brightness temperatures, in fact, these brightness temperatures should actually be lower than those measured over land. However, when the median measured SWE values for lakes versus open polygonal tundra were examined, the values of 54mm for lakes and 65mm for tundra better explained why the brightness temperatures over lakes were higher compared to land (more SWE on land was contributing to more volume scattering, leading to lower 37GHz brightness temperatures over land). The deeper snow along the lake edges, were skewing the mean measured SWE making it higher than it should have been and making the interpretation of the 37GHz brightness temperatures confusing. Using the median SWE values, the snow survey data indicates that lakes do capture less SWE compared to land matching the results noted by Sturm and Liston (2003), and Derksen et al., (2005).

6.4 Summary

The results discussed in this chapter provide the best possible evidence (without actually taking ice thickness measurements) that the lowest airborne SWE values are being recorded over lake features that most likely have liquid water below the ice. It appears that the 19GHz frequency was emanating from deep within the ice and was being influenced by the liquid water below the ice causing a substantial drop in brightness temperatures. These results are similar to Chang et al. (1997) who

modeled and observed a dramatic drop in the 19GHz frequency over lakes within the boreal forest compared to the adjacent land surfaces. Interestingly, the airborne SWE values estimated over the two other lake ice types were also quite a bit lower than the airborne SWE estimates estimated over the surrounding land. The reasons for these lower estimates were most likely due in part to presence of slightly less SWE on the lakes versus land, but could have also been caused by other unexplored factors such as the influence that snow drifts might have on microwave emission. None-the-less, all lakes were contributing to the passive microwave underestimation of SWE, with the greatest underestimation occurring over lakes with free-floating ice. This study was also the first known attempt at using the coarse resolution RADARSAT-1 ScanSAR Wide 2x2 block averaged CIS imagery for creating a regional lake ice map. A number of previous studies have shown the consistent backscatter characteristics in higher resolution SAR imagery for different lake ice types, and it became apparent that the backscatter response from the coarser resolution RADARSAT ScanSAR Wide imagery was still sensitive to different lake ice characteristics, however, the magnitude of this sensitivity was reduced.

Chapter 7
Conclusions, Limitations and Recommendations

7.1 Conclusions

The objective of this thesis was to identify and explore the dominant factors that influence microwave brightness temperatures in the tundra and thereby explain the consistent underestimation of satellite microwave SWE retrievals for this environment. Current satellite scale passive microwave underestimation of SWE in the tundra environment of the Hudson Bay Lowlands can likely be attributed to:

1) Extreme local scale snow depth and SWE variability in the exposed short/non vegetated open tundra environment.
2) The variable tundra snow cover has a significant proportion of its SWE mass balance spatially constrained to tall vegetated land cover features not accounted for by coarse resolution passive microwave spaceborne sensors.
3) The influence of tundra lakes that can lower the 19GHz brightness temperatures, especially those lakes with liquid water below the ice.

1. Extreme local scale snow variability on the open tundra plains

The first factor contributing to passive microwave underestimation of SWE on the tundra is related to the horizontal complexity of the tundra snowpack. Extremely variable snow depths and SWE can be found on local scales ranging from several tens of meters to sub-meter extent, with wind-scoured snow-free hummocks immediately next to substantial snow deposits found in polygonal tundra wedge depressions and depressed tundra ponds. This extremely variable micro-scale snow deposition provides a challenge for determining a mean SWE from ground measurements and for satellite-scale SWE estimation. This micro-scale variability is on such a fine scale that it cannot be measured by any current passive microwave remote sensors due to the coarse resolution of all available data. Current satellite SWE algorithms quantify how much microwave energy is scattered by the snowpack, and relate this quantification to how much SWE is on the ground. In theory, if a large percentage of the wind-swept open land cover within the tundra environment is virtually snow-free (as is the case for

this study site), microwave emission from these surfaces undergo minimal scattering, and existing SWE algorithms subsequently predict very low SWE levels.

2. Spatially constrained snow deposition in vegetated land covers

The second factor contributing to the passive microwave underestimation of SWE on the tundra is related to the re-distribution of blowing snow from the open tundra plains into vegetated land cover features such as forested creekbeds, lake edge willows, and isolated tundra tree-islands. The snow surveys showed that 2 to 3 times more snow was deposited in these vegetated features compared to the open tundra. The natural separation of snow into vegetated and non-vegetated land covers has profound implications because of the different study site proportions of each vegetated land cover type. The proportion of the tundra study site devoted to taller snow trapping vegetation is approximately 30 percent, and the remaining 70 percent is covered by short/non vegetated land covers. In theory, the short/non vegetated land cover contribute 70 percent of the microwave emission measured by current passive microwave satellite sensors, but this land cover contains only 50 percent of all SWE on the ground. The remaining 50 percent of SWE trapped in the taller vegetation is not fully accounted for, because it contributes to only 30 percent of the emission surface area measured by current passive microwave satellite sensors. Therefore, the spatially constrained snow distribution and its influence on microwave emission coupled with the influence of the extremely local scale snow variability of the open tundra plains discussed above, make it very difficulty to relate measured brightness temperatures with SWE in the tundra environment.

3. Influence of lakes on microwave emission

Previous studies have shown that longer wavelength passive microwave radiation can be influenced by water below free-floating lake ice, resulting in a drop in brightness temperatures over lakes compared to adjacent land (Hall et al., 1981). However, this influence has typically only been seen in microwave frequencies in and around the 5GHz range. This study supports the findings of Chang et al. (1997) that documented the probable influence of liquid water below solid free-floating lake ice on the 19GHz vertically polarized frequency causing a substantial drop in brightness temperatures. This response of the 19GHz frequency to lake features results in significantly different brightness temperatures between land versus lake surfaces. Lakes that are most likely frozen to bottom have a 19GHz brightness temperature more similar to the surrounding land, but still have lower airborne SWE estimates because the mean 37GHz airborne brightness temperature measured

over all lakes was higher than that measured over land. The 10K drop in 19GHz brightness temperatures over some lakes, coupled with a generally higher 37GHz brightness temperature leads to a very small brightness temperature difference. These very small 37GHz – 19GHz brightness temperature differences can lead to negative SWE estimates when using contemporary SWE algorithms. Negative SWE values estimated over small tundra lakes can contribute to an underestimation of SWE at the satellite scale because lake cover fraction can account for up to 40% of the land cover in a tundra environment.

However, due to the difference response in the 19GHz frequency mostly likely due to lakes frozen to bottom or not, it not only becomes necessary to take into account the influence of sub-grid scale tundra lake fraction on passive microwave SWE estimation, but it is also necessary to consider the seasonality of this influence because more lakes are likely to freeze to bottom as the winter season progresses. Therefore, from a passive microwave perspective the "true" lake fraction will actually depend on the proportion of lakes that have free-floating ice with liquid water below. Based on the results of the RADARSAT ScanSAR Wide analysis in this study, coarse resolution SAR imagery appears to be sensitive to changing lake ice properties. With further refinement this data source has the potential to create regularly updated "true" lake cover fraction maps for the tundra environment to help in the improvement of passive microwave remote sensing of SWE.

The results of this study highlight the difficulty in using coarse resolution passive microwave spaceborne sensors to estimate SWE in an environment with a high sub-grid lake cover fraction and a very heterogeneous snow distribution.

7.2 Study Limitations

There are a few caveats involved with this study, and these must be understood when reviewing the results of this research. The most notable limitations include:

1) Regions for which passive microwave SWE retrievals are considered 'accurate' typically produce estimates within +/-15mm of surface observations (Derksen et al., 2003). So there is an inherent level of uncertainty to be expected whenever passive microwave data are utilized to estimate SWE.
2) There are a number of limitations associated with using the coarse resolution synthetic aperture radar time series to define probable sub-snowpack lake ice properties in lieu of field observations. Firstly, the accepted practice of using a high resolution SAR time series to define lake properties was not followed. High resolution SAR imagery of remote locations involves pre-ordering. The influence of lakes on the 19GHz frequency was not anticipated during the planning stages of this research, and therefore no pre-ordering of SAR imagery was done. Secondly, the use of coarse resolution RADARSAT ScanSAR Wide imagery for a lake ice analysis has not been done before and therefore no references exist. Thus, with no field observations and no previous work to compare with, accuracy of the lake ice information cannot be assessed. The author realizes that the lake ice information produced in this study is purely speculative, and all interpretations of the airborne data associated with lake ice types are non-conclusive. Still, the retrieval of lake ice state information from ScanSAR wide imagery could represent an important contribution given the relative availability of these data.
3) There is an additional limitation associated with the tundra lake ice map produced from the supervised classification of the principal component analysis outputs of the SAR time series. Only a single iteration of identifying training sites, running the supervised classification algorithms, and assessing the accuracy of the classified image was conducted because of time constraints. Improved accuracies would likely have been attained if training sites had been re-assessed and the classification was run multiple times. However, the true accuracy of the classified lake ice map could never be assessed because no field observations were recorded.

7.3 Recommendations for future research and SWE algorithm development

Recommendation #1

SWE retrieval algorithms applied to the boreal forest / tundra transition zone of the southern tundra environment should account for the percentage of land cover devoted to taller snow-trapping vegetated features, which could potentially be provided by current land cover classifications, and appropriate correction coefficients should be applied accordingly. In addition, future tundra specific SWE algorithms should also account for the extremely variable SWE of the open tundra plains. The nature of the satellite measurements means that only a single SWE value is retrieved per grid cell. Means of attaching upper and lower bounds to these estimates should be explored.

Recommendation #2

Future passive microwave research in the tundra environment should focus on detailed studies of documenting microwave emission from differing lake ice properties including: lakes frozen to bed and with free-floating ice, lake ice with variable bubble concentrations, and lakes with white ice (snow ice). This research would allow for a better assessment of the influence that lakes have on passive microwave brightness temperatures and current underestimation of SWE in the tundra, and if necessary this knowledge would assist in the development of a specific tundra lake SWE algorithm.

Recommendation #3

A more focused approach to future passive microwave SWE retrieval research should be taken. Instead of collecting airborne brightness temperatures over large areas such as a 25km x 25km flight grid, or along lengthy transects several 100kms long, efforts should be made to measure brightness temperatures at local scales where ground personnel would be able to collect detailed snow cover and lake ice information needed to more accurately interpret the brightness temperatures. Future studies should begin to focus more on the use of ground radiometer units, and smaller scale flight grids that focus on more homogeneous land covers so that unmixed radiometric signatures can be developed for specific snow and lake ice properties in the tundra which could then be used to interpret the satellite scale brightness temperatures.

Recommendation #4

Future tundra passive microwave SWE retrieval research should include a temporal component. All previous work has focused on a single time period during the winter season typically during late winter at the time of maximum SWE levels. However, deposition of snow and the growth of lake ice are both dynamic processes, and to fully understand how these processes change over the course of the winter they must be monitored throughout the winter season. Therefore, a study should be done that involves revisiting the same site during the initial onset, early, mid and late winter to conduct snow surveys, lake ice surveys and to measure passive microwave brightness temperatures at each of these times.

Recommendation #5

Efforts should be made to further explore the use of SAR winter time series for extraction of lake ice information useful for the interpretation of passive microwave emission from tundra lakes. There is great potential in using RADARSAT ScanSAR Wide images for the purpose of mapping regional lake ice conditions with its daily repeat coverage of the arctic tundra environment. This study was the first known attempt at using the coarse resolution RADARSAT-1 ScanSAR Wide 2x2 block averaged imagery for a tundra lake ice analysis. It was apparent that the coarse resolution SAR imagery was sensitive to different lake ice characteristics, however, the magnitude of this sensitivity was reduced compared to previous studies using higher resolution imagery. To truly assess the usefulness of this proposed method of lake ice mapping, field observations are needed that coincide with the dates of all images used in the time series and this type of lake ice research should be a high priority for future SAR ice studies.

Bibliography

Armstrong, R., and M. Brodzik. 1995: An earth-gridded SSM/I data set for cryospheric studies and global change monitoring. *Advanced Space Research*. **16** (10): pp. 10155-10163.

Bertoia, C. and B. Ramsay. 1998. Sea ice analysis and products: cooperative work at the US and Canadian national ice centers. *Geoscience and Remote Sensing Symposium, 1998.* IGARSS '98, Seattle, Washington. **4**: pp. 1944-1947.

Brook, Ryan. K. 2001. *Structure and dynamics of the vegetation in Wapusk National Park and the Cape Churchill wildlife management area of Manitoba: community and landscape scales*, Masters Thesis. University of Manitoba, Winnipeg.

Brown, R., A. Walker and B. Goodison, 2000. Seasonal snow cover monitoring in Canada - an assessment of Canadian contributions for global climate monitoring. *Proceedings, 57th Eastern Snow Conference*, Syracuse, New York, pp 131-141.

Bruland, O., K. Sand, and A. Killingtveit. 2001. Snow distribution at a high arctic site at Svalbard. *Nordic Hydrology*. **32:** pp 1-12.

Boudreau LD, Rouse WR. 1994. Algorithm testing of passive microwave monitoring of snow water equivalent in a tundra environment. Report Contract Number KM040-2-9008, Atmospheric Environment Service, Environment Canada, 70 pp.

Byrne, G.F., P.F. Crapper, and K.K. Mayo. 1980. Monitoring land cover change by principal components analysis of multitemporal Landsat data. *Remote Sensing of Environment*, **10:** pp 175-184.

Cameron, M.A., R.W. Gorman, M.J. Manore, A.E. Owens, G.M. Shirtliffe, and R.O. Ramsier. 1984. Passive Microwave Observations of St. Lawrence Seaway Ice and Snow. *9th Canadian Symposium on Remote Sensing*. St. John, Nfld. pp 121-129.

Canadian Digital Elevation Data – CDED 1:250,000 [Raster Digital Data]. 2003. Sherbrooke, Quebec, Natural Resources Canada, Centre for Topographic Information. Available at: http://www.geobase.ca/geobase/en/data/cded/index.html [Accessed March 5th 2007].

Chang, A.T.C., P. Gloersen, T. Schmugge, T.T. Wilheit, and H.J. Zwally. 1976. Microwave emission from snow and glacier ice. *Journal of Glaciology*. **16** (74): pp 23-39.

Chang, A.T.C., J. L. Foster, and D.K. Hall. 1987. NIMBUS-7 SMMR derived snow cover parameters. *Annals of Glaciology*. **9**: pp 39-44.

Chang, A.T.C., J.L. Foster, D.K. Hall, B.E. Goodison, A.E. Walker, J.R. Metcalfe, and A. Harby. 1997: Snow parameters derived from microwave measurements during the BOREAS winter field campaign. *Journal of Geophysical Research*. **102** (D24): pp 29,633-29,671.

Colbeck, S. C. 1991. The layered character of snow covers. *Reviews of Geophysics.* **29** (1): pp 81-96.

Derksen, C., A. Walker, and B. Goodison. 2003. A comparison of 18 winter seasons of in situ and passive microwave derived snow water equivalent estimates in Western Canada. *Remote Sensing of Environment*. **88** (3): pp 271-282.

Derksen, C., A. Walker, and B. Goodison. 2005. Evaluation of passive microwave snow water equivalent retrievals across the boreal forest / tundra transition of western Canada. *Remote Sensing of Environment*. **96** (3-4): pp 315-327.

De Sève, D., M. Bernier, J-P. Fortin, and A. Walker. 1997. Preliminary analysis of snow microwave radiometry using the SSM/I passive microwave data: the case of La Grande River watershed (Quebec). *Annals of Glaciology*. **25**: pp 353-261.

Duguay, C., J. Green, C. Derksen, M. English, A. Rees, M. Sturm, and A. Walker. 2005. Preliminary assessment of the impact of lakes on passive microwave snow retrieval algorithms in the Arctic. *Proceedings of the 62nd Annual Eastern Snow Conference*. Waterloo, ON, June. pp 223-228.

Duguay, C.R. and P.M. Lafleur. 2003. Determining depth and ice thickness of shallow sub-Arctic lakes using space-borne optical and SAR data. *International Journal of Remote Sensing*. **24** (3): pp 474-489.

Duguay, C. R., T.J. Pultz, P.M. Lafleur, D. Drai. 2002. RADARSAT backscatter characteristics of ice growing on shallow sub-Arctic lakes, Churchill, Manitoba, Canada. *Hydrological Processes*. **16**: pp 1631-1644.

Durand, M., and S. Margulis. 2006. Feasibility Test of Multifrequency Radiometric Data Assimilation to Estimate Snow Water Equivalent. *Journal of Hydrometeorology.* **7**: pp 443-457.

Essery, R., L. Li, and J. Pomery. 1999. A distributed model of blowing snow over complex terrain. *Hydrological Processes*. **13**: pp 2423-2438.

Frei, A., J.A. Miller and D.A. Robinson. 2003. Improved simulations of snow extent in the second phase of the Atmospheric Model Intercomparison Project (AMIP-2). *Journal of Geophysical Research.* **108** (D12): pp 10-1 to 10-17.

French, N., S. Savage, R. Shuchman, R. Edson, J. Payne and E. Josberger. 2004. Remote sensing of frozen lakes on the North Slope of Alaska. *Geoscience and Remote Sensing Symposium, 2004.* IGARSS '04, Anchorage, Alaska. **5**: pp 3008-3011.

Kloiber, S. M., P. L. Brezonik and M. E. Bauer. 2002. Application of Landsat imagery to regional-scale assessments of lake clarity. *Water Research*. **30**: pp 4330-4340.

GeoCover™ - Orthorectified Landsat Enhanced Thematic (ETM+) Compressed Mosaics [Raster Digital Data] 2000. Earth Satellite Corporation. Available at: https://zulu.ssc.nasa.gov/mrsid/mrsid.pl [Accessed May 11th 2005].

Goodison, B.E. 1989. Determination of areal snow water equivalent on the Canadian prairies using passive microwave satellite data. *12th Canadian Symposium on Remote Sensing*. Vancouver, BC, July 10-14, **13**: pp 1243-1246.

Goita, K., A. Walker and B. Goodison. 2003. Algorithm development for the estimation of snow water equivalent in the boreal forest using passive microwave data. *International Journal of Remote Sensing*. **24** (5): pp. 1097-1102.

Gray, D. M. and D. H. Male, ed. 1981. Handbook of Snow, Principles, processes, management & use, Toronto, Canada: Pergamon Press.

Hall, D.K., M. Sturm, C.S. Benson, A.T.C. Chang, J.L. Foster, H. Garbeil and E. Chacho. 1991. Passive microwave remote and in situ measurements of artic and subarctic snow covers in Alaska. *Remote Sensing of Environment*. **38**: pp 161-172.

Hall, D.K. 1987. Influence of depth hoar on microwave emission from snow in northern Alaska. *Cold Regions Science and Technology*. **13**: pp 225-231.

Hall, D.K., J.L. Foster and A.T.C. Chang. 1981. Freshwater ice thickness observations using passive microwave sensors. *IEEE Transactions on Geoscience and Remote Sensing.* **GE-19** (4): pp 189-193.

Hall, D.K., J.L. Foster, A. Rango and A.T.C. Chang. 1978. Passive microwave studies of frozen lakes. *Proceedings of the American Society of Photogrammetry: Fall Technical Meeting.* pp 195-207.

Hallikainen, M. 1992. Review of the Microwave Dielectric and Extinction Properties of Sea Ice and Snow. *Proc. IEEE Transactions on Geoscience and Remote Sensing Symposium (IGARSS) (Houston, Texas: May 26-29)* pp 961 - 965.

Hallikainen, M, T., V.S. Jaaskelainen, J. Pulliainen and J. Koskinen. 2000. Transmissivity of boreal forest canopies for microwave radiometry of snow. *Proc. IEEE Transactions on Geoscience and Remote Sensing Symposium*. *(IGARSS), (Honolulu, Hawaii: July 2000)* pp 1564–1566.

Hirashima, H., O. Tetsuo., Y. Kudama., H. Yabuki., N. Sato., and A. Georgiadi. 2004. Nonuniform distribution of tundra snow cover in eastern Siberia. *Journal of Hydrometeorology*. **5**: pp 373-389.

Hollinger, J.P., J.L. Peirce, and G.A. Poe, 1990. SSM/I instrument evaluation, *IEEE Transactions on Geoscience and Remote Sensing*, ***28 (5)***: pp 781-790.

Jensen, J.R. 2005. *Introductory Digital Image Processing: A Remote Sensing Perspective*. 3rd Ed. Prentice Hall series in geographic information science.

Jeffries, M.O., K. Morris, and W.F. Weeks. 1994. Structural and stratigraphic features and ERS 1 synthetic aperture radar backscatter characteristics of ice growing on shallow lakes in NW Alaska, winter 1991-1992. *Journal of Geophysical Research.* **99** (C11): pp 22,459-22,471.

Kawanishi, T., T, Sezai., Y, Ito., K, Imaoka., T, Takeshima., Y. Ishido., A, Shibata., M, Miura., H, Inahata and R.W., Spencer. 2003. The advanced microwave scanning radiometer for the earth observing system (AMSR-E), NASDA's contribution to the EOS for the global energy and water cycle studies. *IEEE Transactions on Geoscience and Remote Sensing* **41** (2): pp 184-194.

Kidd, C. 2006. Radio frequency interference at passive microwave earth observation frequencies. *International Journal of Remote Sensing.* **27** (18): pp 3853-3865.

Kite, G.W. 1995. Scaling of input data for macroscale hydrological modeling. *Water Resource Research*. **31** (11): pp 2769-2781.

Kloiber, S. M., P. L. Brezonik and M. E. Bauer. 2002. Application of Landsat imagery to regional-scale assessments of lake clarity. *Water Research*. **30**: pp 4330-4340

Koenig, Lora S. and R.R. Forster. 2004. Evaluation of passive microwave snow water equivalent algorithms in the depth hoar-dominated snowpack of the Kuparuk River Watershed, Alaska, USA *Remote Sensing of Environment* **93**: pp 511-527.

Kozlenko, N. and M. O. Jefferies. 2000. Bathymetric mapping of shallow water in thaw lakes on the north slope of Alaska with spaceborne imaging radar. *Arctic*. **53** (3): pp 306-316.

Kurvonen, L., and M. Hallikainen. 1997. Influence of land cover category on brightness temperature of snow. *IEEE Transactions on Geoscience and Remote Sensing*. **35** (2): pp 367–77.

Lillesand, Thomas M, Ralph, W. Kiefer. 2000. Remote sensing and image interpretation, 4th ed. New York, United States. John Wiley & Sons, Inc.

Liston, G.E., and M. Sturm. 1998. A snow-transport model for complex terrain. *Journal of Glaciology*. **44**: pp 498-516.

Markus, T., D. Powell, and J. Wang. 2006. Sensitivity of passive microwave snow depth retrievals to weather effects and snow evolution. *IEEE Transactions on Geoscience and Remote Sensing.* **44** (1): pp 68-77.

Mätzler, C., E. Schanda, and W. Good. 1982. Towards the definition of optimum sensor specifications for microwave remote sensing of snow. *IEEE Transactions on Geoscience and Remote Sensing*. **GE-20** (1): pp 57-66.

Morris, K., M.O. Jeffries, and W.F. Weeks. 1995. Ice processes and growth history on Arctic and sub-Arctic lakes using ERS-1 SAR data. *Polar Record.* **31** (177): pp 115-128.

National Climate Data. 2007. Environment Canada, Available at: http://www.climate.weatheroffice.ec.gc.ca/climateData/canada_e.html [Accessed on June 12th 2007] .

National Scale Frameworks Hydrology - Drainage Network, Hudson Bay [Vector Digital Data]. 2003. Ottawa, Ontario, The Atlas of Canada. Available at: http://geogratis.cgdi.gc.ca/geogratis/en/collection/search.do [Accessed June 5th 2007].

Parks Canada. 1977. *Natural Theme Analysis of Natural Region 27 – The Hudson-James Bay Lowlands.* Government of Canada, Ottawa, Canada.

Parra, G.A., M. Moucho and C. Roux. 1996. A multitemporal land cover change analysis tool using change vector and principal components analysis. *Geoscience and Remote Sensing Symposium, 1996*. IGARSS '96, Lincoln, NE. **3**: pp 1753-1755.

Pomeroy, J. W., P. Marsh and D. M. Gray. 1997. Application of a distributed blowing snow model to the arctic. *Hydrological Processes*. **11**: pp 1451-1464.

RADARSAT International. 1999. *RADARSAT Illuminated, Your Guide to Products and Services*. RADARSAT International, Communications Department, BC, Canada, Available at: http://gs.mdacorporation.com/products/sensor/radarsat/rsiug98_499.pdf, [Accessed on March 2nd, 2007].

RADARSAT International. 2000. *D4-RADARSAT Data Product Specifications*. Document no. RSI-GS-026. Version 3, May 8th 2000.

Rees, A., M. English, C. Derksen and A. Walker. 2005. Assessing snowpack water equivalent distribution in an open tundra environment using various scales of passive microwave data. *62nd Eastern Snow Conference Proceedings, Waterloo, Ontario, Canada*. pp 229-233.

Rees, A., C. Derksen, M. English, A. Walker, C. Duguay. 2006. Uncertainty in snow mass retrievals from satellite passive microwave data in lake-rich high-latitude environments. *Hydrological Processes* **20** (4): pp 1019-1022.

Schmugge, T., T.T. Wilheit, P. Gloersen, M.F. Meier, D. Frank and I. Dirnhirn. 1974. Microwave signatures of snow and fresh water ice. *Advanced Concepts and Techniques in the Study of Snow and Ice Resources.* National Academy of Sciences, Washington D.C. pp 551-562.

Sellman, P.V., J. Brown., R.I. Lewellen., H. Mckim., and C. Merry. 1975. The classification and geomorphic implications of thaw lakes on the arctic coastal plain, Alaska. *U.S. Army Cold Regions Research & Engineering Laboratory, Research Report 344*. Hanover, New Hampshire. pp 21.

Sturm, M. and G. E. Liston. 2003. The snow cover on lakes of the Arctic Coastal Plain of Alaska. J. of Glaciology, **49** (166): pp 370-380.

Sturm, M., J.P. McFadden, G.E. Liston, F. S. Chapin III, C.H. Racine, and J. Holmgren. 2000. Snow-shrub interactions in arctic tundra: a hypothesis with climatic implications. *Journal of Climate*. **14**: pp 336-344.

Sturm, M. and C.S. Benson. 1997. Vapor transport, grain growth and depth hoar development in the subarctic snow. *Journal of Glaciology*. **43**: pp 42-59.

Sturm, M., J. Holmgren, and G. Liston. 1995. A seasonal snow cover classification system for local to global applications. *Journal of Climate* **8** (5): pp 1261-1283.

Sturm, M., T.C. Grenfell and D.K. Perovich. 1993. Passive microwave measurements of tundra and taiga snow covers in Alaska, U.S.A. *Annals of Glaciology*. **17:** pp 125-130.

Swift, C.T., W.L. Jones, Jr., R.F. Harrington. 1980. Microwave radar and radiometric remote sensing measurements of lake ice. *Geophysical Research Letters*. **7**: pp 243-246.

Tait, A.B. 1998. Estimation of snow water equivalent using passive microwave radiation data. *Remote Sensing of Environment.* **64:** pp 286-291.

Tedesco, M., and J. Wang. 2006. Atmospheric correction of AMSR-E brightness temperatures for dry snow cover mapping. *IEEE Geoscience and Remote Sensing Letters*. **3** (3): pp 320-324.

The State of Canada's Ecosystems in Maps – EcoAtlas [Vector Digital Data]. 2002. Ottawa, Ontario, The Government of Canada. Available at: http://geogratis.cgdi.gc.ca/geogratis/en/collection/search.do [Accessed June 5th 2007].

Ulaby, F.T. R.K. Moore and A.K. Fung. 1981. *Microwave Remote Sensing, Active and Passive, Vol I: Microwave Remote Sensing Fundamentals and Radiometry,* Addison-Wesley Publishing Co, Advanced Book Program, Reading, Massachusetts.

Ulaby, F.T., R.K. Moore and A.K. Fung. 1982. *Microwave Remote Sensing, Active and Passive, Vol II: Radar Remote Sensing and Surface Scattering and Emission Theory*, Addison-Wesley Publishing Co, Advanced Book Program, Reading, Massachusetts.

Ulaby, F.T., R.K. Moore and A.K. Fung. 1986. *Microwave Remote Sensing, Active and Passive, Vol III: From Theory to Applications*, Addison-Wesley Publishing Co, Advanced Book Program, Reading, Massachusetts.

Walker, A.E., J.W. Strapp, and I. Macpherson. 2002: A Canadian Twin Otter microwave radiometer installation for airborne remote sensing of snow, ice and soil moisture. *CD-ROM Proceedings, International Geoscience and Remote Sensing Symposium*, Toronto, June, 2002.

Wilson, G. S. 1996, July, 15. In *NASA/Marshall Space Sciences Electromagnetic Spectrum Diagram*. Available at: http://science.nasa.gov/newhome/help/glossfig1.htm [Accessed September 19th 2006].

Woo, M. 1998. Arctic snow cover information for hydrological investigations at various scales. *Nordic Hydrology*. **29:** pp 245-266.

Woodhouse, I. H., 2006. Introduction to microwave remote sensing. Boca Raton, Florida, United States: CRC Press Taylor & Francis Group.